The Characterisation and Manipulation of Novel Topological Phases of Matter

James de Lisle

Department of Physics and Astronomy

University of Leeds

A thesis submitted for the degree of

Doctor of Philosophy

 I confirm that the work submitted in this thesis is my own, except where work which has formed part of jointly authored publications has been included. The contribution of myself and the other authors to this work has been explicitly indicated below. I confirm that appropriate credit has been given within the thesis where reference has been made to the work of others.

Publications:

de Lisle, J., De, S., Alba, E., Bullivant, A., Garcia-Ripoll, J.J., Lahtinen, V. and Pachos, J.K. (2014). *Detection of Chern numbers and entanglement in topological two-species systems through subsystem winding numbers.* New Journal of Physics, **16**, 083022.

Chapter 2 is based on the work presented in this paper. I personally derived the proof of the decomposition of the Chern number in the case of superconductors and insulators. The numerical case studies were performed by collaborators.

Finch, P., de Lisle, J., Palumbo, G., Pachos, J. K. (2015) *Induced Topological Phases at the Boundary of 3D Topological Superconductors.* Phys. Rev. Lett. **114**, 016801.

Chapter 3 is based on this paper. Numerical work was performed by Peter Finch, the field theory in the penultimate section was performed by Giandomenico

Palumbo and Jiannis Pachos. I was responsible for constructing the general model and direction and analysis of the numerical results.

For Mr Bull

Acknowledgements

Primarily I would like to thank my supervisor Jiannis Pachos, without whom I would not be where I am today. His belief and patience over the last five years has been a source of motivation and inspiration.

I would also like to thank my fellow PhD students with whom I have struggled with and discussed the various topics and concepts that went into this work.

Finally I would like to thank my family and friends who have given me the love and support needed to pursue my love of physics. Without them I am nothing.

Abstract

This thesis contains work in three areas. The works are presented chronologically starting with my work on the decomposition and measurement of Chern numbers in four component topological insulators and superconductors. This is followed by the work done in the discovery and analysis of four new models of topological superconductivity in three spatial dimensions. Lastly, I present the work done on dimensional reduction through localisation of Majorana modes at the boundary of topological superconductors in three spatial dimensions. Each work is presented in a separate chapter.

Contents

List of Figures

Chapter 1

Introduction

1.1 Introduction

For many years changes in phases of matter were thought to be completely described by Landau's theory of spontaneous symmetry breaking (SSB) [1]. By characterising phases of matter by the symmetries that they break, while defining a local order parameter that contains the information about how the matter in the system is ordered, a wide variety of different physical systems can be accurately described [2, 3]. It was thought that, given that it could describe such a wide range of apparently unrelated physical phenomena, SSB might be able to describe every kind of phase change in physics. This illusion was shattered with the discovery of the integer quantum Hall effect [4]. The observed quantisation in the Hall conductance defied explanation by SSB and required a new approach. It was found that the observed effect was a result of the underlying topology of the Hilbert space in which the ground state resides [5]. The notion of *topological order* was born.

The set of systems that present topological order (TO) is currently quite a broad church. Further to this, the set of indicators that point the presence of

TO is just as varied. A few examples of such indicators include the entanglement entropy [6, 7, 8]; a degeneracy in the ground state that is linked to the topology of the underlying manifold and by implication the ability to support non-Abelian anyonic quasi-particles [9, 10]; the presence of gapless edge modes [11, 12]. As one might guess from these examples the term 'topological order' has a somewhat contested definition. It has been used to refer to fractional quantum Hall states [13, 14], which emerge from systems with strong electron-electron interactions. It can also refer to systems of free fermions which exhibit topologically non-trivial quasi-particles, such as Majorana fermions trapped at the center of vortex excitations in the Kitaev honeycomb lattice model [10].

For the purposes of this thesis it is sufficient to restrict ourselves mostly to the discussion of *topological phases*. By this we refer to a given system supporting a non-trivial topological index [15, 16, 5, 17, 18, 19]. As shall be discussed in greater detail in subsequent chapters, these indices are indicators of the topology of the fiber bundle in which the ground state of a system lives [19]. Such quantities are often defined in terms of projectors onto the bulk ground state wave functions. These indices are also known as *invariants* due to their behavior under adiabatic deformation of the system. Consider an invariant $\nu(\boldsymbol{\lambda}) : \mathcal{M} \to \mathbb{Z}$, where $\boldsymbol{\lambda} = \left(\lambda_1, \quad \ldots, \quad \lambda_{N+M}\right) \in \mathcal{M} \subset \mathbb{R}^N \times \mathbb{C}^M$ is a set of coefficients that parametrise the Hamiltonian of a system. If the system undergoes an adiabatic evolution of the form $\boldsymbol{\lambda}(t_0) \to \boldsymbol{\lambda}(t)$, we have $\nu(\boldsymbol{\lambda}(t_0)) = \nu(\boldsymbol{\lambda}(t))$ as long as certain spectral conditions are met. For bulk topological invariants to be well defined, the bulk ground state wave functions from which they are derived must be energetically gapped from the excited modes. As long as the system remains spectrally gapped the topological invariant remains constant. In some circumstances the existence of a non-trivial topological index is reflected in some other physical characteristic

which can be regarded as TO, such as the examples given above. More often than not this primary indicator of a systems topological phase is not directly accessible. This is one of the issues that we address in this work.

The set of discrete symmetries that a Hamiltonian obeys determines which particular index is used. There exists whole schemes for the classification of Hamiltonians based purely on what symmetries they adhere to. For non-interacting fermionic systems the celebrated 10-fold way [17, 19, 20] details ten distinct symmetry classes delineated by three non-spatial symmetries, time-reversal, particle-hole, and sublattice. This scheme was then extended to include spatial symmetries [21, 22, 23]. Kitaev introduced a means of classifying topological superconductors via the types of statistics their quasi-particle excitations obey [10], sometimes called the 16-fold way. A more recent development has been the realisation that in the presence of interactions the 10-fold way classification scheme gives way to a different landscape of classes. Counter examples [24] show the adiabatic connection of two distinct classes previously thought to be separate. This was followed by a more rigorous formulation of the phenomenon [25, 26, 27].

We now present a short summary of the essential elements of the 10-fold way classification scheme for non-interacting fermionic Hamiltonians, summarising the excellent work by Chiu *et al.* [19].

1.2 Symmetry protected topological order: the 10-fold way

1.2.1 Time-reversal symmetry

Given some state $\Psi(\boldsymbol{r},t) = \Psi_n(\boldsymbol{r})e^{-\frac{i}{\hbar}E_n t}$ that satisfies the Schrödinger equation,

$$i\hbar\frac{\partial}{\partial t}\Psi(\boldsymbol{r},t) = \left(-\frac{\hbar^2}{2m}\nabla^2 + V\right)\Psi(\boldsymbol{r},t) = H\Psi(\boldsymbol{r},t), \tag{1.1}$$

one can ask whether the state $\Psi(\boldsymbol{r},-t)$ is also a solution. Explicit evaluation of (1.1) finds that this is not the case. However the complex conjugate of $\Psi(\boldsymbol{r},-t)$, $\Psi^*(\boldsymbol{r},-t) = \Psi_n^*(\boldsymbol{r})e^{-\frac{i}{\hbar}E_n t}$ is a solution, where the wave function $\Psi_n^*(\boldsymbol{r}) = \langle \boldsymbol{r}|\Psi\rangle^* = \langle\Psi|\boldsymbol{r}\rangle$.

The time-reversal (TR) operator $\hat{\Theta}$ maps a state onto its time reversed partner, $|\Psi\rangle \to \Theta|\Psi\rangle$. Consider the Taylor expanded, time evolved state

$$|\Psi(t_0 = 0 : t = \delta t)\rangle = \left(1 - \frac{i}{\hbar}H\delta t\right)|\Psi\rangle\,. \tag{1.2}$$

where δt is small. If the evolution of the system is TR symmetric then we have

$$\hat{\Theta}\left(1 - \frac{i}{\hbar}H(-\delta t)\right)|\Psi\rangle = \left(1 - \frac{i}{\hbar}H\delta t\right)\hat{\Theta}|\Psi\rangle\,. \tag{1.3}$$

In order for (1.3) to hold we require that $\hat{\Theta}iH|\Psi\rangle = -iH\hat{\Theta}|\Psi\rangle$. This equality implies that $\hat{\Theta}$ is an antiunitary operator which takes the general form

$$\hat{\Theta} = U\mathcal{K} \tag{1.4}$$

where in general $U \in U(n)$. $\mathcal{K}$ is the complex conjugation operator which acts on states in the following way

$$\mathcal{K}c|\psi\rangle = c^*\mathcal{K}|\psi\rangle \tag{1.5}$$

and by implication has the properties $\mathcal{K} = \mathcal{K}^{-1}$ and $\mathcal{K}^2 = 1$. By virtue of its antiunitarity the TR operator preserves only the absolute value of the inner product

$$\left|\langle\hat{\Theta}\psi|\hat{\Theta}\phi\rangle\right| = |\langle\psi|\phi\rangle^*|\,, \tag{1.6}$$

i.e. it is antilinear.

Phase ambiguity

If one acts the TR operator twice, any system should remain the same up to a $U(1)$ phase

$$\hat{\Theta}^2 = \alpha, \quad |\alpha| = 1. \tag{1.7}$$

Using the explicit form of $\hat{\Theta}$ we have

$$U\mathcal{K}U\mathcal{K} = UU^*\mathcal{K}^2 = UU^* = \alpha. \tag{1.8}$$

Following on we have $U^* = \alpha U^\dagger = \alpha \left(U^T\right)^*$ from which we can derive

$$\begin{aligned} U^*\left(U^*\right)^\dagger U^* &= \alpha \left(U^T\right)^* \left(U^*\right)^\dagger U^* \\ U^* &= \alpha \left(U^T\right)^* U^T U^* \\ U^* &= \alpha^2 U^*. \end{aligned} \tag{1.9}$$

This implies $\alpha = \pm 1$. In the case of spinless systems the unitary operator $U \in U(1)$, i.e. $\hat{\Theta} = e^{i\theta}\mathcal{K}$, and $\hat{\Theta}^2 = 1$. For spinful systems U is more complex and can lead to situations where $\hat{\Theta}^2 = -1$.

The TR operator acts on the angular momentum operator as $\hat{\Theta}\hat{\boldsymbol{J}}\hat{\Theta}^{-1} = -\hat{\boldsymbol{J}}$. For spin-$\frac{1}{2}$ particles we also require that the spin angular momentum operator $\hat{\boldsymbol{S}}$ transforms as $\hat{\Theta}\hat{\boldsymbol{S}}\hat{\Theta}^{-1} = -\hat{\boldsymbol{S}}$. The spin angular momentum operator is given by

$$\hat{\boldsymbol{S}} = \frac{\hbar}{2}\boldsymbol{\sigma}, \quad \sigma^x = \begin{pmatrix} 0 & 1 \\ 1 & 0 \end{pmatrix}, \quad \sigma^y = \begin{pmatrix} 0 & -i \\ i & 0 \end{pmatrix}, \quad \sigma^z = \begin{pmatrix} 1 & 0 \\ 0 & -1 \end{pmatrix}. \tag{1.10}$$

Given this form we can construct a set of equations that characterise Θ in the case of spin

$$\begin{aligned}
\hat{\Theta}\sigma^x\hat{\Theta}^{-1} &= U\mathcal{K}\sigma^x\mathcal{K}U^{-1} = U\sigma^xU^{-1} = -\sigma^x, \\
\hat{\Theta}\sigma^y\hat{\Theta}^{-1} &= U\mathcal{K}\sigma^y\mathcal{K}U^{-1} = -U\sigma^yU^{-1} = -\sigma^y, \\
\hat{\Theta}\sigma^z\hat{\Theta}^{-1} &= U\mathcal{K}\sigma^z\mathcal{K}U^{-1} = U\sigma^zU^{-1} = -\sigma^z.
\end{aligned} \tag{1.11}$$

Equations (1.11) imply that U needs to commute with σ^y and anticommute with σ^x and σ^z. By inspection we have

$$\hat{\Theta} = i\sigma^y\mathcal{K}. \tag{1.12}$$

We note that $i\sigma^y\mathcal{K}i\sigma^y\mathcal{K} = -1$. If the system has N spin-$\frac{1}{2}$ particles the TR operator takes the form

$$\begin{aligned}
\hat{\Theta} &= i\sigma_1^y i\sigma_2^y ... i\sigma_N^y\mathcal{K} \\
&= \exp\left[i\frac{\pi}{2}\left(\sigma_1^y + \sigma_2^y + ... + \sigma_N^y\right)\right]\mathcal{K} \\
&= \exp\left(i\pi\frac{S_y}{\hbar}\right)\mathcal{K}
\end{aligned} \tag{1.13}$$

where S_y is the y-component of the total spin operator $\hat{\boldsymbol{S}} = \hbar\left(\boldsymbol{\sigma}_1 + \boldsymbol{\sigma}_2 + ... + \boldsymbol{\sigma}_N\right)$. As such

$$\hat{\Theta}^2 = \begin{cases} 1 & N \text{ is even} \\ -1 & N \text{ is odd} \end{cases} \tag{1.14}$$

Kramers degeneracy

Consider a system where the TR operator commutes with the Hamiltonian, i.e. $[H, \hat{\Theta}] = 0$. The action of the TR operator on the time-independent Schrödinger equation is given by

$$\hat{\Theta}\hat{H}\left|\psi_n\right\rangle = \hat{H}\hat{\Theta}\left|\psi_n\right\rangle = E_n\hat{\Theta}\left|\psi_n\right\rangle. \tag{1.15}$$

where $|\psi_n\rangle$ and E_n are the eigenvectors and eigenvalues of $\hat{H}$. If we assume that $|\psi_n\rangle$ and $\hat{\Theta}|\psi_n\rangle$ are the same eigenstate then we must have $\hat{\Theta}|\psi_n\rangle = e^{i\theta}|\psi_n\rangle$. If we act the TR operator onto the state a second time we find

$$\begin{aligned}\hat{\Theta}^2|\psi_n\rangle &= \hat{\Theta}e^{i\theta}|\psi_n\rangle \\ &= e^{-i\theta}\hat{\Theta}|\psi_n\rangle \\ &= e^{-i\theta}e^{i\theta}|\psi_n\rangle \\ &= |\psi_n\rangle\,. \end{aligned} \tag{1.16}$$

If $\Theta^2 = -1$ then (1.16) does not hold. This implies that $\hat{\Theta}|\psi_n\rangle$ is a state *distinct* from $|\psi_n\rangle$. By (1.15) the two states are degenerate. This is known as a Kramers degeneracy. In spin-$\frac{1}{2}$ systems with an odd number of spins of fermionic systems in general with an odd number of fermions, such degenerate pairs always appear.

Free fermion systems

The concept of TR symmetry can be applied to free fermion tight-binding Hamiltonians. Consider a system defined on a lattice which supports a set of second quantised fermionic operators

$$\left\{\hat{a}_I, \hat{a}_I^\dagger\right\}_{I=1,\ldots,N}, \tag{1.17}$$

where I is some generalised index which can include labels such as position and spin. These operators act on a fermionic Fock space and obey the canonical fermionic anticommutation relations

$$\left\{\hat{a}_I, \hat{a}_J^\dagger\right\} = \delta_{IJ} \tag{1.18}$$

Assuming it is not superconducting, the system is described by the Hamiltonian

$$\hat{\mathcal{H}} = \hat{a}_I^\dagger H_I^J \hat{a}_J = \boldsymbol{\psi}^\dagger H \boldsymbol{\psi}, \tag{1.19}$$

where in general $H_I^J \in \mathbb{C}$, and Einstein summation convention has been used. H is the sometimes known as the first quantised, single particle, or *kernel* Hamiltonian. TR symmetry is defined in terms of the action of a second quantised antiunitary operator $\hat{\mathscr{T}}$ on the fermionic creation and annihilation operators

$$\hat{a}_I \to \hat{a}'_I : \hat{\mathscr{T}} \hat{a}_I \hat{\mathscr{T}}^{-1} = (U_T)_I^J \, \hat{a}_J, \qquad \hat{\mathscr{T}} i \hat{\mathscr{T}}^{-1} = -i, \tag{1.20}$$

where $(U_T)_I^J \in \mathbb{C}$. The system is said to be invariant under this transformation if two conditions are met. The canonical anticommutation relations must be preserved

$$\hat{\mathscr{T}} \left\{ \hat{a}_I, \hat{a}_J^\dagger \right\} \hat{\mathscr{T}}^{-1} = \left\{ \hat{a}_I, \hat{a}_J^\dagger \right\}, \tag{1.21}$$

implying that $(U_T)_I^J$ is a unitary matrix. Additionally, the second quantised Hamiltonian is invariant under its action

$$\hat{\mathscr{T}} \hat{\mathcal{H}} \hat{\mathscr{T}}^{-1} = \hat{\mathcal{H}}. \tag{1.22}$$

If some second quantised Hermitian operator $\hat{O}$ is invariant under the action of $\hat{\mathscr{T}}$ then constraint (1.22) implies

$$\hat{\mathscr{T}} \hat{O}(t) \hat{\mathscr{T}}^{-1} = \hat{\mathscr{T}} e^{i\hat{\mathcal{H}}t} \hat{O} e^{-i\hat{\mathcal{H}}t} \hat{\mathscr{T}}^{-1} = \hat{O}(-t). \tag{1.23}$$

We can derive a constraint on the kernel Hamiltonian from (1.22) and definition (1.20)

$$\begin{aligned}
\hat{\mathscr{T}} \hat{\mathcal{H}} \hat{\mathscr{T}}^{-1} &= \hat{\mathscr{T}} \hat{a}_I^\dagger H_I^J \hat{a}_J \hat{\mathscr{T}}^{-1} \\
&= \hat{\mathscr{T}} \hat{a}_I^\dagger \hat{\mathscr{T}}^{-1} \hat{\mathscr{T}} H_I^J \hat{a}_J \hat{\mathscr{T}}^{-1} \\
&= \hat{\mathscr{T}} \hat{a}_I^\dagger \hat{\mathscr{T}}^{-1} \left(H_I^J \right)^* \hat{\mathscr{T}} \hat{a}_J \hat{\mathscr{T}}^{-1} \\
&= \hat{a}_I^\dagger \left((U_T)_I^K \right)^* \left(H_K^L \right)^* (U_T)_L^J \, \hat{a}_J \\
&= \boldsymbol{\psi}_I^\dagger U_T H^* U_T^\dagger \boldsymbol{\psi}_J \\
&= \hat{\mathcal{H}}.
\end{aligned} \tag{1.24}$$

This leads to the explicit constraint on the kernel Hamiltonian

$$\begin{aligned} U_T H^* U_T^\dagger &= H \\ U_T \mathcal{K} H \mathcal{K}^{-1} U_T^\dagger &= H \\ T H T^{-1} &= H. \end{aligned} \tag{1.25}$$

We retrieve the familiar TR operator form $T = U_T\mathcal{K}$. We can make the link back to the preceding section by asking, what happens if we act the TR operator twice?

$$\begin{aligned} (U_T)^T H U_T^* &= H^* \\ U_T^\dagger (U_T)^T H U_T^* U_T &= U_T^\dagger H^* U_T \\ (U_T^* U_T)^\dagger H U_T^* U_T &= H. \end{aligned} \tag{1.26}$$

Because the second quantised Hamiltonian (1.18) runs over an irreducible representation space, by Schur's lemma $U_T^* U_T$ is some $U(1)$ multiple of the identity matrix, $U_T^* U_T = e^{i\theta}\mathbb{I}$. Using a similar logic as before we have $(U_T)^T = e^{i\theta} U_T$ and by implication $e^{2i\theta} = 1$. This results in two possible outcomes, $U_T^* U_T = \pm\mathbb{I}$. Therefore twice action of the TR operator $\hat{\mathscr{T}}$ on the fermionic operators $\hat{a}_I$ gives $\hat{\mathscr{T}}^2 \hat{a}_I \hat{\mathscr{T}}^{-2} = \pm \hat{a}_I$. An operator $\hat{O}$ constructed from n second quantised fermionic operators transforms as $\hat{\mathscr{T}}^2 \hat{O} \hat{\mathscr{T}}^{-2} = (\pm 1)^n \hat{O}$. So, the final constraint on the TR operator is written

$$\hat{\mathscr{T}}^2 = (\pm 1)^{\hat{N}}, \tag{1.27}$$

where $\hat{N} = \sum_I \hat{a}_I^\dagger \hat{a}_I$ is the total fermion number operator. As before, when $\hat{\mathscr{T}}^2 = -1$ the system supports degenerate Kramers pairs.

Reciprocal space

If a system of fermions is translationally invariant and has periodic boundary conditions it is often useful to rewrite the Hamiltonian in reciprocal space. Let

us expand the index of our second quantised fermionic operators: $\hat{a}_I = \hat{a}_{\boldsymbol{j},\bar{I}}$ where $\boldsymbol{j} \in \mathbb{N}^N$ is a real space position index of a space of dimension N, and $\bar{I}$ are any remaining indices. The Fourier transform of this operator is given by

$$\hat{a}_{\boldsymbol{j},\bar{I}} = \sum_{\boldsymbol{p}} e^{i\boldsymbol{p}\cdot\boldsymbol{j}} \hat{a}_{\boldsymbol{p},\bar{I}}. \tag{1.28}$$

where $\boldsymbol{p}$ is the wave vector confined to the first Brilloiun zone. We note that, by definition, the TR operator negates the wave vector such that $\hat{\mathscr{T}}\boldsymbol{p}\hat{\mathscr{T}}^{-1} = -\boldsymbol{p}$. Taking (1.19) and performing such a transformation leads to

$$\hat{\mathcal{H}} = \sum_{\boldsymbol{p},\boldsymbol{j},\boldsymbol{j}'} \hat{a}^\dagger_{\boldsymbol{p},\bar{I}} e^{-i\boldsymbol{p}\cdot\boldsymbol{j}} H^{\boldsymbol{j}',\bar{J}}_{\boldsymbol{j},\bar{I}} e^{i\boldsymbol{p}\cdot\boldsymbol{j}'} \hat{a}_{\boldsymbol{p},\bar{J}} = \sum_{\boldsymbol{p}} \boldsymbol{\psi}^\dagger_{\boldsymbol{p}} H(\boldsymbol{p}) \boldsymbol{\psi}_{\boldsymbol{p}}. \tag{1.29}$$

The action of the TR operator on (1.29) is given by

$$\begin{aligned}
\hat{\mathscr{T}}\hat{\mathcal{H}}\hat{\mathscr{T}}^{-1} &= \sum_{\boldsymbol{p},\boldsymbol{j},\boldsymbol{j}'} \hat{\mathscr{T}}\hat{a}^\dagger_{\boldsymbol{p},\bar{I}}\hat{\mathscr{T}}^{-1}\hat{\mathscr{T}}e^{-i\boldsymbol{p}\cdot\boldsymbol{j}}\hat{\mathscr{T}}^{-1}\hat{\mathscr{T}}H^{\boldsymbol{j}',\bar{J}}_{\boldsymbol{j},\bar{I}}\hat{\mathscr{T}}^{-1}\hat{\mathscr{T}}e^{i\boldsymbol{p}\cdot\boldsymbol{j}'}\hat{\mathscr{T}}^{-1}\hat{\mathscr{T}}\hat{a}_{\boldsymbol{p},\bar{J}}\hat{\mathscr{T}}^{-1} \\
&= \sum_{\boldsymbol{p},\boldsymbol{j},\boldsymbol{j}'} \hat{\mathscr{T}}\hat{a}^\dagger_{\boldsymbol{p},\bar{I}}\hat{\mathscr{T}}^{-1} e^{-i\boldsymbol{p}\cdot\boldsymbol{j}} \left(H^{\boldsymbol{j}',\bar{J}}_{\boldsymbol{j},\bar{I}}\right)^* e^{i\boldsymbol{p}\cdot\boldsymbol{j}'} \hat{\mathscr{T}}\hat{a}_{\boldsymbol{p},\bar{J}}\hat{\mathscr{T}}^{-1} \\
&= \sum_{\boldsymbol{p},\boldsymbol{j},\boldsymbol{j}'} \hat{a}^\dagger_{\boldsymbol{p},\bar{I}} \left((U_T)^{\bar{K}}_{\bar{I}}\right)^* e^{-i\boldsymbol{p}\cdot\boldsymbol{j}} \left(H^{\boldsymbol{j}',\bar{L}}_{\boldsymbol{j},\bar{K}}\right)^* e^{i\boldsymbol{p}\cdot\boldsymbol{j}'} (U_T)^{\bar{J}}_{\bar{L}} \hat{a}_{\boldsymbol{p},\bar{J}} \\
&= \sum_{\boldsymbol{p},\boldsymbol{j},\boldsymbol{j}'} \boldsymbol{\psi}^\dagger_{\boldsymbol{p}} U_T H^*(-\boldsymbol{p}) U_T^\dagger \boldsymbol{\psi}_{\boldsymbol{p}}.
\end{aligned} \tag{1.30}$$

Therefore the corresponding TR condition on the reciprocal space kernel Hamiltonian is given by

$$TH(-\boldsymbol{p})T^{-1} = H(\boldsymbol{p}). \tag{1.31}$$

1.2.2 Particle-hole symmetry

All finite fermionic systems express a dualism in their formulation. Consider this representation of the fermionic vacuum for a single particle

$$|\varnothing\rangle = \hat{a}\,|1\rangle\,. \tag{1.32}$$

This state behaves as we expect it should

$$\hat{a}^\dagger |\varnothing\rangle = \hat{a}^\dagger \hat{a} |1\rangle = |1\rangle , \quad \hat{a} |\varnothing\rangle = \hat{a}\hat{a} |1\rangle = 0. \tag{1.33}$$

Is there a transformation that exchanges the roles of the creation and annihilation operators while preserving the algebra of (1.33)? We define a second quantised unitary operator $\hat{\Phi} = \hat{a} + \hat{a}^\dagger$ that acts on the fermionic operators as $\hat{\Phi}\hat{a}\hat{\Phi}^{-1} = \hat{a}^\dagger$ and $\hat{\Phi}\hat{a}^\dagger\hat{\Phi}^{-1} = \hat{a}$. The action of this transformation on the vacuum is

$$\begin{aligned} \hat{\Phi} |\varnothing\rangle &= \hat{\Phi}\hat{a} |1\rangle \\ &= \hat{\Phi}\hat{a}\hat{\Phi}^{-1}\hat{\Phi}\hat{a}^\dagger\hat{\Phi}^{-1}\hat{\Phi} |0\rangle \\ &= \hat{a}^\dagger\hat{a} |1\rangle \\ &= \hat{a}^\dagger |0\rangle \equiv |\tilde{\varnothing}\rangle . \end{aligned} \tag{1.34}$$

We find that the fermionic vacuum $|\varnothing\rangle$ is related to a conjugate state $|\tilde{\varnothing}\rangle$ under the exchange of the fermionic creation and annihilation operators. The action of the fermionic operators on this new vacuum state is

$$\hat{a}^\dagger |\tilde{\varnothing}\rangle = \hat{a}^\dagger\hat{a}^\dagger |0\rangle = 0, \quad \hat{a} |\tilde{\varnothing}\rangle = \hat{a}\hat{a}^\dagger |0\rangle = |0\rangle . \tag{1.35}$$

A simple relabeling of the states $|0\rangle \to |1\rangle$ and $|1\rangle \to |0\rangle$ and we retrieve the original algebra given in (1.33) but with the roles of the operators reversed.

Free fermion systems

In much the same way as TR symmetry we can define a general PH symmetry transformation. Given some system of fermions as given by (1.17), (1.18), and (1.19), we define the action of the second quantised PH symmetry operator $\hat{\mathscr{P}}$ as

$$\hat{\mathscr{P}}\hat{a}_I\hat{\mathscr{P}}^{-1} = (U_P^*)_I^J \, \hat{a}_J^\dagger. \tag{1.36}$$

A system is said to be invariant under this transformation if the canonical fermionic anticommutation relations (1.18) are preserved (again implying that $(U_P)_I^J$ is a unitary matrix) and the second quantised Hamiltonian $\hat{\mathcal{H}}$ is invariant under its action

$$\hat{\mathscr{P}}\hat{\mathcal{H}}\hat{\mathscr{P}}^{-1} = \hat{\mathcal{H}}. \tag{1.37}$$

We can derive a condition on the kernel Hamiltonian from condition (1.37), definition (1.36), and (1.18) in the following way

$$\begin{aligned}
\hat{\mathscr{P}}\hat{\mathcal{H}}\hat{\mathscr{P}}^{-1} &= \hat{\mathscr{P}}\hat{a}_I^\dagger H_I^J \hat{a}_J \hat{\mathscr{P}}^{-1} \\
&= \hat{\mathscr{P}}\hat{a}_I^\dagger \hat{\mathscr{P}}^{-1}\hat{\mathscr{P}} H_I^J \hat{\mathscr{P}}^{-1}\hat{\mathscr{P}}\hat{a}_J \hat{\mathscr{P}}^{-1} \\
&= \hat{a}_I \left(U_P\right)_I^K H_K^L \left(U_P^*\right)_L^J \hat{a}_J^\dagger \\
&= -\hat{a}_J^\dagger \left(U_P^*\right)_J^L H_L^K \left(U_P\right)_K^I \hat{a}_I + H_I^I \\
&= -\boldsymbol{\psi}^\dagger U_P H^T U_P^\dagger \boldsymbol{\psi} + \mathrm{Tr}H \\
&= \hat{\mathcal{H}}
\end{aligned} \tag{1.38}$$

From this the condition on the kernel Hamiltonian is stated as

$$\begin{aligned}
U_P H^* U_P^\dagger &= -H \\
U_P \mathcal{K} H \mathcal{K}^{-1} U_P^\dagger &= -H \\
PHP^{-1} &= -H,
\end{aligned} \tag{1.39}$$

where $P = U_P\mathcal{K}$. Using the same arguments as the TR case one can show there are two types of PH transformations

$$\hat{\mathscr{P}}^2 = (\pm 1)^{\hat{N}}, \quad U_P^* U_P = \pm\mathbb{I}. \tag{1.40}$$

The implication of PH symmetry on a system is as follows. The Hamiltonian obeys the time independent Schrödinger equation

$$\hat{\mathcal{H}} \left|\Psi_n\right\rangle = \epsilon_n \left|\Psi_n\right\rangle , \tag{1.41}$$

where $\left|\Psi_n\right\rangle$ and ϵ_n are the eigenvectors and eigenvalues of $\hat{\mathcal{H}}$. (1.41) transforms under the PH operator as follows

$$\begin{aligned} \hat{\mathscr{P}}\hat{\mathcal{H}}\hat{\mathscr{P}}^{-1}\hat{\mathscr{P}} \left|\Psi_n\right\rangle &= E_n \hat{\mathscr{P}} \left|\Psi_n\right\rangle \\ \hat{\mathcal{H}} \left|\tilde{\Psi}_n\right\rangle &= \epsilon_n \left|\tilde{\Psi}_n\right\rangle . \end{aligned} \tag{1.42}$$

The implication of (1.42) is that the presence of PH symmetry implies every eigenstate of $\hat{\mathcal{H}}$, $\left|\Psi_n\right\rangle$, has a conjugate state $\left|\tilde{\Psi}_n\right\rangle = \hat{\mathscr{P}} \left|\Psi_n\right\rangle$ which is also an eigenstate of $\hat{\mathcal{H}}$ with eigenvalue ϵ_n. The kernel Hamiltonian also obeys the time independent Schrödinger equation which transforms under the PH transformation as

$$\begin{aligned} PHP^{-1}P \left|\psi_n\right\rangle &= E_n P \left|\psi\right\rangle \\ -H \left|\tilde{\psi}\right\rangle &= E_n \left|\tilde{\psi}\right\rangle . \end{aligned} \tag{1.43}$$

For each eigenstate $\left|\psi_n\right\rangle$ with energy E_n there exists a conjugate eigenstate $\left|\tilde{\psi}_n\right\rangle = P \left|\psi_n\right\rangle$ with eigenvalue $-E_n$.

Reciprocal space

Using the same procedure as in (1.29) it is possible to show that the PH condition on the reciprocal space kernel Hamiltonian is

$$PH(-\boldsymbol{p})P^{-1} = -H(\boldsymbol{p}). \tag{1.44}$$

1.2.3 Chiral (sublattice) symmetry

Given PH and TR symmetry, a third symmetry suggests itself. The chiral (CH) (sometimes know as sublattice) symmetry transformation $\hat{\mathscr{S}}$ is the product of TR and PH symmetries

$$\hat{\mathscr{S}} = \hat{\mathscr{T}}\hat{\mathscr{P}}. \tag{1.45}$$

In now familiar language, the action of the second quantised chiral (CH) symmetry operator on the fermionic creation and annihilation operators is given by

$$\hat{\mathscr{S}}\hat{a}_I\hat{\mathscr{S}}^{-1} = \left(U_P^\dagger U_T^\dagger\right)_I^J \hat{a}_J^\dagger. \tag{1.46}$$

Using much the same arguments as in the TR and PH cases, the condition on the kernel Hamiltonian is given by

$$U_S H U_S^\dagger = -H, \tag{1.47}$$

where $U_S = U_T U_P$. Furthermore we have $\hat{\mathscr{S}}^2 = (\pm 1)^{\hat{N}}$. A kernel Hamiltonian that obeys CH symmetry has the property that it can always be rotated into block-off-diagonal form. In the basis that U_S is diagonal the kernel Hamiltonian takes the form

$$H = \begin{pmatrix} 0 & D \\ D^\dagger & 0 \end{pmatrix}. \tag{1.48}$$

Finally, if a system breaks both TR and PH symmetry it is still possible for CH symmetry to be preserved.

1.2.4 Bogoliubov de-Gennes systems

Of particular note for us are Bogoliubov de-Gennes (BdG) systems. All superconducting systems are written in this form and they exhibit a set of intrinsic symmetries that come not from the single particle Hamiltonian but from the

many-bodied level. While the basic element of (1.19) is the fermionic operator $\hat{a}_I$, in BdG systems the basic element in the Nambu spinor

$$\hat{\Gamma}_I = \begin{pmatrix} \hat{a}_I \\ \hat{a}_I^\dagger \end{pmatrix} \quad \hat{\Gamma}_I^\dagger = \begin{pmatrix} \hat{a}_I^\dagger & \hat{a}_I \end{pmatrix}. \tag{1.49}$$

where $\left\{\hat{\Gamma}_I, \hat{\Gamma}_J^\dagger\right\} = \delta_{ab}$. The operators $\hat{\Gamma}_I$ and $\hat{\Gamma}_I^\dagger$ are related by the transformation

$$\left(\sigma^x \hat{\Gamma}_I\right)^{\mathrm{T}} = \hat{\Gamma}_I^\dagger. \tag{1.50}$$

The single particle Hamiltonian in terms of Nambu spinors is written

$$\mathcal{H} = \frac{1}{2}\hat{\Gamma}_I^\dagger H_I^J \hat{\Gamma}_J = \Gamma^\dagger H \Gamma \tag{1.51}$$

Because of the relation (1.50) we have

$$\begin{aligned} \mathcal{H} &= \frac{1}{2}\left(\sigma^x \Gamma\right)^{\mathrm{T}} H \left(\Gamma^\dagger \sigma^x\right)^{\mathrm{T}} \\ &= -\frac{1}{2}\Gamma^\dagger \left(\sigma^x H \sigma^x\right)^T \Gamma + \frac{1}{2}\mathrm{Tr}\left(\sigma^x H \sigma^x\right). \end{aligned} \tag{1.52}$$

where σ^x acts on Nambu space. This leads to the condition

$$\sigma^x H^* \sigma^x = -H \tag{1.53}$$

which is the PH symmetry condition. This is completely independent of the form of H, coming only from the behavior of the Nambu spinor. Furthermore, BdG single particle Hamiltonians can be written in the following way

$$H = \begin{pmatrix} \Xi & \Omega \\ \Omega^\dagger & -\Xi \end{pmatrix}, \tag{1.54}$$

where $\Xi = \Xi^\dagger$ corresponds to the normal state, including chemical potential and tunneling terms, and $\Omega = -\Omega^\dagger$ corresponds to the superconducting pairing terms.

1.2.5 Topological invariants

Sometimes a system can be characterised by a topological invariant (topological index). These are quantities that are defined in such a way that they are invariant under adiabatic deformations of the system. Consider a system with Hamiltonian $H(\boldsymbol{\lambda})$ that is parametrised by $\boldsymbol{\lambda} \in \mathbb{R}^N$. The Hamiltonian has ground state $|\psi_g(\boldsymbol{\lambda})\rangle$ which is spectrally separated form the excited states by an energy gap $\Delta E(\boldsymbol{\lambda})$. We can define a quantity $\nu(\boldsymbol{\lambda}) : \mathbb{R}^N \to \mathrm{R}$ where R is a ring of integers. $\nu(\boldsymbol{\lambda})$ is only well defined when $\Delta E(\boldsymbol{\lambda}) \neq 0$. Given some adiabatic evolution of the system $\boldsymbol{\lambda}(t = t_0) \to \boldsymbol{\lambda}(t = t_f)$ the invariant obeys the condition

$$\nu(\boldsymbol{\lambda}(t_0)) = \nu(\boldsymbol{\lambda}(t_f)), \tag{1.55}$$

as long as $\Delta E(t) \neq 0$ for all $t_0 \leq t \leq t_f$. The particular integer ring R that the system's invariant maps to is dependent on the presence and type or absence of PH, TR, and CH symmetries, as well as the number of spatial dimensions. In some cases, particular combinations of these factors mean that it is not possible for a system's invariant to take non-zero values.

Throughout this work many different examples of topological invariants will be discussed from Chern number to the winding number in 1D, 2D, and 3D. In the systems we will be considering, a non-zero topological index can be indicative of topologically protected edge states and non-Abelian quasi-particle excitations.

1.2.6 The classes

The absence, or presence and nature of these symmetries tell us much about the of the system without ever having to look at the details of the Hamiltonian [17]. For example, a system which is TR invariant with $\hat{\mathscr{T}}^2 = 1$ consists of particles with zero or integer spin, while if $\hat{\mathscr{T}}^2 = -1$ then the system's fermions are spinful,

	$\mathscr{T}$	$\mathscr{P}$	$\mathscr{S}$	1	2	3
A	0	0	0	0	$\mathbb{Z}$	0
AIII	0	0	1	$\mathbb{Z}$	0	0
AI	+	0	0	0	0	0
BDI	+	+	1	$\mathbb{Z}$	0	0
D	0	+	0	$\mathbb{Z}_2$	$\mathbb{Z}$	0
DIII	-	+	1	$\mathbb{Z}_2$	$\mathbb{Z}_2$	$\mathbb{Z}$
AII	-	0	0	0	$\mathbb{Z}_2$	$\mathbb{Z}_2$
CII	-	-	1	$\mathbb{Z}$	0	$\mathbb{Z}_2$
C	0	-	0	0	$\mathbb{Z}$	0
CI	+	-	1	0	0	$\mathbb{Z}$

Table 1.1: The symmetry classes of the 10-fold way. The left hand column gives the name of the classes, in the format defined by Altland and Zirnbauer [29]. From the left, the next three columns indicate whether the class obeys TR, PH and CH symmetries. The symbols $+, -, 0, 1$ indicate whether the relevant operator exists and its transformation properties, i.e. $\hat{\mathscr{O}}^2 = \pm 1$. The final three columns indicate, depending on the spatial dimension, to which integer ring the associated topological invariant maps. An entry of 0 implies the invariant is always zero.

i.e. half-integer spin. Superconducting systems with $\hat{\mathscr{P}}^2 = 1$ support spin-triplet pairing, whereas $\hat{\mathscr{P}}^2 = -1$ implies spin-singlet pairing. Furthermore, $\hat{\mathscr{T}}^2 = -1$ implies Kramers' degeneracy [28], while the presence of TR symmetry of either form means the energy spectrum is symmetric about zero energy.

All the possible combinations of symmetries enumerate ten distinct equivalence classes of Hamiltonians, or *symmetry classes*. These classes and their required symmetries are shown in tab. 1.1. The class naming convention is taken from the original Altland and Zirnbauer paper [29], in which the symmetry classes are shown to correspond to different Cartan symmetric spaces. Also shown in tab. 1.1 is the existence (or not) of topologically non-trivial ground states and nature

of a given class' topological index, dependent on the number of spatial dimensions. The topological index for a given class and dimension can take many forms. For example, we shall see that for 2D systems the index can be represented as a Chern number or a winding number, with both representations being equivalent.

1.3 1D topological superconductor

In order to illustrate the essential elements of a topological condensed matter system, we now present a construction and analysis of the simplest superconducting lattice model, the Kitaev wire [30].

1.3.1 Dirac fermions

Given N Dirac fermions, hereby referred to simply as fermions, they can be represented by a set of second quantised fermionic field operators $\{\hat{a}_j\}_{j=1,\ldots,N}$ and their Hermitian conjugate partners $\left\{\hat{a}_j^\dagger\right\}_{j=1,\ldots N}$. They obey the following anticommutation relations

$$\left\{\hat{a}_i, \hat{a}_j^\dagger\right\} = \delta_{ij} \qquad\qquad \left\{\hat{a}_i^{(\dagger)}, \hat{a}_j^{(\dagger)}\right\} = 0 \tag{1.56}$$

where δ_{ij} Kronecker delta function. These operators act on a tensor product of Fock states. A general state of the system, $|\psi\rangle$ can be written as

$$|\psi\rangle = \sum_{n_i=0,1} \left(\alpha_{n_1,\ldots,n_N} \bigotimes_{i=1}^{N} |n_i\rangle \right), \tag{1.57}$$

where $\alpha_{n_1,\ldots,n_N} \in \mathbb{C}$, $\sum_{n_i} |\alpha_{n_1,\ldots,n_N}|^2 = 1$ and

$$\bigotimes_{j=1}^{N} |n_j\rangle = \left(\bigotimes_{j=1}^{N} \left(\hat{a}_j^\dagger\right)^{n_j} \right) \left(\bigotimes_{j=1}^{N} |0\rangle \right). \tag{1.58}$$

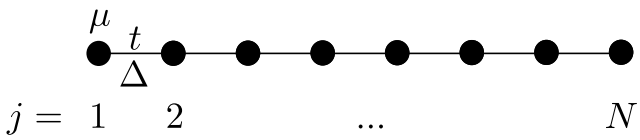

Figure 1.1: A schematic representation of the Kitaev 1D wire. A set of N sites denoted by the black dots and indexed by $j = 1, .., N$ are connected by black lines. To each site we associate a fermion a_j to which we associate a chemical potential $\mu \in \mathbb{R}$. We allow for fermions to tunnel to adjacent sites with amplitude $t \in \mathbb{R}$ and pair with adjacent fermions with amplitude $\Delta \in \mathbb{R}$

1.3.2 Real space tight-binding model

We take a chain of N sites indexed by $j = 1, ..., N$ and to each site we associate a fermion $\hat{a}_j$. To each fermion we associate the same chemical potential μ and we allow for nearest neighbor tunneling and pairing with amplitudes t and Δ respectively, with $\mu, t, \Delta \in \mathbb{R}$. This arrangement is shown in fig. 1.1. With this information we can write down a tight binding Hamiltonian

$$H = \sum_{j=1}^{N} \left(\frac{\mu}{2} \hat{a}_j^\dagger \hat{a}_j - \frac{1}{4} + t \hat{a}_j^\dagger \hat{a}_{j+1} + \Delta \hat{a}_j \hat{a}_{j+1} \right) + \text{H.c.}, \tag{1.59}$$

where H.c. denotes the Hermitian conjugate. The factor of $\frac{1}{4}$ is included for convenience in subsequent calculations and results in an overall energy shift. We have chosen periodic boundary conditions such that $N + 1 \equiv 1$.

1.3.3 Reciprocal space

Because (1.59) is translationally invariant and has periodic boundary conditions, we will transform it into reciprocal space via the Fourier transform. The transformation is defined as

$$\hat{a}_j = \sum_p e^{ipj} \hat{a}_p \qquad\qquad \hat{a}_j^\dagger = \sum_p e^{-ipj} \hat{a}_p^\dagger, \tag{1.60}$$

where $p \in [-\pi, \pi)$, also called the Brillouin zone (BZ). The transformed Hamiltonian is written as

$$H = \sum_p \left[\mu + t\cos(p)\right]\left(\hat{a}_p^\dagger \hat{a}_p - \hat{a}_{-p}\hat{a}_{-p}^\dagger\right) + i\Delta\sin(p)\left(\hat{a}_p\hat{a}_{-p} - \hat{a}_{-p}^\dagger\hat{a}_p^\dagger\right). \quad (1.61)$$

We can now write the Hamiltonian in Bogoliubov-de Gennes form

$$H = \sum_p \boldsymbol{\psi}_p^\dagger h(\boldsymbol{\lambda}, p)\boldsymbol{\psi}_p, \quad (1.62)$$

where $\boldsymbol{\psi}_p = \begin{pmatrix}\hat{a}_p, & \hat{a}_{-p}^\dagger,\end{pmatrix}^{\mathrm{T}}$, $\boldsymbol{\lambda} = \begin{pmatrix}\mu, & \Delta, & t\end{pmatrix}$, and $h(p)$ is a 2×2 Hermitian matrix given by

$$h(\boldsymbol{\lambda}, p) = \begin{pmatrix}\epsilon(\mu, t, p) & \Xi(\Delta, p) \\ \Xi^*(\Delta, p) & -\epsilon(\mu, t, p)\end{pmatrix} \quad (1.63)$$

where $\epsilon(\mu, t, p) = \mu + t\cos(p)$ and $\Xi(\Delta, p) = i\Delta\sin(p)$ and $h(\boldsymbol{\lambda}, p)$ is the kernel Hamiltonian. From the kernel Hamiltonian we can extract many useful quantities such as the energy spectrum and the model's topological invariant, the winding number.

1.3.4 Symmetries

The Kitaev wire obeys both TR and PH (and by implication CH) symmetries. In the basis that (1.62) is written, the PH operator is $P = \sigma^x\mathcal{K}$ while the TR operator is given by $T = \sigma^z\mathcal{K}$. These two operators satisfy the symmetry equations

$$Th(\boldsymbol{\lambda}, \boldsymbol{p})T^{-1} = h(\boldsymbol{\lambda}, -\boldsymbol{p}) \quad Ph(\boldsymbol{\lambda}, \boldsymbol{p})P^{-1} = -h(\boldsymbol{\lambda}, -\boldsymbol{p}) \quad (1.64)$$

As we have the further relations $P^2 = 1$ and $T^2 = 1$, referring to Tab. 1.1, we find that the Kitaev wire lies in the symmetry class BDI. We could introduce some new couplings to our Hamiltonian, for example next nearest neighbor complex tunneling, that break TR symmetry which would place the model in the class D.

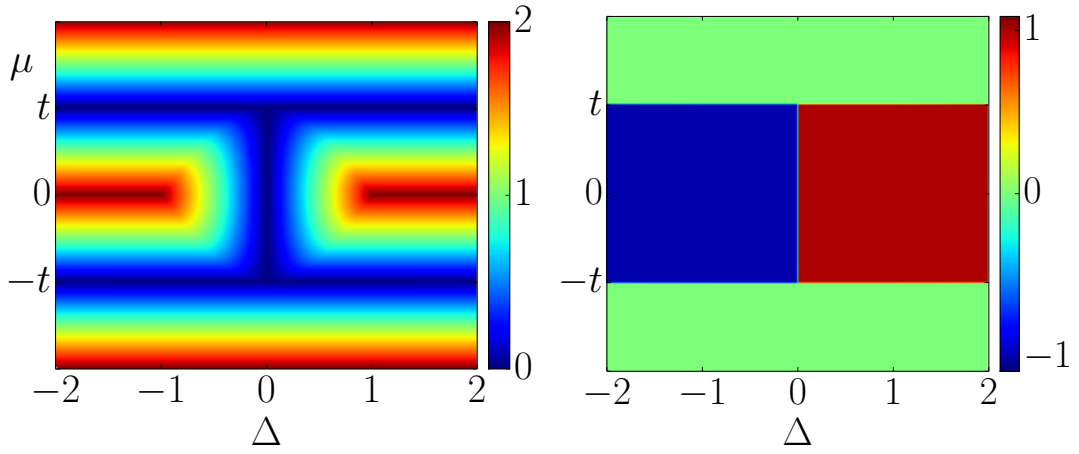

Figure 1.2: *Left*: The energy gap, ΔE of the Kitaev wire as a function of the chemical potential, μ, and the superconducting order parameter Δ. The data was obtained via exact diagonalisation of (1.63). *Right*: The winding number, $\nu_{1\mathrm{D}}$, of the Kitaev wire. Each gapped phase is separated by a gapless line as depicted in the diagram of the gap on the left. The data was obtained via numerical evaluation of (1.69).

1.3.5 Energy spectrum and ground state

The model supports a pair of eigenvalues and eigenvectors, $E^{\pm}(\boldsymbol{\lambda}, p)$ and $|\psi_{\pm}(\boldsymbol{\lambda}, p)\rangle$. As the model is PH symmetric the spectrum will be symmetric about zero energy. This is confirmed when we look at the analytic expression for the eigenvalues of (1.63),

$$E^{\pm}(\boldsymbol{\lambda}, p) = \pm\sqrt{|\epsilon(\mu, t, p)|^2 + |\Xi(\Delta, p)|^2}. \tag{1.65}$$

We define the energy gap, denoted $\Delta E(\boldsymbol{\lambda})$, to be

$$\Delta E(\boldsymbol{\lambda}) = 2\min_p \left|E^{+}(\boldsymbol{\lambda}, p)\right|. \tag{1.66}$$

In fig. 1.2 *Left* we plot $\Delta E(\boldsymbol{\lambda})$ as a function of μ and Δ. The diagram is separated into four regions where $\Delta E(\boldsymbol{\lambda}) \neq 0$ which are separated by lines where $\Delta E(\boldsymbol{\lambda}) = 0$.

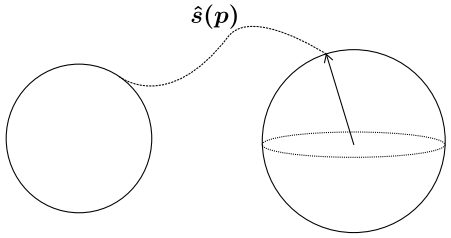

Figure 1.3: A schematic representation of the behavior of vector $\hat{\boldsymbol{s}}$. As the toroidal Brillouin Zone is spanned, the 3-vector $\hat{\boldsymbol{s}}$ winds around the unit 2-sphere an integer number of times.

We take the system to be at half filling. This means that all of the negative energy states are occupied and the ground state is eigenstate associated with $E^{-}(\boldsymbol{\lambda}, p)$, $|\psi_g(\boldsymbol{\lambda}, p)\rangle = |\psi_{-}(\boldsymbol{\lambda}, p)\rangle$.

1.3.6 Winding number

The topological phase of the system is determined by the winding number, $\nu_{1\mathrm{D}}$. In order to define $\nu_{1\mathrm{D}}$ we must first define a unit vector $\hat{\boldsymbol{s}}(p)$ which parametrises the kernel Hamiltonian

$$h(\boldsymbol{\lambda}, p) = \boldsymbol{s}(\boldsymbol{\lambda}, p) \cdot \boldsymbol{\sigma} = |\boldsymbol{s}(\boldsymbol{\lambda}, p)|\, \hat{\boldsymbol{s}}(\boldsymbol{\lambda}, p) \cdot \boldsymbol{\sigma} \tag{1.67}$$

where $\boldsymbol{\sigma} = \begin{pmatrix} \sigma^x & \sigma^y & \sigma^z \end{pmatrix}^{\mathrm{T}}$ and $\hat{\boldsymbol{s}}(\boldsymbol{\lambda}, p) : T^1 \to S^2$. The vector $\hat{\boldsymbol{s}}(\boldsymbol{\lambda}, p)$ is a map between the unit circle that is the BZ and the unit 2-sphere. In the case of the Kitaev wire we have

$$\hat{\boldsymbol{s}}(\boldsymbol{\lambda}, p) = \frac{1}{\sqrt{|\Xi(\boldsymbol{\lambda}, p)|^2 + |\epsilon(\boldsymbol{\lambda}, p)|^2}} \begin{pmatrix} 0 \\ \Xi(\Delta, p) \\ \epsilon(\mu, t, p) \end{pmatrix}. \tag{1.68}$$

We define $\nu_{1\mathrm{D}} : \mathbb{R}^3 \to \mathbb{Z}$ as

$$\nu_{1\mathrm{D}}(\boldsymbol{\lambda}) = \int_{\mathrm{BZ}} dp \;\; \boldsymbol{\theta}(\boldsymbol{\lambda}, p) \cdot \hat{\boldsymbol{u}}(\boldsymbol{\lambda}, p), \tag{1.69}$$

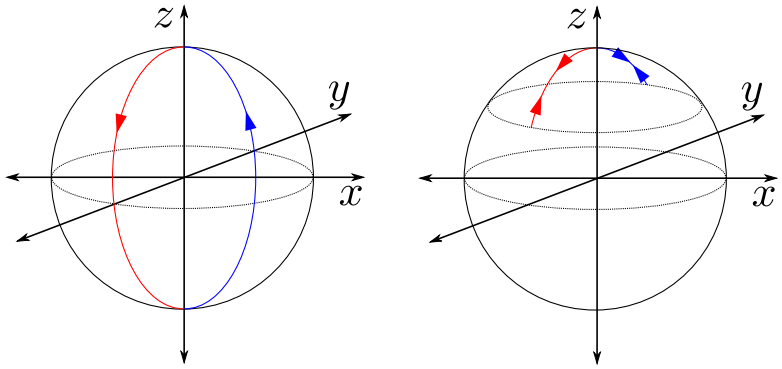

Figure 1.4: The winding of $\hat{\boldsymbol{s}}(\boldsymbol{\lambda}, p)$ for the Kitaev wire. The blue and red lines differentiate the paths for p and $-p$. *Left*: The case when $|\mu| > |t|$. The vector passes through both poles of S^2 giving $\nu_{1D} = \pm 1$ depending on the sign of Δ. *Right*: The case when $|\mu| < |t|$. The vector passes through the same pole twice. Because $\Xi(\boldsymbol{\lambda}, p)$ is odd in p, the contributions from the $\pm p$ paths cancel giving $\nu_{1D} = 0$.

where $\boldsymbol{\theta}(\boldsymbol{\lambda}, p) = \hat{\boldsymbol{s}}(\boldsymbol{\lambda}, p) \times \frac{\partial}{\partial_p} \hat{\boldsymbol{s}}(\boldsymbol{\lambda}, p)$ and $\hat{\boldsymbol{u}}_i(\boldsymbol{\lambda}, p) = \frac{|\theta_i(\boldsymbol{\lambda}, p)|}{|\boldsymbol{\theta}(\boldsymbol{\lambda}, p)|}$. Integral (1.69) counts the number of times the vector $\hat{\boldsymbol{s}}(\boldsymbol{\lambda}, p)$ winds around S^2 as the BZ is spanned.

We can gain some intuition about the behavior of (1.69) by studying the behavior of (1.68) as p varies. First we note that $\hat{\boldsymbol{s}}(\boldsymbol{\lambda}, \pm\pi) = \operatorname{sgn}[-\mu + t]\, \hat{\boldsymbol{z}}$ while $\hat{\boldsymbol{s}}(\boldsymbol{\lambda}, 0) = \operatorname{sgn}[\mu + t]\, \hat{\boldsymbol{z}}$, where $\hat{\boldsymbol{z}}$ is the unit vector pointing in the z direction. Therefore if $|\mu| > |t|$ then $\hat{\boldsymbol{s}}(\boldsymbol{\lambda}, p)$ will pass through both poles of S^2. Whereas if $|\mu| < |t|$ then $\hat{\boldsymbol{s}}(\boldsymbol{\lambda}, p)$ passes through the same pole twice. When we combine this with the fact that $\Xi(\boldsymbol{\lambda}, p)$ is an odd periodic function of p we have two distinct cases for the path of $\hat{\boldsymbol{s}}$, as shown in Fig. 1.4. The sign of Δ affects the sign of the winding number by changing the orientation of the path $\hat{\boldsymbol{s}}(\boldsymbol{\lambda}, p)$ follows.

Fig. 1.2 *right* depicts the winding number for the Kitaev wire as a function of μ and Δ and t. The figure was produced via direct numerical evaluation of (1.69). There are two distinct topological phases with $\nu = \pm 1$ and two separated

trivial phases with $\nu = 0$. The phase transition between the topologically trivial phases and the non-trivial phases occurs at $|\mu| = |t|$ as expected from our earlier analysis. Comparing with Fig. 1.2 *left*, the winding number is invariant within each gapped phase, only changing value when $\Delta E(\boldsymbol{\lambda}) = 0$. This can be understood by looking at the definition of $\hat{\boldsymbol{s}}(\boldsymbol{\lambda}, p)$. Comparing (1.65) and (1.68) we see that $|\boldsymbol{s}(\boldsymbol{\lambda}, p)| = E^{\pm}(\boldsymbol{\lambda}, p)$. Therefore $\hat{\boldsymbol{s}}(\boldsymbol{\lambda}, p)$ is singular for some value of p and $\boldsymbol{\lambda}$. These singular points coincide with the points for which $\Delta E(\boldsymbol{\lambda}) = 0$.

1.3.7 Majorana fermions and edge states

A natural basis for describing topological superconductors is the Majorana basis. It is related to the Dirac fermion basis in the following way

$$\hat{a}_j = \frac{\gamma_{1,j} + i\gamma_{2,j}}{2} \qquad\qquad \hat{a}_j^\dagger = \frac{\gamma_{1,j} - i\gamma_{2,j}}{2} \tag{1.70}$$

where $\gamma_{\alpha,j}$ are the Majorana operators. They are self dual, i.e. $\gamma_{\alpha,j} = \gamma_{\alpha,j}^\dagger$, and they obey the following commutation relations

$$\{\gamma_{\alpha,i}, \gamma_{\beta,j}\} = 2\delta_{\alpha\beta}\delta_{ij}, \tag{1.71}$$

implying that $\gamma_{\alpha,j}^2 = 1$. We can rewrite (1.59) in the Majorana basis to get

$$H = \frac{i}{2}\sum_{j=1}^{N} \left[\mu\gamma_{1,j}\gamma_{2,j} + (t+\Delta)\,\gamma_{2,j}\gamma_{1,j+1} + (-t+\Delta)\,\gamma_{1,j}\gamma_{2,j+1}\right]. \tag{1.72}$$

Through judicious choices of μ, Δ and t we can eliminate different terms in (1.72). If we break the periodic boundary conditions, the different choices of the coupling configuration are shown in fig. 1.5. If we pick a point in parameter space that is in the trivial phase, as depicted in fig. 1.2, such as $\mu > 0$ and $\Delta = t = 0$ then (1.72) becomes $H = \frac{i}{2}\sum_j \mu\gamma_{1,j}\gamma_{2,j}$ and the configuration becomes that of fig. 1.5 *middle*. However if we pick a point in the non-trivial phase, such as $\mu = 0$ and

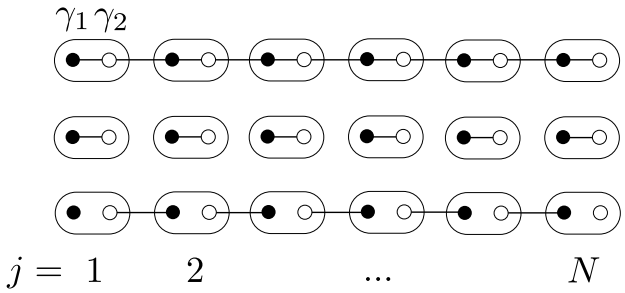

Figure 1.5: *Top*: The Kitaev chain drawn in the Majorana basis. Each site j supports two Majorana fermions $\gamma_{1,j}$ and $\gamma_{2,j}$. *Middle*: The Majorana chain with $\mu > 0$ and $\Delta = t = 0$, leading to the Majoranas on the same site being paired together. This point in parameter space is in the trivial phase with $\nu_{1\mathrm{D}}(\boldsymbol{\lambda}) = 0$. *Bottom* The Majorana chain with $\mu = 0$ and $\Delta = t > 0$, leading to Majoranas on adjacent sites being paired together. Due to the open boundary conditions, there are unpaired Majorana fermions at each end of the wire.

$\Delta = t > 0$, then (1.72) becomes $H = it \sum_j \gamma_{2,j}\gamma_{1,j+1}$ and as depicted in fig. 1.5 (bottom) we are left with two unpaired Majorana fermions, one at each end of the chain. These two Majoranas do not appear in the modified Hamiltonian.

If we compute the spectrum of the real space Hamiltonian with open boundary conditions, when the system is in the topological phase a pair of mid gap states appear. In the limit of an infinite chain length, these states have zero energy. They correspond to the two unpaired Majorana fermions at each end of the chain and are robust against disorder. In the limit of a finite length chain, the states exponentially decay from the boundary into the bulk of the chain.

1.3.8 Summary

The Kitaev wire is a canonical example of a topological superconductor. It exhibits the basic characteristics that the vast majority of topological insulating and superconducting systems share. The phase diagram of the model supports a

number of gapped phases separated by gapless regions. In each gapped phase, a topological index can be defined such that it is invariant within that region. In order to change the index, the system's energy gap must close. If the topological index is non-trivial, the system supports edge states that are robust to disorder as long as the gap remains open. It is models with these characteristics that shall be studied in the subsequent chapters.

As we shall see, there are a whole host of other effects that this interesting class of models exhibit. Notions of bulk-boundary correspondence and topologically protected defects (of which the Majorana edge states in the Kitaev wire are just one type) will both be studied in detail later in this work.

1.4 Anyons

1.4.1 Particles exchange statistics and Abelian anyons

Traditionally, particles can be divided into two distinct classes based on their statistics under exchange. Consider system of N indistinguishable particles $\{\zeta^i\}$ located at positions $\{\boldsymbol{r}_i\}_{i=1,...,N}$, where $\boldsymbol{r}_i \in \mathbb{R}^3$. We denote the many body wave function as $\psi(\zeta^1_{\boldsymbol{r}_1}, ..., \zeta^i_{\boldsymbol{r}_i}, \zeta^j_{\boldsymbol{r}_j}, ..., \zeta^N_{\boldsymbol{r}_N})$. We define an exchange operator $\mathcal{R}$ that exchanges the positions of two of the particles

$$\mathcal{R}\psi(\zeta^1_{\boldsymbol{r}_1}, ..., \zeta^i_{\boldsymbol{r}_i}, \zeta^j_{\boldsymbol{r}_j}, ..., \zeta^N_{\boldsymbol{r}_N}) = \mathcal{U}\psi(\zeta^1_{\boldsymbol{r}_1}, ..., \zeta^i_{\boldsymbol{r}_j}, \zeta^j_{\boldsymbol{r}_i}, ..., \zeta^N_{\boldsymbol{r}_N}), \tag{1.73}$$

where $\mathcal{U}$ is some $U(1)$ phase factor. If one acts the exchange operator twice we have

$$\mathcal{R}^2\psi(\zeta^1_{\boldsymbol{r}_1}, ..., \zeta^i_{\boldsymbol{r}_i}, \zeta^j_{\boldsymbol{r}_j}, ..., \zeta^N_{\boldsymbol{r}_N}) = \mathcal{U}^2\psi(\zeta^1_{\boldsymbol{r}_1}, ..., \zeta^i_{\boldsymbol{r}_i}, \zeta^j_{\boldsymbol{r}_j}, ..., \zeta^N_{\boldsymbol{r}_N}). \tag{1.74}$$

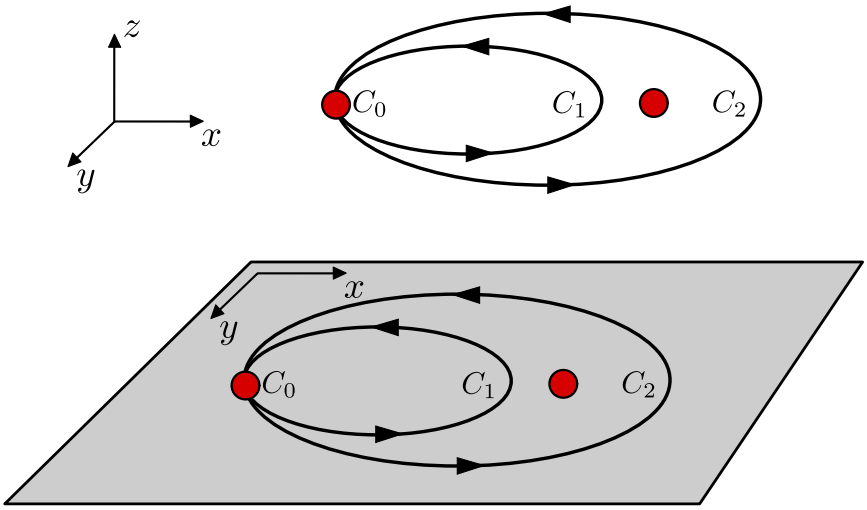

Figure 1.6: *Top*: The exchange of two identical particles, twice, in three spatial dimensions. Paths C_2, C_1 and the trivial path C_0 are shown. Because there exist a continuous mapping between all of the paths they are homotopically equivalent. *Bottom*: The exchange of two particles restricted to two spatial dimensions. While it is possible to continuously deform $C_1 \to C_0$, C_2 is homotopically inequivalent.

From the reference from of one of the two particles such a double exchange is equivalent to one particle executing a loop around another. Shown in Fig. 1.6 *top* is such a loop, denoted C_2. Also shown in Fig 1.6 *top* are two other paths: C_1 is a loop of one particle that does not enclose the other; C_0 is the trivial path. In $\mathbb{R}^3$ there exist continuous maps $\eta : C_2 \mapsto C_1$ and $\eta' : C_1 \mapsto C_0$. One can intuitively see this as bringing C_2 over the top or underneath of the particle it 'encloses'. One can view this as a result of point particles embedded in $\mathbb{R}^3$ being a simply-connected space. As such all paths are said to be homotopically equivalent. Given that C_2 is equivalent to the trivial path C_0, (1.74) implies that $\mathcal{U}^2 = 1$. The $U(1)$ phase factor $\mathcal{U}$ can take two values

$$\text{Bosons}: \ \mathcal{U} = 1 \qquad \text{Fermions}: \ \mathcal{U} = -1. \tag{1.75}$$

What if we embed our particles in $\mathbb{R}^2$? The same double exchange operation

when performed in $\mathbb{R}^2$ is shown in Fig. 1.6 *bottom*. Such an embedding is equivalent to puncturing the plane at the locus of each particle. Therefore adding a particle turns the simply-connected space of plain old $\mathbb{R}^2$ into a multiply-connected space. In this picture there still exists a continuous map $\eta' : C_1 \mapsto C_0$. However there does not exist a continuous maps between C_1 and C_2. As such C_2 is homotopically inequivalent to C_1 and C_0. This implies a continuum of solutions to (1.74)

$$\text{Anyon}: \ \mathcal{U} = e^{i\theta}, \quad \theta \in (0, 2\pi]. \tag{1.76}$$

The cases of $\theta = 0, \pi$ correspond to fermions and bosons. However all other solutions are correspond to anyons.

The discussion above can also be described in terms of groups. The exchange of N identical particles embedded in $\mathbb{R}^3$ reduces to the permutation group S^N. N identical particles embedded in $\mathbb{R}^2$ reduces to the much richer braid group $\mathcal{B}_N$. The elements of the braid group correspond to an equivalence class of paths that can be continuously mapped to each other. In the example given above, C_0 and C_1 are represented by the same group element, the identity. To N particles we associate $N-1$ generators $\mathcal{R}_i$ which correspond to the clockwise exchange of particles i and $i+1$. The inverse of each generator $\mathcal{R}_i^{-1}$ corresponds to anticlockwise exchange of particles i and $i+1$. The generators obey these relations [32]

$$\begin{aligned} \mathcal{R}_i\mathcal{R}_j &= \mathcal{R}_j\mathcal{R}_i, \quad |i-j| \leq 2 \\ \mathcal{R}_i\mathcal{R}_{i+1}\mathcal{R}_i &= \mathcal{R}_{i+1}\mathcal{R}_i\mathcal{R}_{i+1}, \quad 1 \leq i \leq N-1. \end{aligned} \tag{1.77}$$

The distinction between S_N and $\mathcal{B}_N$ is that $\mathcal{R}^2 \neq 1$. This means that while the number of elements in the permutation group is $N!$, the size of the braid group is infinite. In the case described above, the elements of the braid group are the phases gained by the many-body wave function of the system, $e^{im\theta}$, where m is

the number of times the particles are exchanged. If the order of exchanges does not effect the final state of the system then the group is said to be *Abelian* and correspond to Abelian anyons.

1.4.2 Non-Abelian anyons

Consider a many-body system with a ground state $|\Psi\rangle = \sum_{i=1}^{g} \alpha_i |\psi_i\rangle$, where $\alpha_i \in \mathbb{C}$ and $|\psi_i\rangle_{i=1,\ldots,g}$ are g degenerate eigenstates. The action of two generators of the braid group on $|\Psi\rangle$ is written

$$\mathcal{R}\mathcal{R}' |\Psi\rangle = \mathcal{U}\mathcal{U}' |\Psi\rangle . \tag{1.78}$$

The elements of the braid group in this instance are $\mathcal{U}, \mathcal{U}' \in U(n)$ that act on the degenerate subspace of eigenstates, e.g. $\mathcal{U} = \sum_{i,j} \beta_{ij} |\psi_j\rangle \langle\psi_i|$. If there exists a $\mathcal{U}$ and $\mathcal{U}'$ such that $[\mathcal{U}, \mathcal{U}'] \neq 0$ then the particles are *non-Abelian*. Systems that consist of such particles admit non-trivial unitary transformations on their ground state under the exchange of particles. Indeed systems of this nature *only* admit such transformations when braiding the constituent non-Abelian anyons. It is not possible to define a local operator that performs the same operation. Therefore it is possible to encode quantum information in such a state which is robust to perturbative local interactions with its environment.

Anyon models come an all shapes and sizes, but every anyon model must have three key elements (all of which will be defined subsequently):

- A set of particle types.
- A set of fusion rules.
- A set of braid statistics.

For reasons which will become clear subsequently, we shall use the Ising anyon model as the working example. The Ising anyon model has three types of particle

$$\begin{aligned} 1 &: \text{ Vacuum} \\ \psi &: \text{ Fermion} \\ \sigma &: \text{ Anyon.} \end{aligned} \tag{1.79}$$

The 'non-trivial' element in this set is the σ particle. If we have a set of these particles we can always take two sufficiently far away from the others and consider their composite. This process is called *fusion*. It is similar to the notion in superconducting systems where we have phonon mediated electron-electron (fermion-fermion) pairing which can be treated as a composite boson. In much the same way we can define the fusion, also known as a fusion channel, of all of the particle types in the Ising anyon model

$$\begin{aligned} 1 \times x &= x, \quad x = 1, \psi, \sigma \\ \psi \times \psi &= 1 \\ \sigma \times \psi &= \sigma \\ \sigma \times \sigma &= 1 + \psi, \end{aligned} \tag{1.80}$$

where '$\times$' denotes the action of fusing two particles. The symbol '$+$' implies a multiple possible fusion outcomes, i.e. the fusion of two σ particles can result in either a 1 or a ψ particle. This ambiguity in the fusion outcome of the σ particles means that that model is non-Abelian.

Consider four σ particles, we can construct a 2-dimensional Hilbert space based on the result of fusing them pairwise

$$\begin{aligned} &|(\sigma_1 \times \sigma_2) \to 1 : (\sigma_3 \times \sigma_4) \to 1\rangle \equiv |0\rangle \\ &|(\sigma_1 \times \sigma_2) \to \psi : (\sigma_3 \times \sigma_4) \to \psi\rangle \equiv |1\rangle \,. \end{aligned} \tag{1.81}$$

Alternatively we could construct the Hilbert space in another way

$$|(\sigma_1 \times \sigma_2) \to 1 : (\sigma_3 \times \sigma_4) \to \psi\rangle \equiv |0\rangle$$
$$|(\sigma_1 \times \sigma_2) \to \psi : (\sigma_3 \times \sigma_4) \to 1\rangle \equiv |1\rangle \tag{1.82}$$

We can view these two formulations a orthogonal bases as the total fusion outcome in both cases is different. While the total fusion outcome of (1.81) is 1, the total fusion outcome of (1.82) is ψ. Given one of the two bases (1.81) or (1.82) we can fuse the anyons in a different order, for example $|(\sigma_1 \times (\sigma_2 \times \sigma_3)) \times \sigma_4\rangle$. While the total fusion outcome must always be preserved, using (1.79) we can show: given some set of anyons with a given total fusion outcome there are multiple ways of fusing them together to achieve said outcome. Consider the following

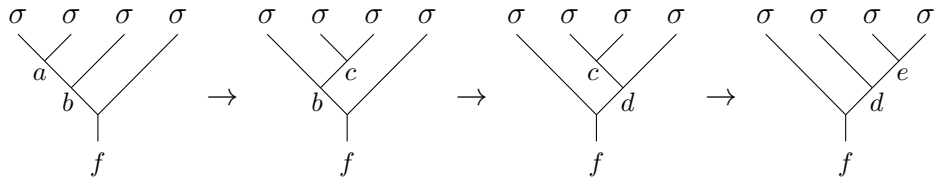

(1.83)

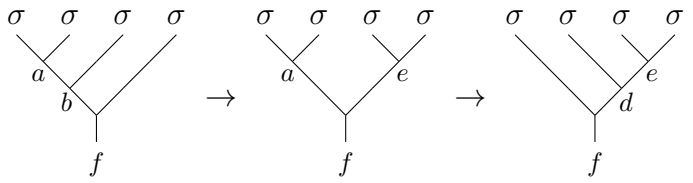

(1.84)

Each diagram shows a particular ordering of the fusions of four σ particles to some final fusion outcome f. Each arrow corresponds to changing the order in which the anyons are fused by a single *F-move*. Both (1.83) and (1.84) show a sequence of F-moves that change from the fusion ordering of the left to the fusion ordering on the right. The initial and final orderings are the same in both cases, but the sequence of F-moves in each case is different. We can represent an

F-move with a matrix element in the following way

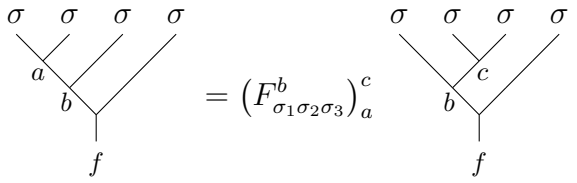

(1.85)

where the matrix $F^{b}_{\sigma\sigma\sigma}$ is the F-matrix containing all possible fusion orderings of three σ particles to a final outcome b. In the case of the Ising anyons, examination of (1.80) finds that b must always be a σ particle. Axiomatic identification of (1.83) and (1.84) gives rise to the pentagon equation

$$\left(F^{f}_{\sigma\sigma e}\right)^{d}_{a}\left(F^{f}_{a\sigma\sigma}\right)^{e}_{b}=\sum_{c=1,\psi}\left(F^{d}_{\sigma\sigma\sigma}\right)^{e}_{c}\left(F^{f}_{\sigma c\sigma}\right)^{d}_{b}\left(F^{b}_{\sigma\sigma\sigma}\right)^{c}_{a} \tag{1.86}$$

which provides a relation between all possible F-matrices of the model. By solving (1.85) for all values of $f=1,\psi,\sigma$ one finds the F-matrix for the model

$$F^{\sigma}_{\sigma\sigma\sigma}=\frac{1}{\sqrt{2}}\begin{pmatrix}1 & 1\\ 1 & -1\end{pmatrix}. \tag{1.87}$$

We can apply the F-matrix to the basis state (1.81)

$$\begin{aligned}F^{\sigma}_{\sigma\sigma\sigma}\left|(\sigma_1\times\sigma_2)\to 1:(\sigma_3\times\sigma_4)\to 1\right\rangle&=\frac{1}{\sqrt{2}}\begin{pmatrix}1 & 1\\ 1 & -1\end{pmatrix}|0\rangle=\frac{1}{\sqrt{2}}\left(|0\rangle+|1\rangle\right)\\ F^{\sigma}_{\sigma\sigma\sigma}\left|(\sigma_1\times\sigma_2)\to\psi:(\sigma_3\times\sigma_4)\to\psi\right\rangle&=\frac{1}{\sqrt{2}}\begin{pmatrix}1 & 1\\ 1 & -1\end{pmatrix}|1\rangle=\frac{1}{\sqrt{2}}\left(|0\rangle-|1\rangle\right).\end{aligned} \tag{1.88}$$

The F-matrix is a transformation between two orthogonal bases. As previously discussed, anyons can acquire a non-trivial phase factor under exchange. We can represent the exchange of anyons in diagrammatic form

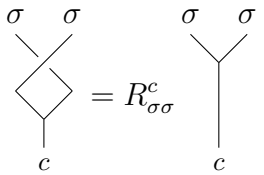

(1.89)

where $R^c_{\sigma\sigma}$ is the phase gained by the wave function when two σ particles with fusion outcome c are braided with one another. There are a set of quantities R^c_{ab}, $a, b = 1, \psi, \sigma$, that together form the *R-matrix* which fully characterises the phases gained under the exchange of all particles in the model. We can combine this formalism with the F-matrix and construct another pair for transformations

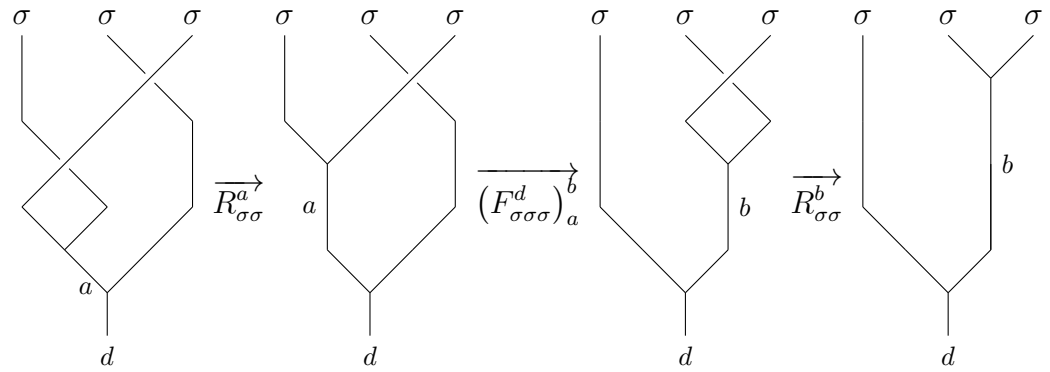

(1.90)

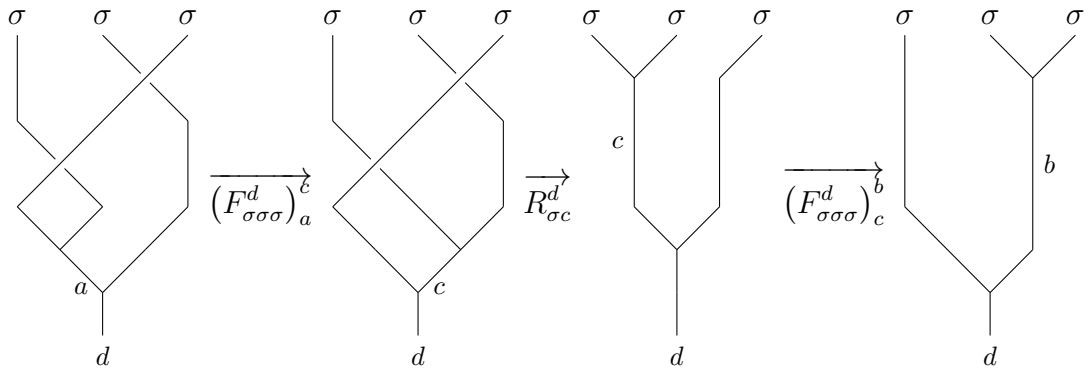

(1.91)

Again we take (1.90) and (1.91) to be identical operations. This gives rise to the hexagon equation

$$\sum_{c=1,\psi} \left(F^d_{\sigma\sigma\sigma}\right)^c_a R^d_{\sigma c} \left(F^d_{\sigma\sigma\sigma}\right)^b_c = R^a_{\sigma\sigma} \left(F^d_{\sigma\sigma\sigma}\right)^b_a R^b_{\sigma\sigma}. \tag{1.92}$$

Solving this equation using the F-matrix gives the explicit form of the R-matrix

for the Ising anyon model

$$R_{\sigma\sigma} = e^{-i\frac{\pi}{8}} \begin{pmatrix} 1 & 0 \\ 0 & i \end{pmatrix}. \tag{1.93}$$

Consider the following problem: we create two pairs of σ particles from the vacuum and braid one particle from each pair with each other and then fuse the original pairs back together

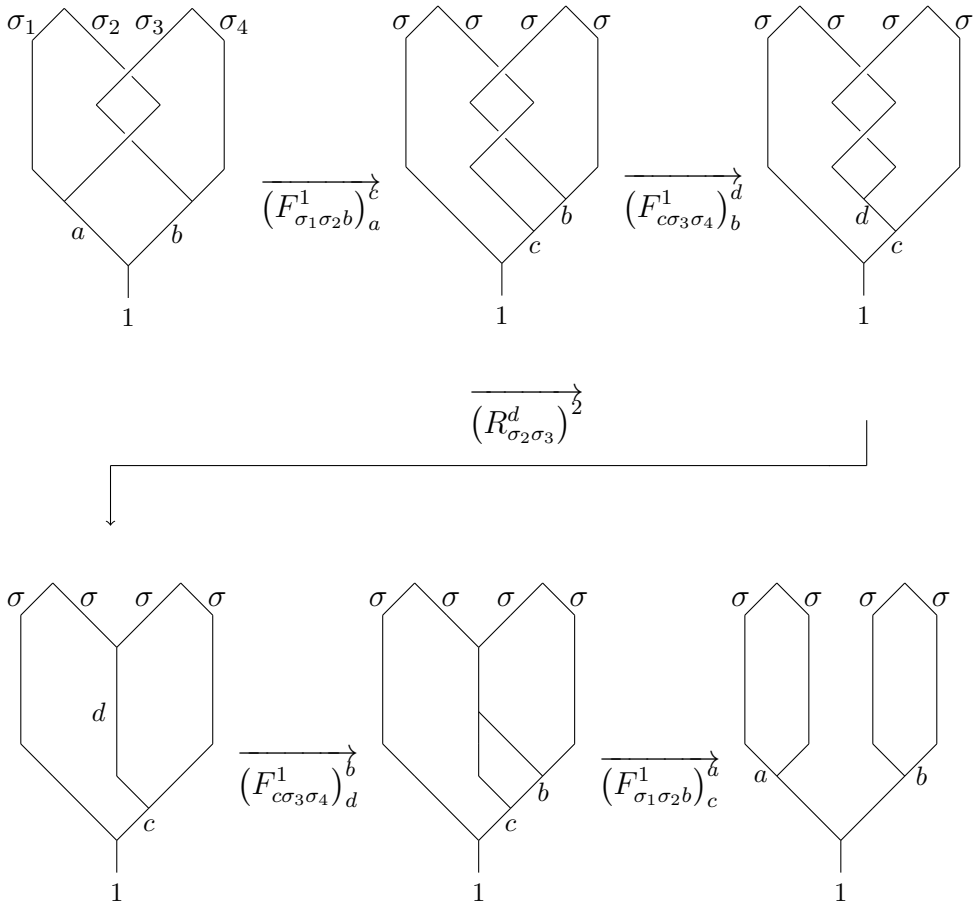

(1.94)

The process shown in (1.94) is equivalent to

$$F^{-1}R^2F\,|1\rangle = \frac{1}{\sqrt{2}}\begin{pmatrix} 1 & 1 \\ 1 & -1 \end{pmatrix} e^{-i\frac{\pi}{4}} \begin{pmatrix} 1 & 0 \\ 0 & -1 \end{pmatrix} \frac{1}{\sqrt{2}}\begin{pmatrix} 1 & 1 \\ 1 & -1 \end{pmatrix} |0\rangle = e^{-i\frac{\pi}{4}}\,|1\rangle \tag{1.95}$$

which is a bit flip operation. The unitary matrix $B = F^{-1}R^2F$ is the braiding operator. We have demonstrated that Ising anyons can be used to store quantum

information. Furthermore, braiding the anyons around each other can result in unitary transformations on their Hilbert space.

The Ising anyon model is the simplest non-Abelian anyon model. More complex models such as Fibonacci anyons provide a richer set of braiding statistics. It is possible to show that the algebra of Majorana fermions is isomorphic to that of the Ising anyons [33]. If Majorana fermions can be created and controlled in physical systems, it would be possible to create topologically protected quantum memories and potentially perform fault tolerant quantum computation.

1.5 Numerical methods

Throughout this work various numerical calculations are performed. These range from computing the spectrum and eigenstates of a given Hamiltonian to computing the winding or Chern number of a system with a given ground state. I now present a short summary of the methods used in these computations.

Chapter 2

The numerical case studies revolved around computing the phase diagram using the Chern number and decomposed winding number methods.

- The eigenstates and eigenvalues were computed using exact diagonalisation via singular value decomposition (SVD).
- The Chern number was computed via the method given in [34].
- The winding numbers were computed by explicit numerical evaluation of the relevant integral over a discretised Brillouin zone using the eigenstates as computed from SVD.

Chapter 3

The study of the models in this chapter revolve around computing the phase diagram, spectrum and edge states.

- The eigenstates and eigenvalues in both the fully periodic and open boundary cases were computed using exact diagonalisation via singular value decomposition SVD.
- The winding numbers were computed by explicit numerical evaluation of the relevant integral over a discretised Brillouin zone using the eigenstates as computed from SVD.

Chapter 4

The need to study large systems in real space requires the use of techniques distinct from the previous chapters.

- The zero energy eigenstates and eigenvalues (edge states) were computed using a Lanczos algorithm.

1.6 Summary

This work is divided into four subsequent chapters. Chapter 2 presents work done on developing a means of experimentally measuring the Chern number in fermionic systems that have four species of particle. Chapter 3 looks at a set of new models that exhibit topological superconductivity in three spatial dimensions. Chapter 4 studies the effect of introducing defects onto the boundary of these new models, resulting in the dimensional reduction of Majorana surface states. Finally, Chapter 5 is a brief summary of the thesis and a proposal for future work.

Chapter 2

Decomposition of the Chern Number in 2D Systems

The discovery and classification of non-interacting fermionic condensed matter systems via their symmetries has been one of the most interesting developments in recent years. So called symmetry protected topological (SPT) order has presented physicists with a wealth of new physical phenomena, some of which have the potential for use in performing fault tolerant quantum computation [35, 36, 32, 33]. A given single particle Hamiltonian's adherence, and nature of that adherence, to three types of symmetries, time-reversal, particle-hole (PH), and chrial, place it in one of ten equivalence classes [18, 20, 17]. Models that fall into one of these categories have the potential to support a set of topologically protected degenerate ground states, depending on whether the system is in a topologically non-trivial phase.

The key indicator of a systems topological phase is its invariant. There exist a wide variety of topological invariants that characterise the phases of many different models, where the specific form of the invariant is determined by the symmetries of the system. One of the most recognisable is the so called TKNN

number [5, 16] of the integer quantum Hall effect; it is proportional to the Hall conductivity. While such a system's ground state is gapped from the excited states, continuous adiabatic transformations of the system do not change the value of the invariant. Only by closing the gap and re-opening can the TKNN number change. Indeed, if the system at two points in phase space can be adiabatically deformed to one another they are considered to be topologically equivalent. This typifies the behavior of topological invariants of all kinds.

A non-trivial topological number can be indicative of a number of interesting phenomena. It can imply the presence of topologically protected edge states; such states live at the boundary of an open system and are robust to perturbation as long as the bulk energy gap is maintained. The Kitaev one dimensional topological superconductor [30] is characterised by a topological invariant called the winding number, $\nu_{1\mathrm{D}}$. When the winding number is non-zero the system supports zero energy Majorana fermion states, exponentially localised at its boundary. Alternatively, a non-trivial topological number can imply a capacity for supporting non-trivial quasi-particle excitations. The Kitaev honeycomb lattice model [10] supports localised Majorana fermions in vortex excitations while its Chern number is non-zero.

In an ideal world, there would exist observable operators for any quantity we would like to measure. Sadly this is not always the case, and the Chern number is not an exception. In some systems there exist secondary measures of topological order which are experimentally accessible, e.g. the quantum Hall effect, thermal Hall effect [37, 38, 39], zero-frequency conductivity [40], ground state degeneracy [41], topological entanglement entropy [42, 7], the existence of edge states, and the entanglement spectrum [43]. These indicators can be strong evidence of

topological order, however the ability to measure the relevant invariant directly provides the most complete characterisation of the topological nature of the system.

In the absence of defects, a Chern number can be defined for models in any symmetry class as long as the number of spatial dimensions is even [17, 18, 20]. On the other hand, winding numbers can be defined in any spatial dimension, the only restriction being that the Hamiltonian must respect CH symmetry. In systems that obey both of these constraints in addition to supporting a sufficiently small number of distinct species of fermion, the winding number and various representations of the Chern number can be identified. Furthermore, the winding number in these cases can be written in terms of quantities which are themselves written in terms of observable quantities. Therefore, if a means can be found to access these observables in an experiment, the Chern number can be measured.

The problem with this approach is the constraint on the number of species of fermion the system may support. For insulating systems we are restricted to two species, while for superconducting systems the we are allowed only one. Many proposed models require more and are therefore exempt from this method. The purpose of this work is to extend the method to allow for twice as many species in each case. We shall see that through decomposing the Berry phase representation of the Chern number into contributions from some subspaces defined *a priori*, we can write it as a sum of winding numbers associated with each subspace. These subsystem winding numbers are experimentally accessible and, therefore, we retrieve the overall Chern number.

In the subsequent sections we will present an analytical argument and numerical evidence for this new method. In Sec. 2.1 we review the known definitions and conventions associated with the Chern number and winding number of systems in two spatial dimensions. In Sec. 2.2 we derive the analytical argument for decomposing the Chern number as subsystem winding numbers. In Sec. 2.3 we present two numerical examples that verify the result within pre-specified limits. Finally, in Sec. 2.4 we discuss the implementation of the method in systems of cold atoms.

2.1 Chern number and winding numbers in two spatial dimensions

The following analysis stands in both the superconducting and insulating cases, despite the derivation being slightly different. Where necessary, we present here the definitions and derivations in the context of insulating systems, and the superconducting case will be addressed separately. Translationally invariant lattice models in two spatial dimensions supporting $N = 2$ species of fermion, $\hat{a}_{\boldsymbol{p}}$ and $\hat{b}_{\boldsymbol{p}}$, can be written in the form

$$H = \int_{\mathrm{BZ}} d^2p \; \boldsymbol{\psi}^\dagger_{\boldsymbol{p}} h(\boldsymbol{\lambda}, \boldsymbol{p}) \boldsymbol{\psi}_{\boldsymbol{p}}, \tag{2.1}$$

where $\boldsymbol{\psi}_{\boldsymbol{p}} = \begin{pmatrix} \hat{a}_{\boldsymbol{p}} & \hat{b}_{\boldsymbol{p}} \end{pmatrix}^{\mathrm{T}}$ and $\boldsymbol{p} = \begin{pmatrix} p_x, & p_y \end{pmatrix} \in \mathrm{BZ}$ where BZ is the Brillouin zone. The kernel Hamiltonian $h(\boldsymbol{\lambda}, \boldsymbol{p})$ is an 2×2 Hermitian matrix where $\boldsymbol{\lambda} = \begin{pmatrix} \lambda_1, & \ldots, & \lambda_M \end{pmatrix} \in \mathcal{M}^M$ such that $\mathcal{M}^M$ is in general an M-dimensional complex manifold we call *parameter space*. For the subsequent derivations we drop the explicit $\boldsymbol{\lambda}$ dependence. The ground state of the system is given by

$$|\Psi\rangle = \prod_{\boldsymbol{p}} |\psi_{\boldsymbol{p}}\rangle \,, \tag{2.2}$$

which is defined in terms of the operators $\hat{a}^\dagger_{\boldsymbol{p}}$ and $\hat{b}^\dagger_{\boldsymbol{p}}$ acting on the fermionic vacuum $|00\rangle$.

$$|\psi_{\boldsymbol{p}}\rangle = \sum_{n^a_{\boldsymbol{p}},n^b_{\boldsymbol{p}}=0,1} \alpha_{n^a_{\boldsymbol{p}},n^b_{\boldsymbol{p}}} \left(\hat{a}^\dagger_{\boldsymbol{p}}\right)^{n^a_{\boldsymbol{p}}} \left(\hat{b}^\dagger_{\boldsymbol{p}}\right)^{n^b_{\boldsymbol{p}}} |00\rangle \,. \tag{2.3}$$

The kernel Hamiltonian has a pair of eigenvectors and eigenvalues

$$h(\boldsymbol{p})\,|\psi_\pm(\boldsymbol{p})\rangle = E_\pm(\boldsymbol{p})\,|\psi_\pm(\boldsymbol{p})\rangle\,, \quad E_-(\boldsymbol{p}) \leq 0 \text{ and } E_+(\boldsymbol{p}) \geq 0. \tag{2.4}$$

We require that the system has an energy gap $\Delta E = \min_{\boldsymbol{p}}\left[E_+(\boldsymbol{p})\right] - \max_{\boldsymbol{p}}\left[E_-(\boldsymbol{p})\right] \neq 0$. We take the system to be at *half filling* by which we mean we construct the ground state of the system by filling it up with particles starting with the most negative energy states until the number of particles in the system is half the maximum number available. Because of the condition on the eigenvalues (2.4), this implies the ground state for $h(\boldsymbol{p})$ is $|\psi_-(\boldsymbol{p})\rangle$. The Chern number, $\nu_{2\mathrm{D}} \in \mathbb{Z}$, that characterises the topological phase of the system is defined as

$$\nu_{2\mathrm{D}} = -\frac{i}{2\pi}\int_{\mathrm{BZ}} d^2p \;\; \mathrm{tr}\left(P_{\boldsymbol{p}}\left[\partial_{p_x}P_{\boldsymbol{p}}, \partial_{p_y}P_{\boldsymbol{p}}\right]\right) \tag{2.5}$$

where $P_{\boldsymbol{p}} = |\psi_-(\boldsymbol{p})\rangle\langle\psi_-(\boldsymbol{p})|$ is the projector on the ground state of $h(\boldsymbol{p})$. This is not the only way we can write the Chern number.

2.1.1 The Berry phase representation of $\nu_{2\mathbf{D}}$

The Chern number can also be written in terms of the Berry phase accrued around the boundary of the BZ. To see this we take the projector definition of the Chern number (2.5) and substitute in the definition of the projector $P_{\boldsymbol{p}}$

$$\begin{aligned}\nu_{2\mathrm{D}} = -\frac{i}{2\pi}\int_{\mathrm{BZ}} d^2p \;\; &\langle\psi_-(\boldsymbol{p})|\Big[\,|\partial_{p_x}\psi_-(\boldsymbol{p})\rangle\langle\psi_-(\boldsymbol{p})| \\ &+ |\psi_-(\boldsymbol{p})\rangle\langle\partial_{p_x}\psi_-(\boldsymbol{p})|\,, |\partial_{p_y}\psi_-(\boldsymbol{p})\rangle\langle\psi_-(\boldsymbol{p})| \\ &+ |\psi_-(\boldsymbol{p})\rangle\langle\partial_{p_x}\psi_-(\boldsymbol{p})|\Big]\,|\psi_-(\boldsymbol{p})\rangle\,.\end{aligned} \tag{2.6}$$

$|\psi_-(\boldsymbol{p})\rangle$ is normalised and therefore $\partial_\mu \langle\psi_-(\boldsymbol{p})|\psi_-(\boldsymbol{p})\rangle = 0$, with $\mu = p_x, p_y$, such that

$$\langle\partial_\mu\psi_-(\boldsymbol{p})|\psi_-(\boldsymbol{p})\rangle = -\langle\psi_-(\boldsymbol{p})|\partial_\mu\psi_-(\boldsymbol{p})\rangle\,. \tag{2.7}$$

By expanding (2.6) and applying (2.7) we have

$$\nu_{\text{2D}} = -\frac{i}{2\pi}\int_{\text{BZ}} d^2p\ \ \varepsilon_{\mu\nu}\,\langle\partial_{p_\mu}\psi_-(\boldsymbol{p})|\partial_{p_\nu}\psi_-(\boldsymbol{p})\rangle\,. \tag{2.8}$$

We recognise that the integrand of (2.8) is the Berry curvature $F(\boldsymbol{p})$

$$F(\boldsymbol{p}) = \varepsilon_{\mu\nu}\partial_\mu A_\nu = \varepsilon_{\mu\nu}\,\langle\partial_{p_\mu}\psi_-(\boldsymbol{p})|\partial_{p_\nu}\psi_-(\boldsymbol{p})\rangle\,, \tag{2.9}$$

where $\boldsymbol{A} = \langle\psi^-(\boldsymbol{p})|\boldsymbol{\partial}|\psi^-(\boldsymbol{p})\rangle$ with $\boldsymbol{\partial} = \left(\partial_{p_x},\ \ \partial_{p_y}\right)$. Using Stokes' theorem we can write the Chern number as

$$\nu_{\text{2D}} = -\frac{i}{2\pi}\int_{\text{BZ}} d^2p\ \ F(\boldsymbol{p}) = -\frac{i}{2\pi}\oint_{\partial\text{BZ}} d\boldsymbol{p}\cdot\boldsymbol{A}, \tag{2.10}$$

where ∂BZ is the boundary of the Brillouin zone.

2.1.2 The winding number representation of ν_{2D}

Under the constraint that $\dim[h(\boldsymbol{p})] = 2$ it can be parametrised in terms of a normalised vector $\hat{\boldsymbol{s}}(\boldsymbol{p}) : \text{BZ} \to S^2$

$$h(\boldsymbol{p}) = |\hat{\boldsymbol{s}}(\boldsymbol{p})|\hat{\boldsymbol{s}}(\boldsymbol{p})\cdot\boldsymbol{\sigma}, \tag{2.11}$$

where $\boldsymbol{\sigma} = \left(\sigma^x,\ \ \sigma^y,\ \ \sigma^z\right)$. We can express ν_{2D} as the winding of $\hat{\boldsymbol{s}}(\boldsymbol{p})$ over BZ. Using (2.11) we can write the projector $P_{\boldsymbol{p}}$ as

$$P_{\boldsymbol{p}} = \frac{1}{2}\left(\mathbb{I} - \hat{\boldsymbol{s}}(\boldsymbol{p})\cdot\boldsymbol{\sigma}\right), \tag{2.12}$$

where $\mathbb{I}$ is the identity matrix. By substituting (2.12) into (2.5) and employing the identities

$$(\boldsymbol{a}\cdot\boldsymbol{\sigma})\,(\boldsymbol{b}\cdot\boldsymbol{\sigma}) = \mathbb{I}\boldsymbol{a}\cdot\boldsymbol{b} + i\boldsymbol{\sigma}\cdot\boldsymbol{a}\times\boldsymbol{b} \tag{2.13}$$

for two 3-vectors $\boldsymbol{a}$ and $\boldsymbol{b}$, and

$$\mathrm{tr}\left(\sigma^\alpha \sigma^\beta\right) = 2\delta_{\alpha\beta}; \qquad \alpha, \beta = x, y, z, \tag{2.14}$$

we have

$$\begin{aligned}\nu_{\mathrm{2D}} =& -\frac{i}{2\pi}\int_{\mathrm{BZ}} d^2p \ \mathrm{tr}\left(|\psi_-(\boldsymbol{p})\rangle \langle\psi_-(\boldsymbol{p})| \frac{1}{4}\left[\partial_{p_x}\hat{\boldsymbol{s}}(\boldsymbol{p})\cdot\boldsymbol{\sigma}, \partial_{p_y}\hat{\boldsymbol{s}}(\boldsymbol{p})\cdot\boldsymbol{\sigma}\right]\right) \\ =& \frac{1}{4\pi}\int_{\mathrm{BZ}} d^2p \ \ \hat{\boldsymbol{s}}(\boldsymbol{p})\cdot\left(\partial_{p_x}\hat{\boldsymbol{s}}(\boldsymbol{p})\times\partial_{p_x}\hat{\boldsymbol{s}}(\boldsymbol{p})\right) \\ \equiv& \tilde{\nu}_{\mathrm{2D}}\end{aligned} \tag{2.15}$$

As the BZ is spanned, $\hat{\boldsymbol{s}}(\boldsymbol{p})$ winds around the sphere S^2 an integer number of times. If $\nu_{\mathrm{2D}} \neq 0$ we say that the system is in a topological phase.

2.1.3 Observability of the winding number

The winding number is of particular interest as it is directly observable. It is easy to show that

$$\hat{\boldsymbol{s}}(\boldsymbol{p}) = \langle\psi_-(\boldsymbol{p})|\boldsymbol{\sigma}|\psi_-(\boldsymbol{p})\rangle = \langle\psi_{\boldsymbol{p}}|\boldsymbol{\Sigma}|\psi_{\boldsymbol{p}}\rangle \tag{2.16}$$

where $\boldsymbol{\Sigma} = \boldsymbol{\psi}^\dagger_{\boldsymbol{p}}\boldsymbol{\sigma}\boldsymbol{\psi}_{\boldsymbol{p}}$ are the second quantised representations of the Pauli operators explicitly given by

$$\begin{aligned}\Sigma^x =& \hat{a}^\dagger_{\boldsymbol{p}}\hat{b}_{\boldsymbol{p}} + \hat{b}^\dagger_{\boldsymbol{p}}\hat{a}_{\boldsymbol{p}}, \\ \Sigma^y =& -i\hat{a}^\dagger_{\boldsymbol{p}}\hat{b}_{\boldsymbol{p}} + i\hat{b}^\dagger_{\boldsymbol{p}}\hat{a}_{\boldsymbol{p}}, \\ \Sigma^z =& \hat{a}^\dagger_{\boldsymbol{p}}\hat{a}_{\boldsymbol{p}} - \hat{b}^\dagger_{\boldsymbol{p}}\hat{b}_{\boldsymbol{p}}\end{aligned} \tag{2.17}$$

In systems of cold atom systems, by studying how the cloud of atoms expands when the trap is switched off, one can obtain a set of time of flight images from which one can extract the expectation values of the number operators $\hat{a}^\dagger_{\boldsymbol{p}}\hat{a}_{\boldsymbol{p}}$ and $\hat{b}^\dagger_{\boldsymbol{p}}\hat{b}_{\boldsymbol{p}}$. As such the σ^z component of (2.16) can be measured and the $\sigma^{x,y}$ components can be obtained through suitable rotations.

2.1.4 Breakdown of the winding number representation

If the number of species of fermion in the system $N > 2$ then $h(\boldsymbol{p})$ can no longer be expanded in the Pauli basis. We can choose to expand it in terms of some higher dimensional basis of matrices, then however $\dim[\hat{\boldsymbol{s}}(\boldsymbol{p})] > 3$ and the derivation of the winding number in sec. 2.1.2 is no longer sound. While it would, in principle, be possible to construct the components of some higher dimensional $\hat{\boldsymbol{s}}(\boldsymbol{p})$ from time of flight images, we no longer know how to reconstruct the Chern number from them.

2.2 Decomposition of the Chern number into subsystem winding numbers

We now present the analytic argument for decomposing the Chern number as a sum of winding numbers associated with each subsystem. We present first present the argument for topological insulators that preserve particle number and then show that it also holds for parity conserving topological superconductors.

2.2.1 Derivation for topological insulators

Consider a system with four different species of fermion $\hat{a}_1$, $\hat{a}_2$, $\hat{b}_1$, and $\hat{b}_2$ where the a/b bi-partition can correspond to a number of different physical distinctions (e.g. spin degrees of freedom, atomic levels, different sectors of some discrete symmetry). Assuming translational invariance and periodic boundary conditions we can write the Hamiltonian as (2.1) with $\boldsymbol{\psi}_{\boldsymbol{p}} = \begin{pmatrix} \hat{a}_{1,\boldsymbol{p}} & \hat{a}_{2,\boldsymbol{p}} & \hat{b}_{1,\boldsymbol{p}} & \hat{b}_{2,\boldsymbol{p}} \end{pmatrix}^{\mathrm{T}}$. A general state in the Hilbert space of the system can be written as

$$|\Psi\rangle = \prod_{\boldsymbol{p}} \left(\sum_{n^i_{j,\boldsymbol{p}}=0,1} \alpha_{n^a_{1,\boldsymbol{p}},n^a_{2,\boldsymbol{p}},n^b_{1,\boldsymbol{p}},n^b_{2,\boldsymbol{p}}} |n^a_{1,\boldsymbol{p}}, n^a_{2,\boldsymbol{p}}, n^b_{1,\boldsymbol{p}}, n^b_{2,\boldsymbol{p}}\rangle \right), \tag{2.18}$$

where we have expressed the state in the occupational basis

$$|n^a_{1,\boldsymbol{p}}, n^a_{2,\boldsymbol{p}}, n^b_{1,\boldsymbol{p}}, n^b_{2,\boldsymbol{p}}\rangle = \left(\hat{a}^\dagger_{1,\boldsymbol{p}}\right)^{n^a_{1,\boldsymbol{p}}} \left(\hat{a}^\dagger_{2,\boldsymbol{p}}\right)^{n^a_{2,\boldsymbol{p}}} \left(\hat{b}^\dagger_{1,\boldsymbol{p}}\right)^{n^b_{1,\boldsymbol{p}}} \left(\hat{b}^\dagger_{2,\boldsymbol{p}}\right)^{n^b_{1,\boldsymbol{p}}} |0000\rangle\,. \quad (2.19)$$

Here $\{n^i_{j,\boldsymbol{p}}\} = 0, 1$ are the fermionic occupation numbers and $|0000\rangle$ is the fermionic vacuum. The eigenstates of (2.1) will be of the form (2.18) with the further condition of normalisation, i.e. $\sum_{n^j_{i,\boldsymbol{p}}=0,1} \left|\alpha_{n^a_{1,\boldsymbol{p}},n^a_{2,\boldsymbol{p}},n^b_{1,\boldsymbol{p}},n^b_{2,\boldsymbol{p}}}\right|^2 = 1$.

As stated previously, we restrict the system to a fixed particle number, i.e. $[H, N] = 0$ where $N = \sum_{\boldsymbol{p},\alpha=1,2} \left(\hat{a}^\dagger_{\alpha,\boldsymbol{p}}\hat{a}_{\alpha,\boldsymbol{p}} + \hat{b}^\dagger_{\alpha,\boldsymbol{p}}\hat{b}_{\alpha,\boldsymbol{p}}\right)$. Furthermore, we fix the system to be at half filling, which means that the ground state $|\psi_{\boldsymbol{p}}\rangle$ satisfies the condition $\sum_{i,j} n^i_{j,\boldsymbol{p}} = 2$. This restriction means that a complete local basis for each momentum component of the ground state is given by

$$\{|1100\rangle, |1010\rangle, |1001\rangle, |0110\rangle, |0101\rangle, |0011\rangle\}\,. \quad (2.20)$$

Now we can divide the ground state into two orthogonal subspaces

$$\begin{aligned} |\psi_{\boldsymbol{p}}\rangle =& A\,|n^a_{1,\boldsymbol{p}} + n^a_{2,\boldsymbol{p}} \Leftrightarrow \textbf{even}; n^b_{1,\boldsymbol{p}} + n^b_{2,\boldsymbol{p}} \Leftrightarrow \textbf{even}\rangle \\ &+ B\,|n^a_{1,\boldsymbol{p}} + n^a_{2,\boldsymbol{p}} \Leftrightarrow \textbf{odd}; n^b_{1,\boldsymbol{p}} + n^b_{2,\boldsymbol{p}} \Leftrightarrow \textbf{odd}\rangle \\ \equiv& A\,|e;e\rangle + B\,|o;o\rangle\,, \end{aligned} \quad (2.21)$$

where $\sum_j n^i_{j,\boldsymbol{p}}$ are either both even or both odd and $|A|^2 + |B|^2 = 1$. The next step is to perform a Schmidt decomposition on each part of the state, $|e;e\rangle$ and $|o;o\rangle$, which can be written

$$\begin{aligned} |e;e\rangle =& \cos\theta_e\,|a_e\rangle \otimes |b_e\rangle + \sin\theta_e\,|\tilde{a}_e\rangle \otimes |\tilde{b}_e\rangle\,, \\ |o;o\rangle =& \cos\theta_o\,|a_o\rangle \otimes |b_o\rangle + \sin\theta_o\,|\tilde{a}_o\rangle \otimes |\tilde{b}_o\rangle\,, \end{aligned} \quad (2.22)$$

where $\theta_e, \theta_o \in [0, \pi/2)$ ensuring that the Schmidt coefficients are non-negative. We stipulate that the states $|a_{e/o}\rangle\,|b_{e/o}\rangle$ are written in the same basis as (2.19).

The states in (2.22) obey the orthogonality conditions $\langle a_{e/o}|\tilde{a}_{e/o}\rangle = 0$ and $\langle b_{e/o}|\tilde{b}_{e/o}\rangle = 0$. More explicitly we have

$$\begin{aligned} |a_o\rangle &= \left(\alpha_{01}\hat{a}^\dagger_{2,\boldsymbol{p}} + \alpha_{10}\hat{a}^\dagger_{1,\boldsymbol{p}}\right)|00\rangle\,, & |\tilde{a}_o\rangle &= \left(\alpha^*_{10}\hat{a}^\dagger_{2,\boldsymbol{p}} - \alpha^*_{01}\hat{a}^\dagger_{1,\boldsymbol{p}}\right)|00\rangle\,, \\ |b_o\rangle &= \left(\beta_{01}\hat{b}^\dagger_{2,\boldsymbol{p}} + \beta_{10}\hat{b}^\dagger_{1,\boldsymbol{p}}\right)|00\rangle\,, & |\tilde{b}_o\rangle &= \left(\beta^*_{10}\hat{b}^\dagger_{2,\boldsymbol{p}} - \beta^*_{01}\hat{b}^\dagger_{1,\boldsymbol{p}}\right)|00\rangle \end{aligned} \tag{2.23}$$

and

$$\begin{aligned} |a_e\rangle &= e^{i\phi_a}|00\rangle\,, & |\tilde{a}_e\rangle &= e^{i\tilde{\phi}_a}\hat{a}^\dagger_{1,\boldsymbol{p}}\hat{a}^\dagger_{2,\boldsymbol{p}}|00\rangle\,, \\ |b_e\rangle &= e^{i\phi_b}\hat{b}^\dagger_{1,\boldsymbol{p}}\hat{b}^\dagger_{2,\boldsymbol{p}}|00\rangle\,, & |\tilde{b}_e\rangle &= e^{i\tilde{\phi}_b}|00\rangle\,, \end{aligned} \tag{2.24}$$

where $|\alpha_{01}|^2 + |\alpha_{10}|^2 = |\beta_{01}|^2 + |\beta_{10}|^2 = 1$. The phases $\phi_{a/b}$ and $\tilde{\phi}_{a/b}$ are in general non-zero however, after multiplying $|\psi_{\boldsymbol{p}}\rangle$ by a global phase of $e^{-i(\phi_a+\phi_b)}$, we can transfer them to the $|o;o\rangle$ subspace via a $U(1)$ local gauge transformation given by

$$\hat{a}^\dagger_{1,\boldsymbol{p}} \to e^{-i(\tilde{\phi}_a+\tilde{\phi}_b-\phi_a-\phi_b)}\hat{a}^\dagger_{1,\boldsymbol{p}}. \tag{2.25}$$

After this transformation the only momentum dependence in the $|e;e\rangle$ subspace is in the real and positive Schmidt coefficients $\cos\theta_e$ and $\sin\theta_e$. Having prepared the state we can now write $\nu_{2\mathrm{D}}$

$$\nu_{2\mathrm{D}} = -\frac{i}{2\pi}\oint_{\partial BZ} A^2\,\langle e;e|\boldsymbol{\partial}|e;e\rangle\cdot d\boldsymbol{p} - \frac{i}{2\pi}\oint_{\partial BZ} B^2\,\langle o;o|\boldsymbol{\partial}|o;o\rangle\cdot d\boldsymbol{p} \tag{2.26}$$

where terms containing $A\boldsymbol{\partial}A$ or $B\boldsymbol{\partial}B$ do not contribute because $A\boldsymbol{\partial}A + B\boldsymbol{\partial}B = \boldsymbol{\partial}(A^2+B^2)/2 = 0$ which follows from the reality condition on A and B. Direct evaluation of the integrand in the $|e;e\rangle$ case finds it to be zero because $\cos\theta_e\boldsymbol{\partial}\cos\theta_e + \sin\theta_e\boldsymbol{\partial}\sin\theta_e = \boldsymbol{\partial}(\cos^2\theta_e + \sin^2\theta_e)/2 = 0$. Noting that $\langle i_o|\boldsymbol{\partial}|i_o\rangle = -\langle\tilde{i}_o|\boldsymbol{\partial}|\tilde{i}_o\rangle$ and using the positivity and normalisation of the Schmidt coefficients, a direct evaluation gives

$$\nu_{2\mathrm{D}} = -\frac{i}{2\pi}\sum_{i=a,b}\oint_{\partial BZ} S\,\langle i_o|\boldsymbol{\partial}|i_o\rangle\cdot d\boldsymbol{p}, \quad S = |B|^2T, \tag{2.27}$$

where $T = \cos^2\theta_o - \sin^2\theta_o$ is a measure of the entanglement between the a and b subsystems.

The Chern number is now written as a sum of exclusive contributions from each subsystem. If $S = 1$ then (2.27) is simply a sum of Berry phases associated with each subsystem which can, by (2.15), be written as a sum of winding numbers of a pair of vectors $\hat{\boldsymbol{s}}_a(\boldsymbol{p})$ and $\hat{\boldsymbol{s}}_b(\boldsymbol{p})$. However as we shall see that the decomposition only fails when $S \to 0$, when the subsystems are maximally entangled. In section 2.3 we present examples that show that the method only diverges from the theoretical values when $T \to 0$.

2.2.2 Subsystem winding numbers as physical observables

We will now construct the subsystem winding numbers as a function of two vectors $\hat{\boldsymbol{s}}_a(\boldsymbol{p})$ and $\hat{\boldsymbol{s}}_b(\boldsymbol{p})$, which are themselves given in terms of the expectation values of the ground state, $|\psi_{\boldsymbol{p}}\rangle$, with some set of observable operators associated with each subsystem. In analogy with (2.17) we can construct the observables associated with the a and b subsystems, $\boldsymbol{\Sigma}_a = \left(\Sigma_a^x,\ \Sigma_a^y,\ \Sigma_a^z\right)$ and $\boldsymbol{\Sigma}_b = \left(\Sigma_b^x,\ \Sigma_b^y,\ \Sigma_b^z\right)$, and they are given explicitly by

$$\begin{aligned}
\Sigma_a^x &= \hat{a}^\dagger_{1,\boldsymbol{p}}\hat{a}_{2,\boldsymbol{p}} + \hat{a}^\dagger_{2,\boldsymbol{p}}\hat{a}_{1,\boldsymbol{p}} & \Sigma_b^x &= \hat{b}^\dagger_{1,\boldsymbol{p}}\hat{b}_{2,\boldsymbol{p}} + \hat{b}^\dagger_{2,\boldsymbol{p}}\hat{b}_{1,\boldsymbol{p}} \\
\Sigma_a^y &= -i\hat{a}^\dagger_{1,\boldsymbol{p}}\hat{a}_{2,\boldsymbol{p}} + i\hat{a}^\dagger_{2,\boldsymbol{p}}\hat{a}_{1,\boldsymbol{p}} & \Sigma_b^y &= -i\hat{b}^\dagger_{1,\boldsymbol{p}}\hat{b}_{2,\boldsymbol{p}} + i\hat{b}^\dagger_{2,\boldsymbol{p}}\hat{b}_{1,\boldsymbol{p}} \\
\Sigma_a^z &= \hat{a}^\dagger_{1,\boldsymbol{p}}\hat{a}_{1,\boldsymbol{p}} - \hat{a}^\dagger_{2,\boldsymbol{p}}\hat{a}_{2,\boldsymbol{p}} & \Sigma_b^z &= \hat{b}^\dagger_{1,\boldsymbol{p}}\hat{b}_{1,\boldsymbol{p}} - \hat{b}^\dagger_{2,\boldsymbol{p}}\hat{b}_{2,\boldsymbol{p}}
\end{aligned} \tag{2.28}$$

Now we can calculate the expectation values

$$\langle\psi_{\boldsymbol{p}}|\boldsymbol{\Sigma}_i|\psi_{\boldsymbol{p}}\rangle = |A|^2\langle e;e|\boldsymbol{\Sigma}_i|e;e\rangle + |B|^2\langle o;o|\boldsymbol{\Sigma}_i|o;o\rangle \tag{2.29}$$

where cross terms between the even and odd subspaces do not appear since the operators given in (2.28) conserve particle number. By direct evaluation of the

$|e;e\rangle$ term we see that it vanishes. Evaluation of the $|o;o\rangle$ term gives

$$\langle o;o|\boldsymbol{\Sigma}_i|o;o\rangle = \cos^2\theta_o \langle i_o|\boldsymbol{\Sigma}_i|i_o\rangle + \sin^2\theta_o \langle \tilde{i}_o|\boldsymbol{\Sigma}_i|\tilde{i}_o\rangle = T\langle i_o|\boldsymbol{\Sigma}_i|i_o\rangle \tag{2.30}$$

where we have used the tracelessness of the $\boldsymbol{\Sigma}_i$ operators which implies $\langle \tilde{i}_o|\boldsymbol{\Sigma}_i|\tilde{i}_o\rangle = -\langle i_o|\boldsymbol{\Sigma}_i|i_o\rangle$. Each case is explicitly given by

$$\begin{aligned}\langle \psi_{\boldsymbol{p}}|\boldsymbol{\Sigma}_a|\psi_{\boldsymbol{p}}\rangle &= S\langle \psi_a(\boldsymbol{p})|\boldsymbol{\sigma}|\psi_a(\boldsymbol{p})\rangle \\ \langle \psi_{\boldsymbol{p}}|\boldsymbol{\Sigma}_b|\psi_{\boldsymbol{p}}\rangle &= S\langle \psi_b(\boldsymbol{p})|\boldsymbol{\sigma}|\psi_b(\boldsymbol{p})\rangle\,,\end{aligned} \tag{2.31}$$

where $|\psi_a(\boldsymbol{p})\rangle = \begin{pmatrix}\alpha_{01} & \alpha_{10}\end{pmatrix}^{\mathrm{T}}$ and $|\psi_b(\boldsymbol{p})\rangle = \begin{pmatrix}\beta_{01} & \beta_{10}\end{pmatrix}^{\mathrm{T}}$. We can normalise the vectors given in (2.31) and relabel them as

$$\hat{\boldsymbol{s}}_i(\boldsymbol{p}) = \frac{\boldsymbol{s}_i(\boldsymbol{p})}{|\boldsymbol{s}_i(\boldsymbol{p})|} = \langle \psi_i(\boldsymbol{p})|\boldsymbol{\sigma}|\psi_i(\boldsymbol{p})\rangle\,, \tag{2.32}$$

where $|\boldsymbol{s}_i(\boldsymbol{p})| = |B|^2|T|^2$. In much the same way as presented in 2.1 we can define subsystem Chern numbers for the $|i_o\rangle$ states as Berry phases

$$\nu^i_{2\mathrm{D}} = -\frac{i}{2\pi}\oint_{\partial\mathrm{BZ}} \langle i_o|\boldsymbol{\partial}|i_o\rangle\cdot d\boldsymbol{p} \tag{2.33}$$

or as subsystem winding numbers

$$\nu^i_{2\mathrm{D}} = \frac{1}{4\pi}\int_{\mathrm{BZ}} d^2p\ \ \hat{\boldsymbol{s}}_i(\boldsymbol{p})\cdot\left(\partial_{p_x}\hat{\boldsymbol{s}}_i(\boldsymbol{p})\times\partial_{p_y}\hat{\boldsymbol{s}}_i(\boldsymbol{p})\right) \tag{2.34}$$

We can view $|\psi_i(\boldsymbol{p})\rangle$ as the ground state of some fictitious kernel Hamiltonian $h_i(\boldsymbol{p}) = \hat{\boldsymbol{s}}_i(\boldsymbol{p})\cdot\boldsymbol{\sigma}$. We have shown that each subsystem Berry phase (2.33) is proportional to its corresponding subsystem winding number (2.34) and that the winding numbers are physically observable. We now show that, with slight modifications, the above method applies to topological superconductors that conserve particle parity.

2.2.3 Derivation for topological superconductors

Again we take the Hamiltonian of the system to be (2.1), but now the spinor takes the form $\boldsymbol{\psi}_{\boldsymbol{p}} = \begin{pmatrix} \hat{a}_{\boldsymbol{p}} & \hat{a}^\dagger_{-\boldsymbol{p}} & \hat{b}_{\boldsymbol{p}} & \hat{b}^\dagger_{-\boldsymbol{p}} \end{pmatrix}^{\mathrm{T}}$. A general state in the Hilbert space can be written as in (2.18) but with the Fock space ordered as

$$|n^a_{\boldsymbol{p}}, n^a_{-\boldsymbol{p}}, n^b_{\boldsymbol{p}}, n^b_{-\boldsymbol{p}}\rangle = \left(\hat{a}^\dagger_{\boldsymbol{p}}\right)^{n^a_{\boldsymbol{p}}} \left(\hat{a}^\dagger_{-\boldsymbol{p}}\right))^{n^a_{-\boldsymbol{p}}} \left(\hat{b}^\dagger_{\boldsymbol{p}}\right)^{n^b_{\boldsymbol{p}}} \left((\hat{b}^\dagger_{-\boldsymbol{p}}\right)^{n^b_{-\boldsymbol{p}}} |0000\rangle \tag{2.35}$$

Superconductors only preserve total parity, i.e. $[H, P] = 0$ with

$$P = \exp\left(i\pi \sum_{\boldsymbol{p}} \left(\hat{a}^\dagger_{\boldsymbol{p}} \hat{a}_{\boldsymbol{p}} + \hat{b}^\dagger_{\boldsymbol{p}} \hat{b}_{\boldsymbol{p}}\right)\right) = P_a P_b \tag{2.36}$$

while subsystem parities, P_a and P_b, are not independently conserved. Without loss of generality we assume that the ground state is in the total even parity sector. This means that the subsystems are correlated such that $P_a = P_b$, which in turn means that the ground state complies with the condition of overall momentum. Under these conditions the ground state is given in the basis spanned by the states

$$\{|0000\rangle, |0011\rangle, |1100\rangle, |1111\rangle, |0110\rangle, |1001\rangle\}. \tag{2.37}$$

As in the insulating case we divide the ground state into even and odd subspaces

$$|\psi_{\boldsymbol{p}}\rangle = A\,|e;e\rangle + B\,|o;o\rangle\,. \tag{2.38}$$

Performing the Schmidt decomposition between the a and b subspaces in this parity sector we obtain a general expression which has the same form as (2.22) but with the Schmidt bases given by

$$\begin{aligned} |a_e\rangle &= \left(\alpha_{00} + \alpha_{11}\hat{a}^\dagger_{\boldsymbol{p}} a^\dagger_{-\boldsymbol{p}}\right)|00\rangle\,, & |\tilde{a}_e\rangle &= \left(\alpha^*_{11} - \alpha^*_{00}\hat{a}^\dagger_{\boldsymbol{p}}\hat{a}^\dagger_{-\boldsymbol{p}}\right)|00\rangle\,, \\ |b_e\rangle &= \left(\beta_{00} + \beta_{11}\hat{b}^\dagger_{\boldsymbol{p}} b^\dagger_{-\boldsymbol{p}}\right)|00\rangle\,, & |\tilde{b}_e\rangle &= \left(\beta^*_{11} - \beta^*_{00}\hat{b}^\dagger_{\boldsymbol{p}}\hat{b}^\dagger_{-\boldsymbol{p}}\right)|00\rangle\,, \end{aligned} \tag{2.39}$$

and

$$|a_o\rangle = e^{i\phi_a} a^\dagger_{-\boldsymbol{p}} |00\rangle\,, \qquad |\tilde{a}_o\rangle = e^{i\tilde{\phi}_a} \hat{a}^\dagger_{\boldsymbol{p}} |00\rangle\,,$$
$$|b_o\rangle = e^{i\phi_b} \hat{b}^\dagger_{\boldsymbol{p}} |00\rangle\,, \qquad |\tilde{b}_o\rangle = e^{i\tilde{\phi}_b} \hat{b}^\dagger_{-\boldsymbol{p}} |00\rangle\,. \tag{2.40}$$

In a similar way to the insulating case, all coefficients except those in the $|o;o\rangle$ subspace can be made real via $U(1)$ gauge transformations. With this in mind, the decomposition of the Berry phase proceeds in the same way as the insulating case with the only difference being that the contribution from the $|o;o\rangle$ subspace vanishes and we are left with

$$\nu_{\text{2D}} = -\frac{i}{2\pi} \sum_{i=a,b} \oint_{\partial BZ} S \, \langle i_o | \boldsymbol{\partial} | i_o \rangle \cdot d\boldsymbol{p}, \quad S = |A|^2 T. \tag{2.41}$$

The observable operators, $\boldsymbol{\Sigma}_i$, used to evaluate the subsystem winding numbers are now given by

$$\Sigma^x_a = \hat{a}^\dagger_{\boldsymbol{p}} \hat{a}^\dagger_{-\boldsymbol{p}} + \hat{a}_{-\boldsymbol{p}} \hat{a}_{\boldsymbol{p}}, \qquad \Sigma^x_b = \hat{b}^\dagger_{\boldsymbol{p}} \hat{b}^\dagger_{-\boldsymbol{p}} + \hat{b}_{-\boldsymbol{p}} \hat{b}_{\boldsymbol{p}},$$
$$\Sigma^y_a = -i\hat{a}^\dagger_{\boldsymbol{p}} \hat{a}^\dagger_{-\boldsymbol{p}} + i\hat{a}_{-\boldsymbol{p}} \hat{a}_{\boldsymbol{p}}, \qquad \Sigma^x_b = -i\hat{b}^\dagger_{\boldsymbol{p}} \hat{b}^\dagger_{-\boldsymbol{p}} + i\hat{b}_{-\boldsymbol{p}} \hat{b}_{\boldsymbol{p}},$$
$$\Sigma^z_a = \hat{a}^\dagger_{\boldsymbol{p}} \hat{a}_{\boldsymbol{p}} - \hat{a}^\dagger_{-\boldsymbol{p}} \hat{a}_{-\boldsymbol{p}}, \qquad \Sigma^z_b = \hat{b}^\dagger_{\boldsymbol{p}} \hat{b}_{\boldsymbol{p}} - \hat{b}^\dagger_{-\boldsymbol{p}} \hat{b}_{-\boldsymbol{p}}. \tag{2.42}$$

When we compute the expectation values we find that only the $|e;e\rangle$ subspace terms contribute. The expectation values are given by

$$\langle e;e|\boldsymbol{\Sigma}_a|e;e\rangle = \langle \psi_a(\boldsymbol{p})|\boldsymbol{\sigma}|\psi_a(\boldsymbol{p})\rangle$$
$$\langle e;e|\boldsymbol{\Sigma}_b|e;e\rangle = \langle \psi_b(\boldsymbol{p})|\boldsymbol{\sigma}|\psi_b(\boldsymbol{p})\rangle \tag{2.43}$$

where $|\psi_a(\boldsymbol{p})\rangle = \begin{pmatrix}\alpha_{00}, & \alpha_{11}\end{pmatrix}^{\text{T}}$ and $|\psi_b(\boldsymbol{p})\rangle = \begin{pmatrix}\beta_{00}, & \beta_{11}\end{pmatrix}^{\text{T}}$. Therefore, as in the insulating case, (2.43) can be used to evaluate the subsystem winding numbers (2.34). Under the condition of non-maximal entanglement we shall show that the Chern number becomes additive in these winding numbers. The entanglement

between the subsystems can be accessed experimentally by measuring the quantity $|\hat{\boldsymbol{s}}_i(\boldsymbol{p})|$ which is proportional to the entanglement. As such a given choice of bi-partition can be assessed for the applicability of this method.

2.3 Case studies

In this section we present two numerical case studies showcasing the method. The examples we use are the quantum spin Hall insulator [44] and a staggered topological superconductor [45]. We find that in both cases the phase diagrams are accurately reproduced, with any discrepancies occurring only when the entanglement between the subsystems is particularly high.

2.3.1 Example 1: The quantum spin Hall Insulator

The time-reversal invariant quantum spin Hall insulator is defined on a honeycomb lattice [44] and its tight binding Hamiltonian is given by

$$\begin{aligned}\hat{H}_{\mathrm{QSH}} =& t\sum_{\langle \boldsymbol{ij}\rangle} \hat{\boldsymbol{a}}_{\boldsymbol{i}}^{\dagger}\hat{\boldsymbol{b}}_{\boldsymbol{j}} + i\lambda_{\mathrm{SO}}\sum_{\langle\langle \boldsymbol{ij}\rangle\rangle} \xi_{\mathrm{SO}}\left(\hat{\boldsymbol{a}}_{\boldsymbol{i}}^{\dagger}\sigma^{z}\hat{\boldsymbol{a}}_{\boldsymbol{j}} + \hat{\boldsymbol{b}}_{\boldsymbol{i}}^{\dagger}\sigma^{z}\hat{\boldsymbol{b}}_{\boldsymbol{j}}\right) \\ &+ \lambda_{v}\sum_{\boldsymbol{i}}\left(\hat{\boldsymbol{a}}_{\boldsymbol{i}}^{\dagger}\hat{\boldsymbol{a}}_{\boldsymbol{i}} - \hat{\boldsymbol{b}}_{\boldsymbol{i}}^{\dagger}\hat{\boldsymbol{b}}_{\boldsymbol{i}}\right) + i\lambda_{\mathrm{R}}\sum_{\langle \boldsymbol{ij}\rangle}\hat{\boldsymbol{a}}_{\boldsymbol{i}}^{\dagger}\left(\boldsymbol{\sigma}\times\hat{\boldsymbol{d}}_{\boldsymbol{i}}\right)_{z}\hat{\boldsymbol{b}}_{\boldsymbol{j}}\end{aligned} \tag{2.44}$$

where the spinors $\hat{\boldsymbol{a}}_{\boldsymbol{i}} = \left(\hat{a}_{\boldsymbol{i},\uparrow},\ \ \hat{a}_{\boldsymbol{i},\downarrow}\right)^{\mathrm{T}}$ and $\hat{\boldsymbol{b}}_{\boldsymbol{i}} = \left(\hat{b}_{\boldsymbol{i},\uparrow},\ \ \hat{b}_{\boldsymbol{i},\downarrow}\right)^{\mathrm{T}}$ denote the two sublattice degrees of freedom of the lattice. The terms with coefficients t and λ_v are the spin-independent nearest-neighbor tunneling and the sublattice energy imbalance, respectively. The terms with coefficients λ_{R} and λ_{SO} are the nearest and next-nearest neighbor spin-orbit coupling, respectively. Finally we have $\xi_{\mathrm{SO}} = \mathrm{sgn}\left[\hat{\boldsymbol{d}}_1 \times \hat{\boldsymbol{d}}_2\right]$, where $\hat{\boldsymbol{d}}_1$ and $\hat{\boldsymbol{d}}_2$ are vectors that connect the next-nearest neighbor sites.

After Fourier transforming (2.44) we can write it in the form (2.1), where the

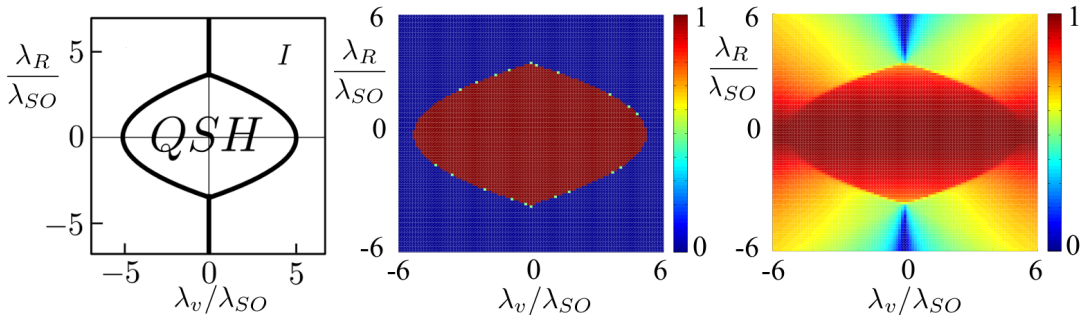

Figure 2.1: *Left*: Theoretical phase diagram in the parameter-space λ_R/λ_{SO}, λ_V/λ_{SO} of Hamiltonian (2.44). The trivial phase corresponds to $\nu^{\mathrm{s}}_{2\mathrm{D}} = 0$, while the QSH phase corresponds to $\nu_{2\mathrm{D}} = 1$. *Middle*: Numerical computation of the phase diagram as the winding spin Chern number $(\tilde{\nu}_\uparrow - \tilde{\nu}_\downarrow)/2$. *Right*: The minimum of the spin component entanglement measure across the Brillouin zone, $\min_{\boldsymbol{p}}|\hat{\boldsymbol{s}}_i(\boldsymbol{p})|$. When $\min_{\boldsymbol{p}}|\hat{\boldsymbol{s}}_i(\boldsymbol{p})|$ is small the entanglement is large. The spin components become maximally entangled (blue regions) only around the transitions between the two trivial insulators, while between trivial and spin Hall phases we find a discontinuity.

spinor is now given by $\boldsymbol{\psi}_{\boldsymbol{p}} = \left(\hat{a}_{\boldsymbol{p},\uparrow},\ \hat{a}_{\boldsymbol{p},\downarrow},\ \hat{b}_{\boldsymbol{p},\uparrow},\ \hat{b}_{\boldsymbol{p},\downarrow}\right)^{\mathrm{T}}$. Kane and Mele showed that this model supports two distinct phases, the quantum spin Hall phase and the trivial insulator phase, which are distinguished by a $\mathbb{Z}_2$ topological invariant [44]. In each phase the system has an energy gap; the gap closes as the system transitions between the two phases. Their $\mathbb{Z}_2$ invariant, analogous to the TKNN invariant [5], was shown by Sheng *et al.* [46] to be related to the spin Chern numbers, $\nu_{\uparrow/\downarrow}$, in the following way

$$\nu^{s}_{2\mathrm{D}} = \frac{\nu_\uparrow - \nu_\downarrow}{2} \tag{2.45}$$

where $\nu_\uparrow = -\nu_\downarrow$. The phase diagram of system is shown in fig. 2.1 *left*.

In line with our method, we can associate the spin up and spin down components in (2.44) with the $|a_{e/o}\rangle$ and $|b_{e/o}\rangle$ subspaces in the Schmidt decomposition,

as defined in the derivation in sec. 2.2.1. Therefore, the observable operators needed for computing the subsystem winding numbers are given by

$$\begin{aligned}\Sigma^x_{\uparrow/\downarrow} &= \hat{a}^\dagger_{\uparrow/\downarrow,\boldsymbol{p}}\hat{b}_{\uparrow/\downarrow,\boldsymbol{p}} + \hat{b}^\dagger_{\uparrow/\downarrow,\boldsymbol{p}}\hat{a}_{\uparrow/\downarrow,\boldsymbol{p}},\\ \Sigma^y_{\uparrow/\downarrow} &= -i\hat{a}^\dagger_{\uparrow/\downarrow,\boldsymbol{p}}\hat{b}_{\uparrow/\downarrow,\boldsymbol{p}} + i\hat{b}^\dagger_{\uparrow/\downarrow,\boldsymbol{p}}\hat{a}_{\uparrow/\downarrow,\boldsymbol{p}},\\ \Sigma^z_{\uparrow/\downarrow} &= \hat{a}^\dagger_{\uparrow/\downarrow,\boldsymbol{p}}\hat{a}_{\uparrow/\downarrow,\boldsymbol{p}} - \hat{b}^\dagger_{\uparrow/\downarrow,\boldsymbol{p}}\hat{b}_{\uparrow/\downarrow,\boldsymbol{p}}\end{aligned} \tag{2.46}$$

It is now possible to construct the two maps $\hat{\boldsymbol{s}}_\uparrow(\boldsymbol{p})$ and $\hat{\boldsymbol{s}}_\downarrow(\boldsymbol{p})$ and, by substituting them into (2.34), we can calculate the subsystem winding numbers, $\tilde{\nu}_\uparrow$ and $\tilde{\nu}_\downarrow$. After subtracting them as in (2.45) we find that the method perfectly reproduces the phase diagram of the model, as presented in fig. 2.1 *middle*. The subsystem entanglement is shown in fig. 2.1. We see that in the QSH phase the subsystems are minimally entangled. This lends evidence to the claim that the method works when the subsystems are non-maximally entangled.

2.3.2 Example 2: Topological superconductor with staggered sublattices

The second example we present is the topological superconductor with a staggered chemical potential [45]. The model supports a variety of topological phases with Chern numbers $\nu_{2\mathrm{D}} = 0, \pm 1, \pm 2$. The real space tight-binding Hamiltonian is given by

$$\begin{aligned}\hat{H} = \sum_{\boldsymbol{j}} \Big[&(\mu-\delta)\,\hat{a}^\dagger_{\boldsymbol{j}}\hat{a}_{\boldsymbol{j}} + (\mu+\delta)\,\hat{b}^\dagger_{\boldsymbol{j}}\hat{b}_{\boldsymbol{j}} + t\left(i\hat{a}^\dagger_{\boldsymbol{j}}\hat{b}_{\boldsymbol{j}} - i\hat{b}^\dagger_{\boldsymbol{j}}\hat{a}_{\boldsymbol{j}+\hat{\boldsymbol{x}}} + \hat{a}^\dagger_{\boldsymbol{j}}\hat{a}_{\boldsymbol{j}+\hat{\boldsymbol{y}}} + \hat{b}^\dagger_{\boldsymbol{j}}\hat{b}_{\boldsymbol{j}+\hat{\boldsymbol{y}}}\right)\\ &+ \Delta\left(\hat{a}^\dagger_{\boldsymbol{j}}\hat{b}^\dagger_{\boldsymbol{j}} + \hat{b}^\dagger_{\boldsymbol{j}}\hat{a}_{\boldsymbol{j}+\hat{\boldsymbol{x}}} + \hat{a}^\dagger_{\boldsymbol{j}}\hat{a}^\dagger_{\boldsymbol{j}+\hat{\boldsymbol{y}}} + \hat{b}^\dagger_{\boldsymbol{j}}\hat{b}_{\boldsymbol{j}+\hat{\boldsymbol{y}}}\right) + h.c.\Big],\end{aligned} \tag{2.47}$$

where $\hat{a}_{\boldsymbol{j}}$ and $\hat{b}_{\boldsymbol{j}}$ are the two sublattice fermions which are distinguished by the difference in the sign of the coefficient δ in the chemical potential. The coefficients t and Δ correspond to tunneling and pairing between adjacent lattice sites.

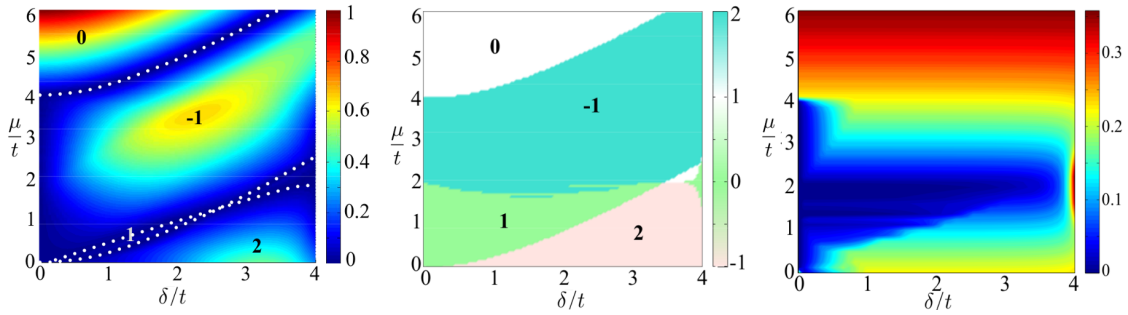

Figure 2.2: *Left*: The phase diagram as computed via the Berry phase. The colour encodes the magnitude of the spectral gap while the dashed lines indicate the phase boundaries. *Middle*: The phase diagram as a sum of the winding numbers of the a and b sublattices. *Right*: The sublattice entanglement as characterised by $\min_{\boldsymbol{p}}|\hat{\boldsymbol{s}}_i(\boldsymbol{p})|$. When $\min_{\boldsymbol{p}}|\hat{\boldsymbol{s}}_i(\boldsymbol{p})|$ is small the entanglement is large.

We partition the system by sublattice and therefore relevant observable operators are given by (2.42). Evaluation of (2.34), after calculating $\hat{\boldsymbol{s}}_a(\boldsymbol{p})$ and $\hat{\boldsymbol{s}}_b(\boldsymbol{p})$, leads to a reproduction of the phase diagram, as shown in fig. 2.2. The left pane shows the phase diagram as calculated using the Berry phase representation of the Chern number, while the middle pane shows the phase diagram as a sum of subsystem winding numbers. The two are largely in agreement, diverging only when the entanglement between the sublattices is maximal, as shown in fig. 2.2 *right*. It is also worth noting that the discrepancy is only in the sign of the Chern number, and as such all of the topological phases are distinguished.

2.4 Experimental implementation

In this section we describe how this method might be implemented in systems of cold atoms. Use of systems of cold atoms trapped in optical lattices to simulate different topological states of matter has come on leaps and bounds over the last decade. In particular, attempts have been made to measure various physical

observables including but not limited to time-of-flight measurements [47, 45, 48], analysis of wave packet dynamics [49], interferometric measurements of the Berry phase [50, 51], measurements of the Hall conductance [52, 53], measurements of the center of mass of atomic gases [54], and direct measurements of the Skyrmion number [55]. Many of these methods are defined for specific systems and are potentially unrealistic for actual experiments.

The specifics of how one might go about measuring the relevant observables for our method are analogous to [45]. We can take some specific tight binding model, such as that proposed in [45], and map it to a system of cold atoms trapped in an optical lattice. Couplings such as tunneling and chemical potentials can be modulated via Raman-assisted tunneling [56, 57, 58]. Furthermore, we can implement nearest neighbor pairing if we allow for two internal atomic states and s-wave Feshbach resonances [59, 60].

We must measure the components of the vectors $\hat{\boldsymbol{s}}_i(\boldsymbol{p})$, with $i = a, b$, in order to access the subsystem winding numbers. Time-of-flight images give direct access to the momentum space densities $\langle \hat{a}^\dagger_{\boldsymbol{p}} \hat{a}_{\boldsymbol{p}} \rangle$ and $\langle \hat{b}^\dagger_{\boldsymbol{p}} \hat{b}_{\boldsymbol{p}} \rangle$ which by, (2.42), gives us $\hat{s}_{i,z}(\boldsymbol{p})$. Each sublattice can be treated independently due to the imbalance in the chemical potential, allowing each to be released from the trap separately. The $\hat{s}_{i,x}(\boldsymbol{p})$ and $\hat{s}_{i,y}(\boldsymbol{p})$ components can be accessed by first switching off the pairing and tunneling before switching off the trap. This is equivalent to rotating the observables Σ^x_i and Σ^y_i to Σ^z_i.

While the above steps are specific to the staggered topological superconductor, in principle any four component system in which the relevant observables can be accessed are susceptible to our method. For example, angle-resolved photo-

emission spectroscopy has been shown to be successful in measuring both spin textures [61] and orbital textures [62] in condensed matter systems.

Another issue is the prospect of disorder. Real systems are rarely translationally invariant, and as such the reciprocal space representation of the winding number is no longer valid. Luckily, the winding number is also expressible in terms of real space observables [10]. As long as a system with disorder continues to have an energy gap, the subsystem winding numbers can be accessed and our method is valid.

2.5 Conclusions

Here we have derived an analytic decomposition of the Chern number of four component topological superconductors and insulators into subsystem winding numbers. We show that each of these winding numbers is expressed in terms of the expectation values of a set of observable operators. Therefore, the Chern number of such systems can be experimentally accessed, assuming one can find a way of measuring these observables. It was shown numerically that the method works in the case of the quantum spin Hall effect, where the subsystems correspond to the spin components, and the sublattice degrees of freedom in the staggered $p + ip$ superconductor, where in both cases the phase diagram was accurately reproduced. The method can be viewed as a generalisation of the detection of Chern numbers from time-of-flight images [47, 45, 48]. As such the method is particularly suited to cold atom experiments, where multiple internal atomic states are often used to synthesise the pairing terms, spin-orbit couplings and gauge fields required for topological phases to emerge [63, 64, 65, 66, 67, 68]. Being able to independently measure the time-of-flight images of the components

is sufficient to be able to construct the subsystem winding numbers and hence the full Chern number.

The accuracy of the method is limited only by the entanglement between the components with respect to which the observables have been defined. We found that errors due to the discretisation of the Brillouin zone become significant as the subsystems become more entangled, which leads to the winding numbers becoming unreliable. Luckily, it is possible to use the observables to evaluate the subsystem winding numbers to probe the entanglements between the subsystems. Given that we can access the entanglement between the subsystems, we can make a judicious choice of partitions such that the entanglement between them is low. In both the case studies that are presented, any discrepancies between the true values and our method directly correspond to regions of the phase diagram for which the partitions are maximally entangled.

An open question is the generalisation of the analytic argument for the Chern number decomposition to n component systems. While Schmidt decompositions are hard to generalise for systems with more than two components [69], a possible avenue might be to use convoluted multi-partite Schmidt decompositions.

Chapter 3

Three Dimensional Topological Superconductors

1D and 2D TSs have been well studied, and there exist several tight binding models such as the Kitaev wire [30], the Kitaev honeycomb lattice [10], and the $p+ip$ superconductor [45] that have been studied extensively. The Kitaev wire has even been probed experimentally [70, 71, 72, 73, 74] in hybrid superconductor-semiconductor nano-wires, to some success. Through study of their tight binding models, they have been theoretically shown to exhibit topologically non-trivial quasi-particles; the Kitaev wire supports zero energy Majorana modes localised at its boundary; the Kitaev honeycomb lattice and $p + ip$ superconductor trap Majorana fermions trapped at the center of vorticies [75, 76]. Surprisingly, at the time of the inception of this work, little effort had been afforded to the study of 3D TS tight binding models [77, 78].

There has been intense work in the search for topological superconductivity in real materials. Of particular note are $Cu_xBi_2Se_3$ [79] and $Sn_{1-x}In_xTe$ [80]. Both share the same effective description, developed by Fu and Berg [81]. Both of these materials have been studied at their surfaces extensively, with some strong

evidence of non-trivial pairing occurring. However there has been no conclusive detection of topological superconductivity, such as direct measurement of the bulk invariant. There already exist a few examples of TS tight binding models. The earliest example is Schnyder *et al.*'s construction of an inter-penetrating diamond lattice model in the symmetry class CI [82]. The model supports phases where the three dimensional winding number takes values $\nu_{3D} = 0, \pm 2$. Shortly afterwards, Fu and Berg's contribution came in the form of a model related to the known superconductor $Cu_xBi_2Se_3$, which was shown to be in the symmetry class DIII and to support winding numbers $\nu_{3D} = 0, \pm 1$[81]. Of particular note, was Deng *et al.*'s brilliant work in developing a systematic protocol for constructing tight binding models for TIs and TSs that can support arbitrary winding numbers [83]. Through a beautiful quaternionic construction, they are able to realise tight binding models in the symmetry classes that support topological indexes in the $\mathbb{Z}$ domain. While through this process they achieve arbitrary winding numbers, for higher winding numbers they require correspondingly long range interactions.

We chose to develop a model in the symmetry class DIII. Such models are characterised by possessing both TR, PH, and by implication SL, symmetries. We choose our system to have two species of fermion, which can be interpreted as a spin degree of freedom. Furthermore, we enforce a maximum interaction length. To each interaction within the maximum interaction length we assign a parameter λ_i which may be real or complex depending on the type of interaction. Together they form a vector $\boldsymbol{\lambda}$ which is a point on a manifold $\mathcal{M} \subset \mathbb{R}^N \times \mathbb{C}^M$. In order to identify specific example models we perform a random search in $\mathcal{M}$, where possible calculating the topological invariant and determining if it is non-zero. Through this process we arrive at four different models that all exhibit a variety of topological phases. All of the models present zero energy helical Majorana modes,

exponentially localised at their boundary, which present as modes crossing zero energy in the energy spectrum [84]. When an effective Zeeman field is applied to their boundary TR symmetry is broken [85, 86, 87], creating an energy gap. The resultant system on the boundary can be shown to be a 2D TS in its own right, with its own topological invariant. We find that the topological invariant of the bulk system and the boundary system coincide, and that this is no accident.

The rest of this chapter is divided into several sections. In Section 3.1 we define the general DIII model from which we will derive the specific examples. Section 3.2 discusses the definitions and conventions associated with the winding number in 3D. Section 3.3 outlines the numerical search procedure used to find topologically non-trivial examples. In Section 3.4 are presented the four examples models that support a variety of different winding numbers. Presented in Section 3.5 is an analysis of the boundary physics of each model.

3.1 The general model

We now present the generic model from which we shall derive the specific examples. Consider a cubic lattice onto which we place two different species of fermion $\hat{a}_1$ and $\hat{a}_2$, one at each vertex. We order the fermions periodically on the lattice such that we create a unit cell that lies along the x axis, as shown in fig. 3.1. To each unit cell we associate a spatial index $\boldsymbol{j} = \begin{pmatrix} j_x, & j_y, & j_z \end{pmatrix}$ which runs over the whole lattice. The tight binding Hamiltonian is given by

$$H = \sum_{\boldsymbol{j}} \left(\sum_{k} \left[\mu \hat{a}^{\dagger}_{k\boldsymbol{j}} \hat{a}_{k\boldsymbol{j}} \right] + \sum_{k,k',\boldsymbol{s}} \left[t_{kk'\boldsymbol{s}} \hat{a}^{\dagger}_{k\boldsymbol{j}} \hat{a}_{k'\boldsymbol{j}+\boldsymbol{s}} + \Delta_{kk'\boldsymbol{s}} \hat{a}_{k\boldsymbol{j}} \hat{a}_{k'\boldsymbol{j}+\boldsymbol{s}} \right] \right) + \text{H.c.}, \quad (3.1)$$

where $t_{kk'\boldsymbol{s}} \in \mathbb{R}$ and $\Delta_{kk'\boldsymbol{s}} \in \mathbb{C}$ are the tunneling and pairing coefficients respectively, $\mu \in \mathbb{R}$ is the chemical potential and $\boldsymbol{s} = s_x\hat{\boldsymbol{x}} + s_y\hat{\boldsymbol{y}} + s_z\hat{\boldsymbol{z}}$, with $s_x, s_y, s_z \in \mathbb{Z}$,

is a vector that connects different unit cells. We constrain the interactions to a maximum distance of $|\boldsymbol{s}| = \sqrt{2}$.

When we impose periodic boundary conditions we may transform the Hamiltonian (3.1) into reciprocal space using the Fourier transformation $\hat{a}_{k\boldsymbol{j}} = \sum_{\boldsymbol{p}} e^{i\boldsymbol{p}\cdot\boldsymbol{j}} \hat{a}_{k\boldsymbol{p}}$, where $\boldsymbol{p} = \begin{pmatrix} p_x, & p_y, & p_z \end{pmatrix} \in BZ = [0, 2\pi) \times [0, 2\pi) \times [0, 2\pi)$. The Hamiltonian can then be cast into Bogoliubov-de Gennes form $H = \sum_{\boldsymbol{p}} \boldsymbol{\psi}_{\boldsymbol{p}}^\dagger h(\boldsymbol{p}) \boldsymbol{\psi}_{\boldsymbol{p}}$, where $\boldsymbol{\psi}_{\boldsymbol{p}} = \begin{pmatrix} \hat{a}_{1,\boldsymbol{p}}, & \hat{a}_{1,-\boldsymbol{p}}^\dagger, & \hat{a}_{2,\boldsymbol{p}}, & \hat{a}_{2,-\boldsymbol{p}}^\dagger \end{pmatrix}^{\mathrm{T}}$ and the kernel Hamiltonian $h(\boldsymbol{p})$ is a 4×4 Hermitian matrix. We would like to restrict the Hamiltonian to the DIII symmetry class. As such we introduce two symmetry operators, the time reversal operator C_{TR} and the particle-hole operator C_{PH} and require that

$$Th(-\boldsymbol{p})T^{-1} = h(\boldsymbol{p}), \quad Ph(-\boldsymbol{p})P^{-1} = -h(\boldsymbol{p}) \tag{3.2}$$

where $T^2 = -1$ and $P^2 = 1$. We are free to choose explicit forms for these operators and as such we define $T = \sigma^y \otimes \mathbb{I}\mathcal{K}$ and $C_{\mathrm{PH}} = \mathbb{I} \otimes \sigma^x \mathcal{K}$.

For reasons that will become apparent shortly, we would like to unitarily rotate $h(\boldsymbol{p})$ into the spin triplet basis [88, 89]. Through application of the unitary

$$U_{\mathrm{s.t.}} = \frac{1}{\sqrt{2}} \begin{pmatrix} i & -1 & 0 & 0 \\ 0 & 0 & 1 & -i \\ i & 1 & 0 & 0 \\ 0 & 0 & 1 & i \end{pmatrix} \tag{3.3}$$

we place $h(\boldsymbol{p})$ in the basis

$$\boldsymbol{\psi}_{\boldsymbol{p}} = \begin{pmatrix} i\hat{a}_{1,\boldsymbol{p}} - \hat{a}_{1,-\boldsymbol{p}}^\dagger \\ \hat{a}_{2,\boldsymbol{p}} - i\hat{a}_{2,-\boldsymbol{p}}^\dagger \\ i\hat{a}_{1,\boldsymbol{p}} + \hat{a}_{1,-\boldsymbol{p}}^\dagger \\ \hat{a}_{2,\boldsymbol{p}} + i\hat{a}_{2,-\boldsymbol{p}}^\dagger \end{pmatrix} \tag{3.4}$$

such that the kernel takes the form

$$h(\boldsymbol{p}) = \begin{pmatrix} \epsilon(\boldsymbol{p})\mathbb{I} & \Theta(\boldsymbol{p}) \\ \Theta^\dagger(\boldsymbol{p}) & -\epsilon(\boldsymbol{p})\mathbb{I} \end{pmatrix} \tag{3.5}$$

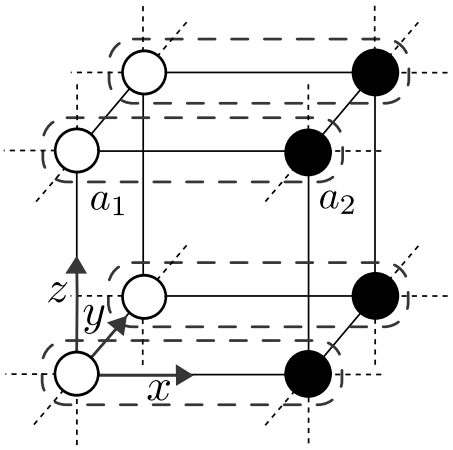

Figure 3.1: The cubic lattice onto which are placed Dirac fermions at the vertices. There are two species of fermion $\hat{a}_1$ and $\hat{a}_2$ that are placed alternately along the x axis. They form the unit cell that is indexed by $\boldsymbol{j} = (j_x, j_y, j_z)$.

where $\epsilon(\boldsymbol{p})$ denotes the *normal* state, $\mathbb{I}$ is the 2×2 identity matrix and $\Theta(\boldsymbol{p}) = i\left(\boldsymbol{d}(\boldsymbol{p}) \cdot \boldsymbol{\sigma}\right)\sigma^y$ is the spin triplet pairing function. The spin triplet form immediately allows us to access the degenerate energy spectrum $E_\pm(\boldsymbol{p}) = \pm\sqrt{\epsilon^2(\boldsymbol{p}) + |\boldsymbol{d}(\boldsymbol{p})|^2}$. We take the system to be in its lowest energy state, i.e. both negative valence bands are occupied. Due to the particle-hole symmetric nature of the spectrum, the system's energy gap is given by $\Delta E = \min_{\boldsymbol{p}}\left[E_+(\boldsymbol{p})\right]$.

3.2 3D winding number

Winding around the 3-sphere

We can determine the topological nature of the gapped regions of the phase diagram by calculating the 3D winding number, $\nu_{3\mathrm{D}}$. While there are many different representations of $\nu_{3\mathrm{D}}$, we start with the definition that is commensurate

with that given for ν_{2D} in the previous chapter. That definition is as follows [89]

$$\nu_{3D} = \frac{1}{12\pi^2}\int_{BZ} d^3p\ \epsilon^{ijk}\epsilon^{abcd}\hat{\eta}_a\partial_i\hat{\eta}_b\partial_j\hat{\eta}_c\partial_k\hat{\eta}_d \tag{3.6}$$

where BZ $= T^3$ and $\boldsymbol{\eta}(\boldsymbol{p}) = (d_1(\boldsymbol{p}), d_2(\boldsymbol{p}), d_3(\boldsymbol{p}), \epsilon(\boldsymbol{p}))$ is a 4-vector that maps between the BZ and S^3. As in the ν_{2D} case, as the BZ is spanned (3.6) counts the number of times $\hat{\boldsymbol{\eta}}$ wraps around S^3. This representation is quite cumbersome, but luckily there exists a more concise and illuminating representation [89].

Pole counting

Consider the set of points $\{\boldsymbol{p}^*\}$ in the Brillouin Zone that satisfy

$$\boldsymbol{d}(\boldsymbol{p}^*) = 0. \tag{3.7}$$

These are the points in the BZ where $\boldsymbol{\eta}(\boldsymbol{p})$ points to the poles of S^3. Without loss of generality we can perform the rescaling $\epsilon(\boldsymbol{p}) \to a\epsilon(\boldsymbol{p})$, where $a \ll 1$. Taylor expanding $\boldsymbol{\eta}(\boldsymbol{p})$ around $\boldsymbol{p}^*$ we have

$$\eta_a(\boldsymbol{p}) = \partial_\beta d_a(\boldsymbol{p})\Big|_{\boldsymbol{p}=\boldsymbol{p}^*}(\boldsymbol{p}-\boldsymbol{p}^*)_\beta, \quad a = 1,2,3. \tag{3.8}$$

where $\eta_4 = \epsilon(\boldsymbol{p})$. Near $\boldsymbol{p}^*$ we approximate

$$\hat{\eta}_a(\boldsymbol{p}) = \frac{\partial_\beta d_a(\boldsymbol{p})\Big|_{\boldsymbol{p}=\boldsymbol{p}^*}(\boldsymbol{p}-\boldsymbol{p}^*)_\beta}{\epsilon(\boldsymbol{p}^*)}, \tag{3.9}$$

as $\sqrt{\eta_a\eta^a} \approx |\epsilon(\boldsymbol{p}^*)|$. This implies $\hat{\eta}_4(\boldsymbol{p}) = \frac{\epsilon(\boldsymbol{p}^*)}{|\epsilon(\boldsymbol{p}^*|} = \mathrm{sgn}\,[\epsilon(\boldsymbol{p}^*)]$. The derivative of the components of $\hat{\boldsymbol{\eta}}$ are given by

$$\begin{aligned}
\partial_\alpha\hat{\eta}_a(\boldsymbol{p}) =& \partial_\alpha\left(\frac{\partial_\beta d_a(\boldsymbol{p})\Big|_{\boldsymbol{p}=\boldsymbol{p}^*}(\boldsymbol{p}-\boldsymbol{p}^*)_\beta}{\epsilon(\boldsymbol{p}^*)}\right)\\
=& \frac{\partial_\beta d_a(\boldsymbol{p})\Big|_{\boldsymbol{p}=\boldsymbol{p}^*}}{\epsilon(\boldsymbol{p}^*)}\delta_{\alpha\beta}\\
=& \frac{\partial_\alpha d_a(\boldsymbol{p})\Big|_{\boldsymbol{p}=\boldsymbol{p}^*}}{\epsilon(\boldsymbol{p}^*)}.
\end{aligned} \tag{3.10}$$

We also have that, near $\boldsymbol{p}^*$, $\hat{\boldsymbol{d}}(\boldsymbol{p}) \approx \frac{\boldsymbol{d}(\boldsymbol{p})}{|\epsilon(\boldsymbol{p}^*)|}$. With this in mind we have

$$\det\left[J\left(\hat{\boldsymbol{d}}(\boldsymbol{p})\right)\right] = \pm 1 = \operatorname{sgn}\left(\det\left[J\left(\hat{\boldsymbol{d}}(\boldsymbol{p})\right)\right]\right), \tag{3.11}$$

where $J\left(\hat{\boldsymbol{d}}(\boldsymbol{p})\right)$ is the Jacobian. We split the integral over the sphere into two parts as the linear approximation is only well defined for one of the two poles (the surface area of the three-sphere is $2\pi^2$). We can now rewrite (3.6) as

$$\begin{aligned}
\nu_{3\mathrm{D}} &= \frac{1}{12}\sum_{\boldsymbol{p}=\boldsymbol{p}^*} \operatorname{sgn}\left[\epsilon(\boldsymbol{p}^*)\right]\epsilon^{ijk}\epsilon^{4abc}\frac{\partial_i d_a(\boldsymbol{p})\Big|_{\boldsymbol{p}=\boldsymbol{p}^*}\partial_j d_b(\boldsymbol{p})\Big|_{\boldsymbol{p}=\boldsymbol{p}^*}\partial_k d_c(\boldsymbol{p})\Big|_{\boldsymbol{p}=\boldsymbol{p}^*}}{|\epsilon(\boldsymbol{p}^*)|^3} \\
&= \frac{1}{2}\sum_{\boldsymbol{p}=\boldsymbol{p}^*} \operatorname{sgn}\left[\epsilon(\boldsymbol{p}^*)\right]\frac{\det\left[J\left(\boldsymbol{d}(\boldsymbol{p})\right)\right]}{|\epsilon(\boldsymbol{p}^*)|^3} \\
&= \frac{1}{2}\sum_{\boldsymbol{p}=\boldsymbol{p}^*} \operatorname{sgn}\left[\epsilon(\boldsymbol{p}^*)\right]\det\left[\frac{1}{|\epsilon(\boldsymbol{p}^*)|}J\left(\boldsymbol{d}(\boldsymbol{p})\right)\right] \\
&= \frac{1}{2}\sum_{\boldsymbol{p}=\boldsymbol{p}^*} \operatorname{sgn}\left[\epsilon(\boldsymbol{p}^*)\right]\det\left[J\left(\hat{\boldsymbol{d}}(\boldsymbol{p})\right)\right] \\
&= \frac{1}{2}\sum_{\boldsymbol{p}=\boldsymbol{p}^*} \operatorname{sgn}\left[\epsilon(\boldsymbol{p}^*)\right]\operatorname{sgn}\left[\det\left[J\left(\hat{\boldsymbol{d}}(\boldsymbol{p})\right)\right]\right] \\
&= \frac{1}{2}\sum_{\boldsymbol{p}=\boldsymbol{p}^*} \operatorname{sgn}\left[\epsilon(\boldsymbol{p}^*)\right]\operatorname{sgn}\left[\frac{1}{|\epsilon(\boldsymbol{p}^*)|^3}\det\left[J\left(\boldsymbol{d}(\boldsymbol{p})\right)\right]\right] \\
&= \frac{1}{2}\sum_{\boldsymbol{p}=\boldsymbol{p}^*} \operatorname{sgn}\left[\epsilon(\boldsymbol{p}^*)\right]\operatorname{sgn}\left(\frac{1}{|\epsilon(\boldsymbol{p}^*)|^3}\right)\operatorname{sgn}\left[\det\left[J\left(\boldsymbol{d}(\boldsymbol{p})\right)\right]\right] \\
&= \frac{1}{2}\sum_{\boldsymbol{p}=\boldsymbol{p}^*} \operatorname{sgn}\left[\epsilon(\boldsymbol{p}^*)\right]\operatorname{sgn}\left[\det\left[J\left(\boldsymbol{d}(\boldsymbol{p})\right)\right]\right],
\end{aligned} \tag{3.12}$$

or

$$\nu_{3\mathrm{D}} = \frac{1}{2}\sum_{\boldsymbol{p}=\boldsymbol{p}^*} \operatorname{sgn}\left[\epsilon(\boldsymbol{p}^*)\right]\operatorname{sgn}\left[\det\left[J\left(\boldsymbol{d}(\boldsymbol{p})\right)\right]\right]. \tag{3.13}$$

This form follows from the fact that in order for $\hat{\boldsymbol{\eta}}(\boldsymbol{p})$ to wrap S^3, it must pass through the poles. What is nice about this representation is it explicitly shows

the dependence of the sgn $[\nu_{3D}]$ on the sign of the couplings Δ and μ.

Projectors

For the subsequent numerical evaluations of ν_{3D} a different representation of the winding number was used. As discussed in Sec. 1.2.3, a Hamiltonian which obeys SL symmetry can be brought into block-off-diagonal form

$$h(\boldsymbol{p}) = \begin{pmatrix} 0 & D(\boldsymbol{p}) \\ D^\dagger(\boldsymbol{p}) & 0 \end{pmatrix}. \tag{3.14}$$

Given (3.14) we can define a projection operator

$$Q(\boldsymbol{p}) = \begin{pmatrix} 0 & q(\boldsymbol{p}) \\ q^\dagger(\boldsymbol{p}) & 0 \end{pmatrix} \tag{3.15}$$

where $q(\boldsymbol{p}) = -\frac{D(\boldsymbol{p})}{E_+(\boldsymbol{p})}$. The winding number is defined as a map between the Brillouin zone and the space of projection operators $Q(\boldsymbol{p})$

$$\nu_{3D} = \frac{1}{24\pi^2} \int_{BZ} d^3p \; \epsilon^{ijk} \mathrm{tr} \left[\left(q^{-1}\partial_i q\right) \left(q^{-1}\partial_j q\right) \left(q^{-1}\partial_k q\right) \right]. \tag{3.16}$$

3.3 Numerical search method

We now address how we arrive at models with specific sets of couplings. The coupling coefficients of the general model, μ, $\Delta_{kk'\boldsymbol{s}}$ and $t_{kk'\boldsymbol{s}}$, form a space $\mathcal{M} = \mathbb{R}^2 \times \mathbb{C}^{56}$ we call *parameter space* (the chemical potentials are restricted to be real while all other parameters are allowed to be complex). As such, a point $\boldsymbol{\lambda} = \left(\lambda_1, \;\; \ldots \,, \;\; \lambda_{58}\right) \in \mathcal{M}$ defines a specific example of a model. In order to find a specific model with a non-trivial winding number we perform a random search within parameter space. To each coefficient λ_i we assign a normal distribution with standard deviation $\sigma = 2$, centered about zero. In the case of complex coefficients the distribution is two dimensional over the complex plane. Then the following procedure is followed

1. Sample a point $\boldsymbol{\lambda}_\alpha \in \mathcal{M}$.

2. Compute $\Delta E(\boldsymbol{\lambda}_\alpha)$.

3. If $\Delta E(\boldsymbol{\lambda}_\alpha) \neq 0$ compute $\nu_{3\mathrm{D}}(\boldsymbol{\lambda}_\alpha)$, else return to step 1.

4. If $\nu_{3\mathrm{D}}(\boldsymbol{\lambda}_\alpha) \neq 0$ store $\boldsymbol{\lambda}_\alpha$, else return to step 1.

5. Return to step 1.

After repeating this protocol for a sufficiently long period of time we have a set of points $\{\boldsymbol{\lambda}_\alpha\}$ that return non-zero winding numbers. At this stage, the elements of each $\boldsymbol{\lambda}_\alpha$ are not 'nice' numbers. We can attempt to change this by incrementally varying each $(\boldsymbol{\lambda}_\alpha)_i$ to an integer value without allowing the energy gap to close; by preventing the energy gap from closing, we assure that the winding number remains constant. Through this process we arrive at a 'nice' value for $\boldsymbol{\lambda}_\alpha$. Finally, we can choose to parametrise our Hamiltonian in a variety of ways. The simplest and most natural way is to associate a single parameter μ to all chemical potential terms, a single parameter t to all tunneling terms, and a single parameter Δ to all pairing terms. We can now explore the phase diagram of each model and perform the usual analyses.

3.4 Specific models

In this section we present four different specific examples of models that support a variety of winding numbers. The four models with Hamiltonians H_1, H_2, H_3, and H_4 support winding numbers $\nu_{3\mathrm{D}} = 0, \pm 1$, $\nu_{3\mathrm{D}} = 0, \pm 2$, $\nu_{3\mathrm{D}} = 0, \pm 1, \pm 3$, and $\nu_{3\mathrm{D}} = 0, \pm 2, \pm 4$ respectively.

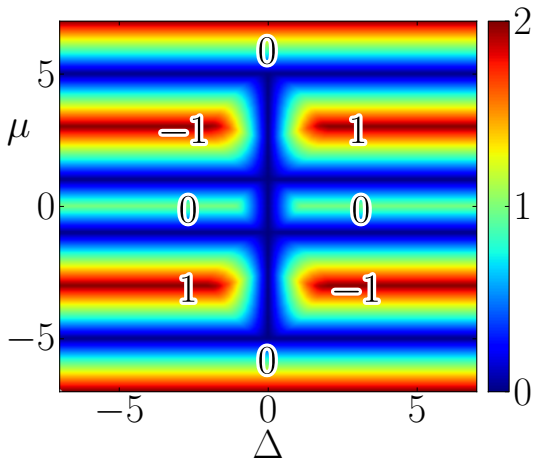

Figure 3.2: The phase diagram of the $\nu_{3D} = \pm 1$ model. The colour map shows the energy gap ΔE as a function of the chemical potential μ and the pairing coefficient Δ. The phase space is separated into eight different gapped regions separated by gapless lines. The number in each gapped region indicates the value of ν_{3D} in that phase as computed via (3.16) . The energy gap is in units of t.

3.4.1 Model 1: $\nu_{3D} = 0, \pm 1$

The real space tight binding Hamiltonian H_1 is given by

$$\begin{aligned}\hat{H}_1 = \sum_{\boldsymbol{j}} \Bigg\{ \sum_{k=1,2} \Big[& \mu \hat{a}^\dagger_{k,\boldsymbol{j}} \hat{a}_{k,\boldsymbol{j}} + \frac{1}{2} \\ & + t\hat{a}^\dagger_{k,\boldsymbol{j}} \hat{a}_{k,\boldsymbol{j}-\hat{\boldsymbol{x}}} + 2t\hat{a}^\dagger_{k,\boldsymbol{j}} \hat{a}_{k,\boldsymbol{j}-\hat{\boldsymbol{x}}+\hat{\boldsymbol{z}}} + t\hat{a}^\dagger_{k,\boldsymbol{j}} \hat{a}_{k,\boldsymbol{j}+\hat{\boldsymbol{y}}} + t\hat{a}^\dagger_{k,\boldsymbol{j}} \hat{a}_{k,\boldsymbol{j}-\hat{\boldsymbol{y}}+\hat{\boldsymbol{z}}} \\ & + \Delta \hat{a}_{k,\boldsymbol{j}} \hat{a}_{k,\boldsymbol{j}-\hat{\boldsymbol{x}}} + \Delta \hat{a}_{k,\boldsymbol{j}} \hat{a}_{k,\boldsymbol{j}-\hat{\boldsymbol{x}}+\hat{\boldsymbol{z}}} - \Delta \hat{a}_{k,\boldsymbol{j}} \hat{a}_{k,\boldsymbol{j}+\hat{\boldsymbol{y}}} + \Delta \hat{a}_{k,\boldsymbol{j}} \hat{a}_{k,\boldsymbol{j}-\hat{\boldsymbol{y}}+\hat{\boldsymbol{z}}} \Big] \\ & - 2i\Delta\big(\hat{a}_{1,\boldsymbol{j}} \hat{a}_{2,\boldsymbol{j}+\hat{\boldsymbol{y}}} + \hat{a}_{2,\boldsymbol{j}} \hat{a}_{1,\boldsymbol{j}+\hat{\boldsymbol{y}}}\big) + 2i\Delta\big(\hat{a}_{1,\boldsymbol{j}} \hat{a}_{1,\boldsymbol{j}+\hat{\boldsymbol{x}}+\hat{\boldsymbol{y}}} - \hat{a}_{2,\boldsymbol{j}} \hat{a}_{2,\boldsymbol{j}+\hat{\boldsymbol{x}}+\hat{\boldsymbol{y}}}\big) + \text{H.c.} \Bigg\},\end{aligned} \tag{3.17}$$

with $\mu, t, \Delta \in \mathbb{R}$. H_1 contains a mixture of s and p wave pairing terms without spin-orbit coupling terms. In reciprocal space the elements of the kernel Hamil-

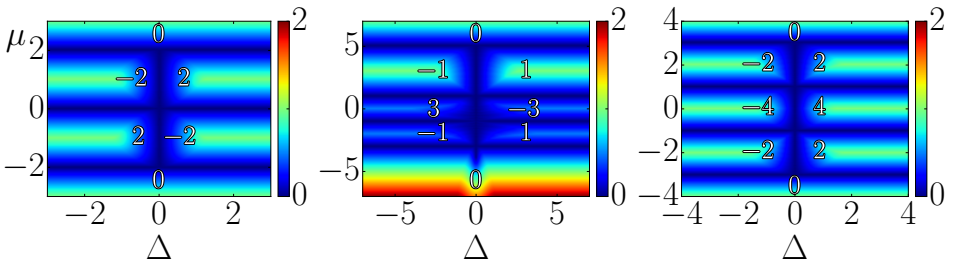

Figure 3.3: The phase diagrams for H_2, H_3 and H_4 from left to right respectively. The colour map encodes the bulk energy gap while the numbers show the value of the winding number in each gapped region. The energy gaps are in units of t.

tonian $h(\boldsymbol{p})$ are given by

$$\begin{aligned}
\epsilon(\boldsymbol{p}) &= t\Big[\cos(p_x - p_z) + \cos(p_x) + 2\cos(p_y - p_z) + \cos(p_y)\Big] - \mu, \\
d_x(\boldsymbol{p}) &= \Delta\Big[\sin(p_x - p_z) + \sin(p_x) + 2\sin(p_y - p_z) - \sin(p_y)\Big], \\
d_y(\boldsymbol{p}) &= 2\Delta\sin(p_y) \\
, d_z(\boldsymbol{p}) &= 2\Delta\sin(p_x + p_y).
\end{aligned} \tag{3.18}$$

The phase diagram as a function of μ and Δ, with $t = 1$, for H_1 is shown in fig. 3.2. There are eight distinct gapped regions separated by gapless lines. Of note is the adherence of the sign of ν_{3D} to the definition (3.13).

Below we present the real space Hamiltonians and components of (3.5) for each of the other three models.

3.4.2 Model 2: $\nu_{\mathbf{3D}} = 0, \pm 2$

The real space tight binding Hamiltonian H_2 is given by

$$\begin{aligned}\hat{H}_2 = \sum_{\boldsymbol{j}} \Bigg\{ \sum_{k=1,2} \Big[& \mu \hat{a}^\dagger_{k,\boldsymbol{j}} \hat{a}_{k,\boldsymbol{j}} + \frac{1}{2} + t \hat{a}^\dagger_{k,\boldsymbol{j}} \hat{a}_{k,\boldsymbol{j}-\hat{\boldsymbol{x}}} + t \hat{a}^\dagger_{k,\boldsymbol{j}} \hat{a}_{k,\boldsymbol{j}-\hat{\boldsymbol{x}}+\hat{\boldsymbol{z}}} \\ & - \Delta \hat{a}_{k,\boldsymbol{j}} \hat{a}_{k,\boldsymbol{j}+\hat{\boldsymbol{x}}} + \Delta \hat{a}_{k,\boldsymbol{j}} \hat{a}_{k,\boldsymbol{j}-\hat{\boldsymbol{x}}+\hat{\boldsymbol{z}}} \Big] - 2i\Delta \big(\hat{a}_{1,\boldsymbol{j}} \hat{a}_{2,\boldsymbol{j}+\hat{\boldsymbol{y}}} + \hat{a}_{2,\boldsymbol{j}} \hat{a}_{1,\boldsymbol{j}+\hat{\boldsymbol{y}}} \big) \\ & + 2i\Delta \big(\hat{a}_{1,\boldsymbol{j}} \hat{a}_{1,\boldsymbol{j}+\hat{\boldsymbol{x}}+\hat{\boldsymbol{y}}} - \hat{a}_{2,\boldsymbol{j}} \hat{a}_{2,\boldsymbol{j}+\hat{\boldsymbol{x}}+\hat{\boldsymbol{y}}} \big) + H.c. \Bigg\}. \end{aligned} \tag{3.19}$$

The spin-triplet form of $h(\boldsymbol{p})$ is given by the terms

$$\begin{aligned} \epsilon(\boldsymbol{p}) =& t \Big[\cos(p_x) + \cos(p_x - p_z) \Big] - \mu \\ d_x(\boldsymbol{p}) =& \Delta [\sin(p_x) + \sin(p_x - p_z)] \\ d_y(\boldsymbol{p}) =& 2\Delta \sin(p_y) \\ d_z(\boldsymbol{p}) =& 2\Delta \sin(p_x + p_y). \end{aligned} \tag{3.20}$$

The phase diagram for H_2 is shown in fig. 3.3 *left*.

3.4.3 Model 3: $\nu_{\mathbf{3D}} = 0, \pm 1, \pm 3$

The real space tight binding Hamiltonian H_3 is given by

$$\begin{aligned}\hat{H}_3 = \sum_{\boldsymbol{j}} \Bigg\{ \sum_{k=1,2} \Big[& \mu \hat{a}^\dagger_{k,\boldsymbol{j}} \hat{a}_{k,\boldsymbol{j}} + \frac{1}{2} \\ & + t \hat{a}^\dagger_{k,\boldsymbol{j}} \hat{a}_{k,\boldsymbol{j}-\hat{\boldsymbol{x}}} - t \hat{a}^\dagger_{k,\boldsymbol{j}} \hat{a}_{k,\boldsymbol{j}-\hat{\boldsymbol{x}}+\hat{\boldsymbol{z}}} - t \hat{a}^\dagger_{k,\boldsymbol{j}} \hat{a}_{k,\boldsymbol{j}+\hat{\boldsymbol{y}}} + t \hat{a}^\dagger_{k,\boldsymbol{j}} \hat{a}_{k,\boldsymbol{j}-\hat{\boldsymbol{y}}+\hat{\boldsymbol{z}}} - t \hat{a}^\dagger_{k,\boldsymbol{j}} \hat{a}_{k,\boldsymbol{j}+2\hat{\boldsymbol{y}}} \\ & - \Delta \hat{a}_{k,\boldsymbol{j}} \hat{a}_{k,\boldsymbol{j}-\hat{\boldsymbol{x}}} - \Delta \hat{a}_{k,\boldsymbol{j}} \hat{a}_{k,\boldsymbol{j}-\hat{\boldsymbol{x}}+\hat{\boldsymbol{z}}} - \Delta \hat{a}_{k,\boldsymbol{j}} \hat{a}_{k,\boldsymbol{j}+\hat{\boldsymbol{y}}} - 2\Delta \hat{a}_{k,\boldsymbol{j}} \hat{a}_{k,\boldsymbol{j}+\hat{\boldsymbol{y}}+\hat{\boldsymbol{z}}} \Big] \\ & - 2i\Delta \big(\hat{a}_{1,\boldsymbol{j}} \hat{a}_{2,\boldsymbol{j}+\hat{\boldsymbol{y}}} + \hat{a}_{2,\boldsymbol{j}} \hat{a}_{1,\boldsymbol{j}+\hat{\boldsymbol{y}}} \big) + 2i\Delta \big(\hat{a}_{1,\boldsymbol{j}} \hat{a}_{1,\boldsymbol{j}-\hat{\boldsymbol{x}}+\hat{\boldsymbol{y}}} - \hat{a}_{2,\boldsymbol{j}} \hat{a}_{2,\boldsymbol{j}-\hat{\boldsymbol{x}}+\hat{\boldsymbol{y}}} \big) + \text{H.c.} \Bigg\}. \end{aligned} \tag{3.21}$$

The spin-triplet form of $h(\boldsymbol{p})$ is given by the terms

$$\begin{aligned}
\epsilon(\boldsymbol{p}) =& -t\Big[-\cos(p_x)+\cos(p_x-p_z)+\cos(2p_y)-\cos(p_y+p_z)+\cos(p_y)\Big]+\mu\\
d_x(\boldsymbol{p}) =& \Delta[-\sin(p_x)-\sin(p_x-p_z)+\sin(2p_y)-\sin(p_y)-\sin(p_y+p_z)]\\
d_y(\boldsymbol{p}) =& 2\Delta\sin(p_y)\\
d_z(\boldsymbol{p}) =& 2\Delta\sin(p_x-p_y).
\end{aligned} \tag{3.22}$$

3.4.4 Model 4: $\nu_{\mathbf{3D}} = 0, \pm 2, \pm 4$

The real space tight binding Hamiltonian H_4 is given by

$$\begin{aligned}
\hat{H}_4 = \sum_{\boldsymbol{j}} \Bigg\{ \sum_{k=1,2} \Big[& \mu \hat{a}^\dagger_{k,\boldsymbol{j}} \hat{a}_{k,\boldsymbol{j}} + \frac{1}{2} - 2t \hat{a}^\dagger_{k,\boldsymbol{j}} \hat{a}_{k,\boldsymbol{j}-\hat{\boldsymbol{y}}} + t \hat{a}^\dagger_{k,\boldsymbol{j}} \hat{a}_{k,\boldsymbol{j}-\hat{\boldsymbol{x}}-\hat{\boldsymbol{z}}} \\
& + \Delta \hat{a}_{k,\boldsymbol{j}} \hat{a}_{k,\boldsymbol{j}+\hat{\boldsymbol{x}}+\hat{\boldsymbol{z}}} \Big] + 2i\Delta\big(\hat{a}_{1,\boldsymbol{j}} \hat{a}_{2,\boldsymbol{j}+\hat{\boldsymbol{z}}} + \hat{a}_{2,\boldsymbol{j}} \hat{a}_{1,\boldsymbol{j}+\hat{\boldsymbol{z}}}\big) \\
& + 2i\Delta\big(\hat{a}_{1,\boldsymbol{j}} \hat{a}_{1,\boldsymbol{j}+\hat{\boldsymbol{x}}+\hat{\boldsymbol{y}}} - \hat{a}_{2,\boldsymbol{j}} \hat{a}_{2,\boldsymbol{j}+\hat{\boldsymbol{x}}+\hat{\boldsymbol{y}}}\big) + H.c. \Bigg\}.
\end{aligned} \tag{3.23}$$

The spin-triplet form of $h(\boldsymbol{p})$ is given by the terms

$$\begin{aligned}
\epsilon(\boldsymbol{p}) =& t\Big[\cos(p_x+p_z)-2\cos(p_y)\Big]+\mu\\
d_x(\boldsymbol{p}) =& -\Delta\sin(p_x+p_z)\\
d_y(\boldsymbol{p}) =& -2\Delta\sin(p_z)\\
d_z(\boldsymbol{p}) =& 2\Delta\sin(p_x+p_y).
\end{aligned} \tag{3.24}$$

3.5 Boundary properties

As in many systems in physics, interesting things happen on the boundary. In this spirit, we now study the physics of the boundary of our models. For this purpose, we consider the lattice to extend between two parallel planes, both perpendicular to the z axis. The Bottom plane (B) is positioned at $z = 1$ and the Top plane

(T) is positioned at $z = l$, where l is a positive integer. The lattice is periodic in the x and y directions. It is necessary to specify that we consider the boundary *as a whole* to consist of the combination of these two surfaces. As such, any subsequent reference to 'the boundary' refers to the union of both the top and bottom surfaces. The generic Hamiltonian the system is given by

$$\hat{H}_\circ = \hat{H} + \hat{H}_\Omega, \quad H_\Omega = \sum_{\boldsymbol{j}} \boldsymbol{\psi}_\Omega^\dagger \boldsymbol{B} \cdot \boldsymbol{\sigma} \boldsymbol{\psi}_\Omega, \tag{3.25}$$

where $\boldsymbol{\psi}_\Omega = \begin{pmatrix} \hat{a}_{1,\boldsymbol{j}} & \hat{a}_{2,\boldsymbol{j}} \end{pmatrix}^{\mathrm{T}}$ and $\boldsymbol{B} = \begin{pmatrix} B_x & B_y & B_z \end{pmatrix}^{\mathrm{T}} \in \mathbb{R}$ with $\boldsymbol{B} = 0$ for $1 < j_z < N_z$. The boundary term H_Ω can be viewed as an effective Zeeman field. The reciprocal space form of (3.25) is given by

$$\hat{H}_\circ = \sum_{\bar{\boldsymbol{p}},\boldsymbol{z},\boldsymbol{s}} \boldsymbol{\psi}^\dagger_{\boldsymbol{z},\bar{\boldsymbol{p}}} h(\bar{\boldsymbol{p}}) \boldsymbol{\psi}_{\boldsymbol{z},\bar{\boldsymbol{p}}} + \sum_{\bar{\boldsymbol{p}}} \left(\boldsymbol{\psi}^\dagger_{1,\bar{\boldsymbol{p}}} h_B \boldsymbol{\psi}_{1,\bar{\boldsymbol{p}}} + \boldsymbol{\psi}^\dagger_{l,\bar{\boldsymbol{p}}} h_T \boldsymbol{\psi}_{l,\bar{\boldsymbol{p}}} \right) \tag{3.26}$$

where $\boldsymbol{\psi}_{\boldsymbol{z},\bar{\boldsymbol{p}}} = \bigoplus_z \begin{pmatrix} \hat{a}_{1,z,\bar{\boldsymbol{p}}}, & \hat{a}^\dagger_{1,z,-\bar{\boldsymbol{p}}}, & \hat{a}_{2,z,\bar{\boldsymbol{p}}}, & \hat{a}^\dagger_{2,z,-\bar{\boldsymbol{p}}} \end{pmatrix}^{\mathrm{T}}$, z is the position in the z direction, and $\bar{\boldsymbol{p}} \in [0, 2\pi) \times [0, 2\pi) = \mathrm{BZ}_{2\mathrm{D}}$. The kernel Hamiltonian is a Hermitian matrix of dimension $4N_z$ that contains the coupling and phase information of the bulk system. We choose this basis for (3.26) to ease subsequent discussion of the boundary fields and their physics. The terms h_B and h_T encode additional on site interactions that lie on the bottom and top z planes, respectively. For our purposes, we choose $h_B = h_T = \boldsymbol{B} \cdot \boldsymbol{\sigma} \otimes \mathbb{I}$. They correspond to inter-species couplings within the unit cell. We note that if $\boldsymbol{B} \neq 0$ then $\left\{ h_{B/T}, C_{\mathrm{TR}} \right\} = 0$ meaning that terms $h_{B,T}$ break time-reversal symmetry on the boundary.

3.5.1 Zero energy Majorana edge states

We begin our analysis by taking $\boldsymbol{B} = 0$. When $\nu_{3\mathrm{D}} \neq 0$, bulk-boundary correspondence requires that the model supports a number of gapless chiral edge

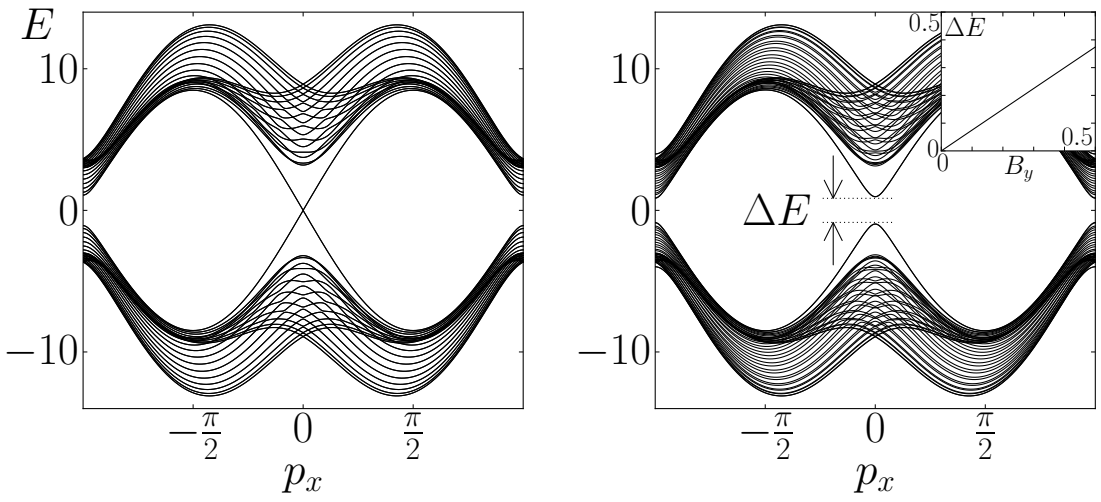

Figure 3.4: *Left* A cross section of the energy dispersion at $p_y = 0$ for model H_1 while in the $\nu_{3D} = 1$ phase ($t = 1$, $\Delta = 2$, $\mu = 3$) with open boundaries at $z = 1$ and $z = 20$. A single double degenerate cone appears, with each state corresponding to one of the two open surfaces. *Right* When the Zeeman field on the boundary takes value $B_y \neq 0$ the gapless modes acquire a gap $\Delta E_\circ$. *Inset* The energy gap $\Delta E_\circ$ as a function of B_y.

modes $N_\circ = |\nu_{3D}|$ at each surface. Furthermore, all edge modes on a given surface have the same chirality [17]. Such states manifest as 2D gapless Majorana cones in the dispersion relation. This behavior is shown for the H_1 model in fig. 3.4 *left*. The spectrum is doubly degenerate and has two so called Dirac cones, one per surface, as depicted in fig 3.5. For the models that support higher winding numbers, the configuration of zero energy Majorana cones on their boundaries is depicted in fig. 3.6. The plots depict each model in the $\max(\nu_{3D})$ phase, clearly showcasing the $N_\circ = |\nu_{3D}|$ correspondence. If we place the model in the $\nu_{3D} = 0$ phase, we find that the constraint $N_\circ \neq \nu_{3D}$ no long holds.

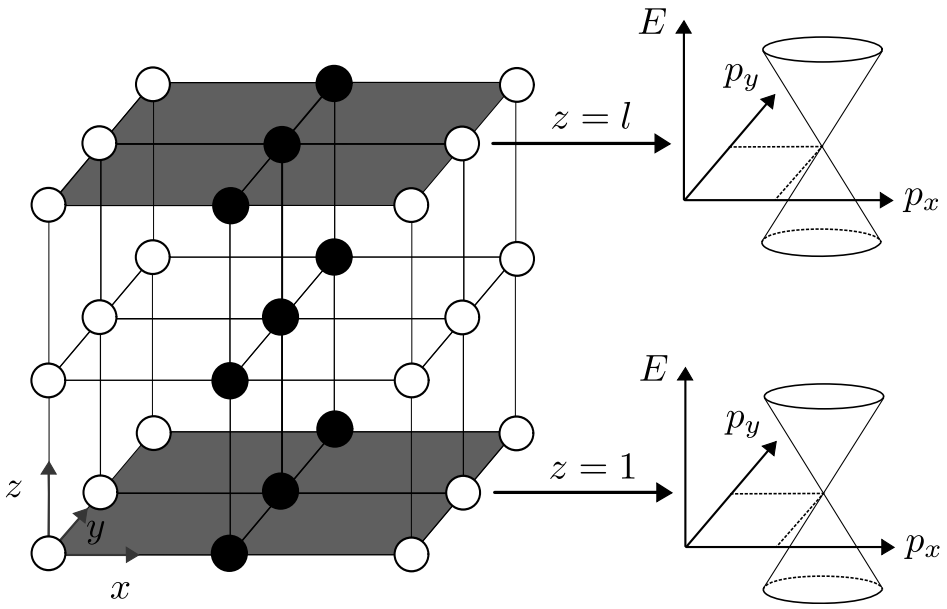

Figure 3.5: A schematic representation of the zero energy Majorana cones for the $\nu_{3D} = 1$ phase of H_1. The boundary of the system consists of two dislocated planes (T and B) lying at $z = 1$ and $z = l$. A single Majorana cone exists at each surface.

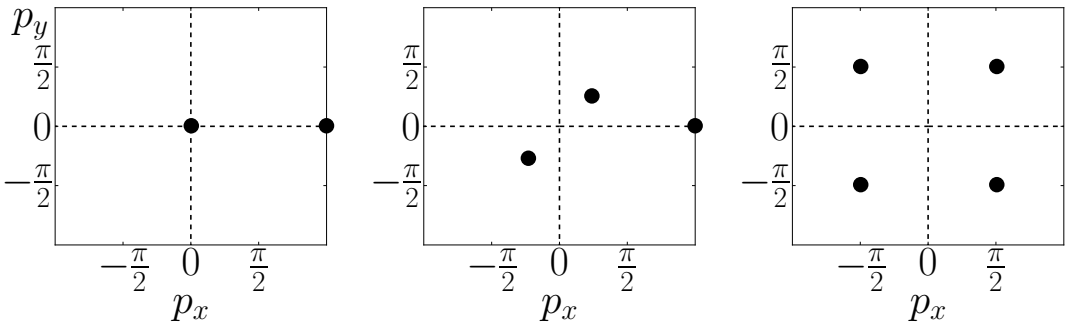

Figure 3.6: The center of the Majorana cones on the boundaries of models H_2, H_3, and H_4, ordered from left to right. The plots show each model in the $\max(\nu_{3D})$ phase ($\mu = 0.1$, $\Delta = t = 1$). The number of cones on each surface of the boundary $N_\circ$ is equal to ν_{3D}.

3.5.2 The boundary as a 2D TS in the class D

Turning on the Zeeman field with $\boldsymbol{B} \neq 0$, we find that the B_x and B_z terms change the position of the Majorana cones in the $\mathrm{BZ}_{\mathrm{2D}}$ plane. More usefully, when $B_y \neq 0$ we induce an energy gap $\Delta E_\circ$ in the surface states, as seen in fig. 3.4 *right* where the cones have become paraboloids. While it is entirely possible to treat each surface independently, if we take $h_B = h_T$ then the entire boundary can be considered as a single two dimensional TS in the symmetry class D [17] that is dislocated between the two surfaces that constitute the boundary. This class is characterised by preserving the same kind of particle-hole symmetry as the class DIII while breaking time reversal symmetry. While the choice of $\mathrm{sgn}\,[B_y]$ is free, in order to make a valid comparison between the boundary and bulk systems, we enforce the constraint $\mathrm{sgn}\,[B_y] = \mathrm{sgn}\,[\Delta]$.

As with all TSs, we would like to determine their topological phase by evaluating the corresponding invariant. Happily, now that the edge states are gapped, we can associate a fractional 2D winding number $\nu_{\partial 2\mathrm{D}}(\triangledown)$ to each cone $\triangledown$ on each surface [5, 90]. It is defined in terms of the projector $P_{\bar{\boldsymbol{p}}}(\triangledown)$ onto each state and is given by

$$\nu_{\partial 2\mathrm{D}}(\triangledown) = -\frac{i}{2\pi}\int_{\mathrm{BZ}_{\mathrm{2D}}} d^2p\,\mathrm{tr}\Big(P_{\bar{\boldsymbol{p}}}(\triangledown)\big[\partial_{p_x}P_{\bar{\boldsymbol{p}}}(\triangledown), \partial_{p_y}P_{\bar{\boldsymbol{p}}}(\triangledown)\big]\Big). \tag{3.27}$$

To each surface we associate a *partial winding number* ν_b, where $b = T, B$, which is defined as the sum of all the fractional winding numbers of all the cones living on that surface

$$\nu_b = \sum_{\forall\triangledown \text{ on } b} \nu_{\partial 2\mathrm{D}}(\triangledown). \tag{3.28}$$

(μ,Δ,t)	$\nu_{\partial 2\mathrm{D}}(\nabla_T)$	$\nu_{\partial 2\mathrm{D}}(\nabla_B)$	$\nu_{2\mathrm{D}}$	$\nu_{3\mathrm{D}}$
$(3.0, 2.0, 1.0)$	0.505	0.504	1.009	$+1$
$(-3.0, -2.0, 1.0)$	0.505	0.499	1.004	$+1$
$(-3.0, 2.0, 1.0)$	-0.505	-0.499	-1.004	-1
$(3.0, -2.0, 1.0)$	-0.505	-0.504	-1.009	-1

Table 3.1: The numerical values for ν_T and ν_B are calculated by approximating the formula for the model H_1 system with $l = 5$ sites and $B_y = 0.025$. Because H_1 has a single cone $\nabla_{T/B}$ on each surface, we have $\nu_{T/B} = \nu_{\partial 2\mathrm{D}}(\nabla_{T/B})$. The fractional winding number $\nu_{\partial 2\mathrm{D}}$ is approximated from (3.27) applied to the individual Dirac cones $\nabla_{T/B}$ on the top and bottom surfaces. We confirm that $\nu_{2\mathrm{D}} = \sum_b \nu_b$, for $b = B, T$, and is in agreement with $\nu_{3\mathrm{D}}$.

Finally, we define the winding number $\nu_{2\mathrm{D}}$ of the whole boundary as the sum of the partial winding numbers of both surfaces

$$\nu_{2\mathrm{D}} = \sum_b \nu_b. \tag{3.29}$$

In order to numerically evaluate (3.27) we must lift the degeneracy of all the ∇ on either surface. To do this, we vary B_x and B_z which shifts the cones on each surface in momentum space relative to one another, and allows us to distinguish the apex of each cone. The integral's primary contribution comes from the region around these apexes and therefore, after shifting the cones, we can get a good approximation of $\nu_{\partial 2\mathrm{D}}(\nabla)$ in each case.

Tab. 3.1 shows the output of such a numerical evaluation of the partial winding numbers for the H_1 model in all of the topologically non-trivial phases. We see the contribution to $\nu_{2\mathrm{D}}$ from each cone is fractional, with each one contributing $|\nu_{\partial 2\mathrm{D}}(\nabla)| \approx 0.5$. Furthermore, we have $\mathrm{sgn}\,[\nu_T] = \mathrm{sgn}\,[\nu_B]$; this is ensured by the fact that cones on opposite surfaces have *opposite helicities*, which compensates for the orientation of unit vector normal to each surface. When $\nu_{3\mathrm{D}} = 0$ we have

Model	Δ	ν_{3D}	ν_{2D}	$N_\circ$
H_2	$+1.0$	2.001	2.002	2
H_2	-1.0	-1.984	-2.007	2
H_3	$+1.0$	3.019	2.874	3
H_3	-1.0	-3.009	-2.876	3
H_4	$+1.0$	4.000	3.877	4
H_4	-1.0	-4.000	-3.880	4

Table 3.2: Numerical data for ν_{3D} and ν_{2D} for models H_2, H_3, and H_4 with $t = 2$ and $\mu = 0.1$. ν_{3D} was computed by approximating (3.6) and ν_{2D} can approximated from (3.27). In all cases $|B_y| \leq 0.05$ depending on the model. The number of Dirac cones for each model was counted manually.

$N_\circ = 2$ where cones on the *same* surface have opposite helicities. As such when computing $\nu_{\partial 2D}(\triangledown)$ the contributions from each cone differ sign. By (3.28), this means the partial winding numbers ν_b are zero for both surfaces, and by (3.29) $\nu_{2D} = 0$. The numerical values for ν_{3D} and ν_{2D} for the other models is shown in tab. 3.2.

What is becoming apparent is the correspondence between the bulk winding number, ν_{3D}, and the winding number of the boundary system, ν_{2D}. In fact, under the pre-agreed sign conventions, our numerical study finds that in all models

$$\nu_{3D} = \nu_{2D} \tag{3.30}$$

This *bulk-boundary correspondence* is robust, with the topological phase of the boundary changing only when the bulk system undergoes a phase transition. The phase transition of the boundary is driven by the change in the number of edge states at the boundary when ν_{3D} varies.

3.6 Conclusions

We have presented four distinct topological spin-triplet superconductors that support variety of bulk winding numbers. These models, while being novel in their own right, support a new manifestation of 2D TSs in the class D at their boundary. These 2D systems are composite, consisting of both the top and bottom surfaces that constitute the boundary of their 3D host model. The winding number associated to the 2D boundary model were found, both numerically and analytically, to be equal to the winding number of their bulk systems. This bulk-boundary correspondence in the topological phase is robust to changes in the phase of the bulk, such that a change of phase of the bulk leads to a corresponding change of phase of the boundary. Conversely, the phase of the boundary is protected by the robust nature of the topological phase of the bulk. The effect is a result of the stability of the number of surface states when the bulk has a non-zero winding number. Each surface state contributes an equal fraction of the overall 2D winding number, and the number of surface states at each surface is equal, as long as ν_{3D} remains the same so will ν_{2D}.

The spatial dislocation of the boundary system can provide further protection for external pertubations. As an example, consider placing a 2D system with $\nu_{2D} = \pm 1$ onto one of the surfaces. Such a 2D system has an effective description as a pair of massive Majorana fermions [10]. If we introduce some perturbative interactions between this invader and one of the surfaces of our 3D system, one of these massive Majoranas can pair with one of the Majorana edge modes on the boundary, resulting in a single massive Dirac fermion [15]. Crucially, these pair of massive Majoranas have opposite helicity and as such, when we adiabatically connect the two systems, only the Majoranas with opposite helicity will pair

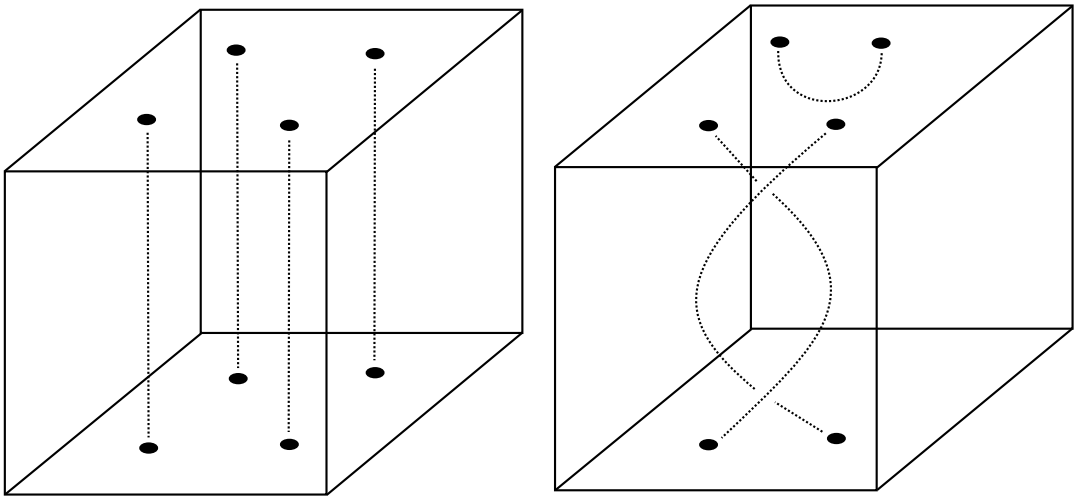

Figure 3.7: *Left* Four pairs of Majorana fermions into which one can encode a logical qubit. Each Majorana is at the terminus of a vortex that penetrates the bulk of the sample. Such a vortex has a finite string tension. *Right* Shows a pair of Majoranas created on the same surface. The finite string tension means such a creation will not propagate through the system and will quickly annihilate. Also shown is a pair of Majoranas braiding. The two Majoranas on the top surface are braided while their partners on the bottom surface remain static. The finite string tension means this logical operation is thermodynamically suppressed.

together. Therefore, the total number of Majoranas at the surface remains constant and their helicities are all the same and, by implication, the partial winding number associated with that surface remains constant.

The boundary system could potentially support non-Abelian anyons in the form of vortices that localise Majorana fermions at their centers [91, 92]. Consider fig. 3.7 *left* where we have created four vortex pairs such that each vortex terminates on opposite surfaces. It is possible to store, and manipulate through braiding operations, a single qubit in the degenerate ground space of a set of four Majorana fermions [33]. In this case, by braiding the vortices around one another, the Majorana fermions localise at their end points will undergo the stan-

dard unitary evolution associated with a braiding operation. What happens in the case of thermal errors in this system? Fig. 3.7 *right* shows a vortex whose ends terminate on the same surface. Such a vortex is typical of local thermal excitations. A finite density of such errors could lead to a phase transition due to vortex nucleation [93, 94]. However, the vortex strings have a finite energy which is proportional to the string length, also called a string tension [95]. As such, for sufficiently low temperatures, it will be energetically favorable for any vortex whose ends terminate on the same surface to shrink and eventually annihilate itself [96]. Vortices that terminate on different surfaces will reach an equilibrium when the length of the vortex is minimised, as shown in fig. 3.7 [97, 98]. The non-proliferation of vortex errors means that the topological phase of the boundary is protected, and any quantum information stored is safe.

Chapter 4

Defects on the Boundary of 3D Topological Superconductors

The study of zero energy modes localised at defects in topological condensed matter and other systems has been long and fruitful [99, 100, 101, 102, 103, 104, 105], from the prediction of solitons in polyacetylene [106, 107] and vortex fermions [108], to Majorana modes trapped at vortex cores in the $p + ip$ superconductor [109]. Specific experimental implementations that give rise to Majorana zero modes have been proposed in superconducting-insulating heterostructures [87] as well as semiconductor-superconductor heterostructures [110, 86, 111, 112].

The famed 10-fold way classification [17] was modified to classify the different kinds of defects that can arise in topological systems in various spatial dimensions [113]. By relating the dimension of a defect with the dimension of the system into which it is embedded, the traditional periodic table of symmetry classes tab. 1.1 is rewritten. The classes are no longer demarcated by the spatial dimension of the model d but by the parameter $\delta = d - D$, where D is the dimension of a surface that encloses the defect. The traditional AZ classification scheme considers only $D = 0$, i.e. defects that occur at the boundary of the system such as zero energy

Majorana fermions at the end of the Kitaev wire [30] or chiral edge modes of the quantum spin Hall effect [44].

We are interested in three particular elements of this revised periodic table. Namely class DIII with $\delta = 3 - 0$, class D with $\delta = 2 - 0$ and $\delta = 2 - 1$. Consider that we start with a topological superconductor in the class DIII with open boundary conditions in the z direction. As has been shown, 2D helical zero energy Majorana fermions are supported at its boundary. This configuration corresponds to the initial $\delta = 3 - 0$ configuration. We found that the introduction of a uniform Zeeman field over the boundary breaks time reversal symmetry and opens an energy gap. The boundary can be then be considered to be a class D topological superconductor in its own right. As we saw in the previous chapter, the topological invariants of the bulk and boundary systems were found to be in agreement. The purpose of the work in this chapter is to introduce defects of dimension $\delta = 2 - 0$ and $\delta = 1 - 0$ onto this boundary class D system such that we trap zero energy Majorana modes of corresponding dimensionality.

Given some purely 2D class D topological superconductor, the introduction of a domain wall results in a number of chiral Majorana zero modes appearing. The nature of the domain wall and the value of the topological invariant determines the number of modes that appear. For example, a $p + ip$ superconductor with $\nu_{2D} = 1$ on a open ended cylinder supports one chiral edge mode per edge. More generally, given some interface between two systems with differing topological index, the number of zero modes at the interface is the absolute value of the difference in the indicies of each system. From this perspective, we would consider a topologically non-trivial system with an open boundary to be the interface between two systems, one with a non-zero and one with zero topological index. An

example of a case when we have a topologically non-trivial system on either side of the interface is the Kitaev wire with a change in the sign of the superconducting order parameter at some point in the chain. By the phase diagram Fig. 1.2, a change in the sign of the order parameter leads to a change in the sign of the winding number. The difference between the winding numbers of the two systems is two. The number of zero energy Majorana modes that appear at the interface is also two. This correspondence is enshrined in an index theorem [114]. Given two TS with bulk invariants ν_+ and ν_-, it is known that the number of gapless states N at the interface between the two systems is given by

$$N = |\nu_+ - \nu_-|. \tag{4.1}$$

A system with an open boundary is equivalent to having $\nu_- = 0$ and as such the number of gapless edge states is simply $|\nu_+|$.

We study the behavior of Majorana modes at the boundary of a 3D TS in class DIII, which has both particle-hole (PH) and time-reversal (TR) symmetries. We initially consider a 3D model periodic in all three spatial dimensions that is characterised by a 3D winding number $\nu_{3D} \in \mathbb{Z}$. We then create a boundary by breaking the periodicity in the z direction. The two disconnected surfaces naturally support gapless helical Majorana modes exponentially localised at the boundary. In order to gap these modes we introduce a TR-breaking Zeeman field thus effectively creating a 2D TS in class D. The topological phases at each boundary are unlike purely 2D TS as each of the two surfaces of the boundary is described by partial Chern numbers. As each surface can be manipulated independently it is intriguing to investigate how Majorana modes configure themselves around a variety of defects. To probe this we first introduce line defect in the Zeeman field between two regions with opposite field orientation. We numerically demonstrate

that localised 1D Majorana modes live along these defect lines. In order to create 0D Majorana modes, we consider crossing 1D defect lines in the configuration of the effective Zeeman field. We demonstrate that quasi-0D Majorana modes are localised in the crossing points. We demonstrate our analysis for TS with $\nu_{3\mathrm{D}} = 1$ and $\nu_{3\mathrm{D}} = 2$. Overall we observe a generalisation of the well known index theorem (4.1) that determines the number of states at the interface between two system of differing bulk topological invariant. Motivated by this we demonstrate that the number of gapless Majorana modes is the difference in the partial contributions to the Chern number of the boundary system, either side of a magnetic domain wall.

In Section 4.1 we introduce the notation and conventions associated with the real space representations of the Hamiltonian. Section 4.2.1 outlines the nature of the open boundaries and definitions and notation associated with the effective Zeeman field. Section 4.3 introduces a Zeeman field configuration with 1D magnetic domain walls. We present numerical and analytical evidence showing this induces dimensional reduction of the surface states from 2D to 1D. Section 4.4 introduces the 'chessboard' configuration of effective Zeeman fields. We present numerical evidence showing the reduction of the Majorana modes from 2D to 0D. Finally, in section 4.5 we summarise the preceding sections and suggest possible implementations using magnetic impurities or superconducting-to-magnetic material heterostructures.

4.1 Real space eigenvalues, eigenvectors and spectral fermions

We can factorise the Hamiltonian

$$\begin{aligned}\hat{H}_1 = \sum_{\boldsymbol{j}} \Bigg\{ \sum_{k=1,2} \Big[& \mu \hat{a}^\dagger_{k,\boldsymbol{j}} \hat{a}_{k,\boldsymbol{j}} + \frac{1}{2} \\ & + t\hat{a}^\dagger_{k,\boldsymbol{j}} \hat{a}_{k,\boldsymbol{j}-\hat{\boldsymbol{x}}} + 2t\hat{a}^\dagger_{k,\boldsymbol{j}} \hat{a}_{k,\boldsymbol{j}-\hat{\boldsymbol{x}}+\hat{\boldsymbol{z}}} + t\hat{a}^\dagger_{k,\boldsymbol{j}} \hat{a}_{k,\boldsymbol{j}+\hat{\boldsymbol{y}}} + t\hat{a}^\dagger_{k,\boldsymbol{j}} \hat{a}_{k,\boldsymbol{j}-\hat{\boldsymbol{y}}+\hat{\boldsymbol{z}}} \\ & + \Delta \hat{a}_{k,\boldsymbol{j}} \hat{a}_{k,\boldsymbol{j}-\hat{\boldsymbol{x}}} + \Delta \hat{a}_{k,\boldsymbol{j}} \hat{a}_{k,\boldsymbol{j}-\hat{\boldsymbol{x}}+\hat{\boldsymbol{z}}} - \Delta \hat{a}_{k,\boldsymbol{j}} \hat{a}_{k,\boldsymbol{j}+\hat{\boldsymbol{y}}} + \Delta \hat{a}_{k,\boldsymbol{j}} \hat{a}_{k,\boldsymbol{j}-\hat{\boldsymbol{y}}+\hat{\boldsymbol{z}}} \Big] \\ & - 2i\Delta\big(\hat{a}_{1,\boldsymbol{j}} \hat{a}_{2,\boldsymbol{j}+\hat{\boldsymbol{y}}} + \hat{a}_{2,\boldsymbol{j}} \hat{a}_{1,\boldsymbol{j}+\hat{\boldsymbol{y}}}\big) + 2i\Delta\big(\hat{a}_{1,\boldsymbol{j}} \hat{a}_{1,\boldsymbol{j}+\hat{\boldsymbol{x}}+\hat{\boldsymbol{y}}} - \hat{a}_{2,\boldsymbol{j}} \hat{a}_{2,\boldsymbol{j}+\hat{\boldsymbol{x}}+\hat{\boldsymbol{y}}}\big) + \text{H.c.} \Bigg\},\end{aligned} \tag{4.2}$$

into the form

$$H = \Psi^\dagger \Lambda \Psi, \quad \text{where} \quad \Psi = \bigoplus_{\boldsymbol{j}} \begin{pmatrix} \hat{a}_{1,\boldsymbol{j}} \\ \hat{a}^\dagger_{1,\boldsymbol{j}} \\ \hat{a}_{2,\boldsymbol{j}} \\ \hat{a}^\dagger_{2,\boldsymbol{j}} \end{pmatrix}. \tag{4.3}$$

The kernel Λ is a square matrix of dimension $\dim(\Lambda) = 4N_xN_yN_z$. The positive eigenvalues of Λ are enumerated E_n, $0 \leq n \leq \dim(\Lambda)/2$, where $E_1 \leq E_2 \leq ... \leq E_{\dim(\Lambda)/2}$. The eigenstates of Λ are given by

$$|\kappa_n\rangle = \sum_{\boldsymbol{j}} \sum_{k=1,2} \sum_{\rho=\bullet,\circ} \alpha_{\boldsymbol{j}k\rho} \, |\boldsymbol{j}\rangle \otimes |k\rho\rangle \,, \tag{4.4}$$

where $|\boldsymbol{j}\rangle$ are the position basis states and $|k\rho\rangle$ are mode basis states given by

$$\begin{aligned} |1\bullet\rangle &= (1,0,0,0), & |1\circ\rangle &= (0,1,0,0), \\ |2\bullet\rangle &= (0,0,1,0), & |2\circ\rangle &= (0,0,0,1). \end{aligned} \tag{4.5}$$

In (4.4) the complex number $\alpha_{k\rho\boldsymbol{j}}$ is the amplitude of the $\hat{a}_k$ ($\rho = \bullet$) or $\hat{a}^\dagger_k$ ($\rho = \circ$) fermionic mode at the site $\boldsymbol{j}$. Particle-hole symmetry dictates that for every eigenstate $|\kappa_n\rangle$ with eigenvalue E_n there exists a conjugate state $|\kappa_{-n}\rangle$ with eigenvalue $E_{-n} = -E_n$ such that $|\kappa_{-n}\rangle = C_{\text{PH}} \, |\kappa_n\rangle$ where $C_{\text{PH}} = \bigoplus_{\boldsymbol{j}} \mathbb{I}_2 \otimes \sigma^x$.

The Hamiltonian (3.17) can be rewritten in the diagonal basis

$$H = \sum_n \Big(E_n \tilde{\hat{a}}_n^\dagger \tilde{\hat{a}}_n + E_{-n} \tilde{\hat{a}}_{-n}^\dagger \tilde{\hat{a}}_{-n} \Big), \tag{4.6}$$

where $\tilde{\hat{a}}_n = \langle \kappa_n | \, \Psi$ and $\tilde{\hat{a}}_n = \tilde{\hat{a}}_{-n}^\dagger$ (see Appendix A). These 'spectral' Dirac fermions obey the canonical fermionic anticommutation relations. We can decompose these fermions into spectral Majorana modes in the following way

$$\tilde{\hat{a}}_n = \frac{\tilde{\gamma}_{1,n} + i\tilde{\gamma}_{2,n}}{2}, \tag{4.7}$$

where $\tilde{\gamma}_{g,n} = \tilde{\gamma}_{g,n}^\dagger$ and $\{\tilde{\gamma}_{g,n}, \tilde{\gamma}_{g',n'}\} = 2\delta_{nn'}\delta_{gg'}$. In this basis Hamiltonian (4.6) is given by

$$H = i \sum_n E_n \tilde{\gamma}_{1,n} \tilde{\gamma}_{2,n}, \tag{4.8}$$

up to a constant shift in energy. It is possible to extract the amplitude of a given spectral Majorana fermion at a given site $\boldsymbol{j}$, hereby denoted $|\Gamma_{g,n}(\boldsymbol{j})|$, from the eigenstates of the kernel Λ (see Appendix A).

Each time we introduce a defect the Majorana modes may become localised around it. To describe this behavior we introduce a vector of real parameters, $\boldsymbol{\xi} = (\xi_x, \xi_y, \xi_z)$, that describes the localisation of a Majorana mode around a defect point, line or surface, in the following way. A spectral Majorana mode will decay as

$$|\Gamma_{g,n}(\boldsymbol{J})| \propto e^{-\|\boldsymbol{\xi}\cdot(\boldsymbol{j}-\boldsymbol{j}_0)\|}, \tag{4.9}$$

where $\xi_x, \xi_y, \xi_z \in \mathbb{R}$ are inversely proportional to the localisation length along their corresponding direction and $\|\boldsymbol{\xi} \cdot (\boldsymbol{j} - \boldsymbol{j}_0)\| = \sum_{i=x,y,z} |\xi_i (j_i - (j_0)_i)|$. The parameter $\boldsymbol{j}_0$ defines the point, line or plane to which a state is localised. For example, a state localised to the plane located at $z = N_z$ has $\boldsymbol{j}_0 = j_x\hat{\boldsymbol{x}} + j_y\hat{\boldsymbol{y}} + N_z\hat{\boldsymbol{z}}$, where $N_z\hat{\boldsymbol{z}}$ define the position of the plane in the z direction and j_x, j_y are the coordinates on the plane. On the other hand a state localised in the x direction to a line that passes through the point $(0, a, b)$ has $\boldsymbol{j}_0 = j_x\hat{\boldsymbol{x}} + a\hat{\boldsymbol{y}} + b\hat{\boldsymbol{z}}$.

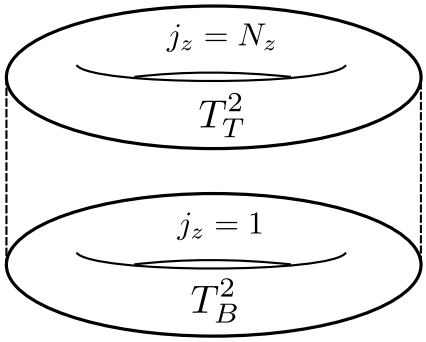

Figure 4.1: A schematic representation of the boundary of the 3D superconductor. Due to the periodic boundary conditions in the x and y directions, the top and bottom surfaces that constitute the boundary can be viewed as a pair of tori, T_T^2 located at $j_z = N_z$, and T_B^2 located at $j_z = 1$.

4.2 Open boundaries

4.2.1 2D Majorana modes

We initialise the system in the $\nu_{3D} = 1$ phase ($\mu = 3$, $t = \Delta = 1$) and break the periodic boundary condition in the z direction. The system's boundary can be viewed as a pair of toroidal surfaces T_T^2, located at $j_z = N_z$, and T_B^2, located at $j_z = 1$, as shown in Fig. 4.1. The energy spectrum of the kernel Λ acquires a set of four mid-gap states $\{|\kappa_1\rangle, |\kappa_2\rangle, |\kappa_{-1}\rangle, |\kappa_{-2}\rangle\}$ that have eigenvalues $\{E_1, E_2, -E_1, -E_2\}$ respectively. In the current configuration we have $E_1 = E_2 = 0$. The four states correspond to two spectral Dirac fermions $\tilde{\hat{a}}_i$, where $i = 1, 2$, and their PH symmetric partners. As previously asserted, these spectral Dirac fermions can be decomposed into four spectral Majorana modes $\tilde{\gamma}_{g,1}$ and $\tilde{\gamma}_{g,2}$. If we plot the spatial distribution of these four gapless Majorana modes, we find that $\tilde{\gamma}_{1,1}$ and $\tilde{\gamma}_{1,2}$ are supported on T_T^2, while $\tilde{\gamma}_{2,1}$ and $\tilde{\gamma}_{2,2}$ are supported on T_B^2. All of the Majoranas are completely delocalised in the x-y plane while being exponentially localised to their respective surfaces in the z direction.

This is succinctly expressed as

$$|\Gamma_{1,n}(\boldsymbol{j})| \propto e^{-\|\boldsymbol{\xi}\cdot(\boldsymbol{j}-\boldsymbol{j}_{0,T})\|}, \quad |\Gamma_{2,n}(\boldsymbol{j})| \propto e^{-\|\boldsymbol{\xi}\cdot(\boldsymbol{j}-\boldsymbol{j}_{0,B})\|}, \tag{4.10}$$

where $\boldsymbol{j}_{0,T} = j_x\hat{\boldsymbol{x}} + j_y\hat{\boldsymbol{y}} + \hat{\boldsymbol{z}}$, $\boldsymbol{j}_{0,B} = j_x\hat{\boldsymbol{x}} + j_y\hat{\boldsymbol{y}} + N_z\hat{\boldsymbol{z}}$, and $\boldsymbol{\xi} = (0, 0, \xi_z)$. Numerical evaluation finds that $\xi_z \approx 1.6$.

4.2.2 Effective Zeeman field

We can induce an energy splitting in the gapless states by introducing an effective Zeeman field at the boundary. The Hamiltonian (3.17) becomes

$$H' = H + H_\Omega, \quad H_\Omega = \sum_{\boldsymbol{j}} \boldsymbol{\psi}^\dagger \boldsymbol{B}\cdot\boldsymbol{\sigma}\boldsymbol{\psi}, \tag{4.11}$$

where $\boldsymbol{\psi} = \begin{pmatrix}\hat{a}_{1,\boldsymbol{j}} & \hat{a}_{2,\boldsymbol{j}}\end{pmatrix}^T$ and $\boldsymbol{B} = (B_x, B_y, B_z)$ where $\boldsymbol{B} = 0$ for $1 < j_z < N_z$. We find that $\Delta E \propto B_y$ for $0 \leq B_y < 1.5$. The other parameters B_x and B_z change the position of the Dirac cones in momentum space [115], but have no effect on the magnitude of ΔE. Due to the bulk-boundary correspondence [113] the edge states are separated from the bulk states and only a phase transition can mix them. As a consequence, we can consider how the boundary Hamiltonian H_Ω acts on the edge states alone. We can achieve that by projecting the boundary Hamiltonian onto the surface states $|\psi_i\rangle = 2\tilde{\hat{a}}_i^\dagger \bigotimes_{\boldsymbol{j}} |0_{\hat{a}_1} 0_{\hat{a}_2}\rangle$, where $\bigotimes_{\boldsymbol{j}} |0_{\hat{a}_1} 0_{\hat{a}_2}\rangle$ is the fermionic vacuum. The resulting effective Hamiltonian is given by

$$H_{\text{eff}} = \mathcal{N}\sum_{ij} \langle\psi_i|H_\Omega|\psi_j\rangle\, |\psi_i\rangle\langle\psi_j|\,, \tag{4.12}$$

where $\mathcal{N}$ is a fitting parameter that is dependent on system size. We introduce it to account for the fact that the effective Hamiltonian is a two-dimensional object derived from three-dimensional states. The eigenvalues of H_{eff}, denoted $\Delta\tilde{E}_F$, are degenerate and numerical evaluation finds that they are equal to the energy

splitting ΔE. The Zeeman field induces a position dependent, local coupling between the spatially varying (pseudo-)spin degrees of freedom. One can rewrite the H_{eff} in terms of Majorana operators and show that the effective Zeeman field couples all the various gapless Majorana modes. Given that the effective Zeeman field term is local, only zero energy Majoranas that have support on the same site will contribute to the energy splitting. Further to this, if the spatial distribution of the surface states $|\psi_i\rangle$ remains constant over the x-y plane as a function of B_y then $\Delta\tilde{E} \propto B_y$. This is consistent with our previous findings [115].

4.3 1D Majorana zero modes

4.3.1 Effective Zeeman field configuration

We now present a scheme for reducing the dimensionality of the gapless Majorana modes from two to one dimension. We modify the effective Zeeman field such that $\text{sgn}(B_y) = 1$ for $N_y/4 < j_y < 3N_y/4$ and $\text{sgn}(B_y) = -1$ elsewhere. This creates a pair of magnetic domain walls on each surface of the boundary. This configuration is depicted in Fig. 4.2 *Top*. If we initialise the system with a large magnitude Zeeman field, we find that the four mid-gap states are still present. The spatial distribution of the four gapless Majorana modes has changed. Each of the four Majoranas are still localised to the same tori as in the uniform field configuration. However, the modes on each surface are now spatially separated such that each is exponentially localised to a different single magnetic domain wall, as depicted in Fig. 4.2 *Bottom*. In terms of the previously defined notation the Majorana modes are localised as

$$\begin{aligned} |\Gamma_{1,1}(\boldsymbol{j})| &\propto e^{-\|\boldsymbol{\xi}\cdot(\boldsymbol{j}-\boldsymbol{j}_{0,\mathrm{T},1})\|}, \quad |\Gamma_{2,1}(\boldsymbol{j})| \propto e^{-\|\boldsymbol{\xi}\cdot(\boldsymbol{j}-\boldsymbol{j}_{0,\mathrm{B},2})\|}, \\ |\Gamma_{1,2}(\boldsymbol{j})| &\propto e^{-\|\boldsymbol{\xi}\cdot(\boldsymbol{j}-\boldsymbol{j}_{0,\mathrm{T},2})\|}, \quad |\Gamma_{2,2}(\boldsymbol{j})| \propto e^{-\|\boldsymbol{\xi}\cdot(\boldsymbol{j}-\boldsymbol{j}_{0,\mathrm{B},1})\|}, \end{aligned} \tag{4.13}$$

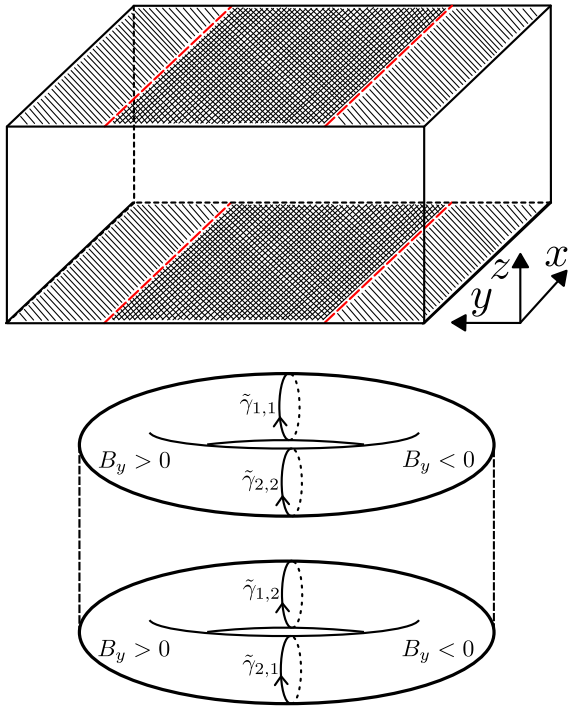

Figure 4.2: *Top* A schematic representation of the configuration of local effective Zeeman fields when localising the Majorana modes to 1D. The system is periodic in the x and y directions while having open boundaries in the z direction. A locally varying effective Zeeman field has been applied such that $\mathrm{sgn}(B_y) = 1$ for $N_y/4 \leq j_y \leq 3N_y/4$ and $\mathrm{sgn}(B_y) = -1$ elsewhere. Gapless Majorana modes appear at the interfaces between the different local effective Zeeman fields, indicated by the red dashed lines. *Bottom* The four gapless Majorana modes localised to the four interfaces between regions of differing effective Zeeman field.

where $\boldsymbol{j}_{0,\mathrm{T},1} = j_x\hat{\boldsymbol{x}} + \frac{N_y}{4}\hat{\boldsymbol{y}} + N_z\hat{\boldsymbol{z}}$, $\boldsymbol{j}_{0,\mathrm{T},2} = j_x\hat{\boldsymbol{x}} + \frac{3N_y}{4}\hat{\boldsymbol{y}} + N_z\hat{\boldsymbol{z}}$, $\boldsymbol{j}_{0,\mathrm{B},1} = j_x\hat{\boldsymbol{x}} + \frac{N_y}{4}\hat{\boldsymbol{y}} + \hat{\boldsymbol{z}}$ and $\boldsymbol{j}_{0,\mathrm{B},2} = j_x\hat{\boldsymbol{x}} + \frac{3N_y}{4}\hat{\boldsymbol{y}} + \hat{\boldsymbol{z}}$ and coherence lengths $\boldsymbol{\xi} = (0, \xi_y, \xi_z)$, with $\xi_z \approx 1.90$ and $\xi_y \approx 0.94$.

Fig. 4.3 *Top* depicts ξ_y and ΔE (computed via exact diagonalisation) as a function of $|B_y|$. The localisation parameter ξ_y was computed directly from the spatial amplitudes $|\Gamma_{g,n}(\boldsymbol{j})|$ and was found to be proportional to $|B_y|$. The energy splitting follows a linear increase which transitions into an exponential decay to

zero. The eigenvalue of the effective Hamiltonian H_{eff} is also shown in Fig. 4.3; it exactly corresponds to the energy splitting as computed via exact diagonalisation. The behavior of the energy splitting can be attributed to the gapless Majorana modes on each surface coupling in the presence of the effective Zeeman field, while simultaneously being localised by that same field. This is made plain if we plot $\omega = \Delta\tilde{E}_F/B_y$, as shown in Fig. 4.3. As the magnitude of the effective Zeeman field increases, the spatial overlap in the presence of the coupling field between the different states decreases exponentially.

4.3.2 Theoretical model

We can further reinforce this picture by theoretically modelling this behaviour. We define four ansatz wave functions $\psi_i(\boldsymbol{r})$ with $i = 1, 2, 3, 4$, trapped at four potentials of height $|B_y|$ located at $\boldsymbol{r}_0^1 = \frac{L_y}{4}\hat{\boldsymbol{y}} + L_z\hat{\boldsymbol{z}}$, $\boldsymbol{r}_0^2 = \frac{3L_y}{4}\hat{\boldsymbol{y}} + L_z\hat{\boldsymbol{z}}$, $\boldsymbol{r}_0^3 = \frac{3L_y}{4}\hat{\boldsymbol{y}} + \hat{\boldsymbol{z}}$, and $\boldsymbol{r}_0^4 = \frac{3L_y}{4}\hat{\boldsymbol{y}} + \hat{\boldsymbol{z}}$, where L_x, L_y and L_z are the system sizes in the x, y and z directions. The states can be written as

$$\psi_i^{\text{1D}}(\boldsymbol{r}) = \sqrt{\frac{\xi_y\xi_z}{2L_x\bar{Y}\bar{Z}}}e^{-\frac{\xi_y}{2}|y-y_i|}e^{-\frac{\xi_z}{2}|z-z_i|}, \tag{4.14}$$

where $\bar{Y} = (1 - e^{-\xi_y L_y})$ and $\bar{Z} = (1 - e^{-\xi_z L_z})$. If we calculate the energy shift associated with the overlap between the two states on each surface, neglecting overlaps between states on different z levels, we have

$$\Delta\tilde{E}_{\text{1D}} = 4\sum_{i\neq j}\int_0^{L_x}\int_{\frac{L_y}{4}}^{\frac{3L_y}{4}}\int_0^{l} dz\,dy\,dx \;\; \psi_i^{\text{1D}}(\boldsymbol{r})V_0\psi_j^{\text{1D}}(\boldsymbol{r}), \tag{4.15}$$

where we have periodic boundary conditions and $V_0 = |B_y|(1 - \mathrm{H}(l - z))$, where $\mathrm{H}(l - z) = \int_{-\infty}^{l-z}\delta(s)ds$ is the Heaviside function and $|B_y|$ is the strength of the potential that couples the 1D localised states. The Heaviside function is introduced as the Zeeman field is applied exclusively on the surface. The parameter l

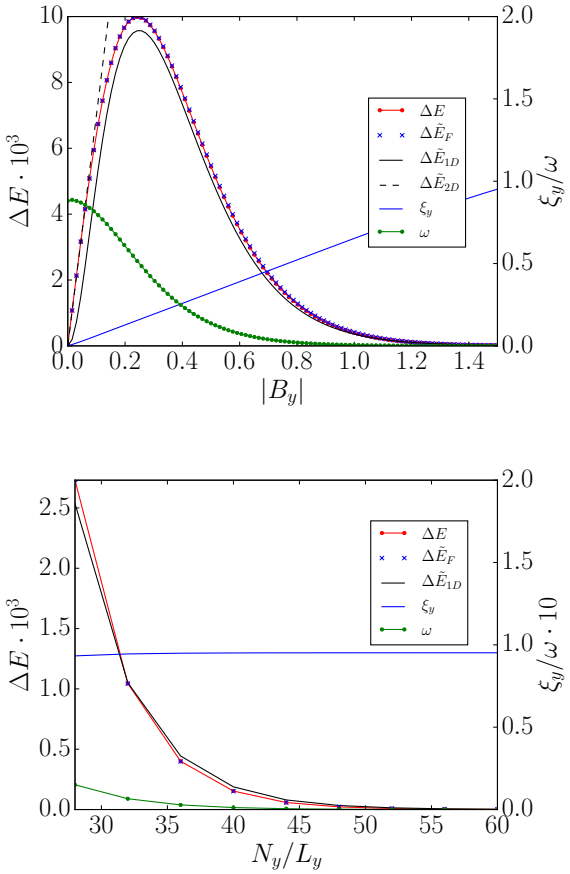

Figure 4.3: *Top* A plot of the energy splitting ΔE and the localisation in the y direction ξ_y as a function of $|B_y|$ ($25 \times 50 \times 14$, $\mu = 3$, $\Delta = t = 1$) for the 1D defect configuration. The quantity $\omega = \Delta\tilde{E}_F/B_y$ decreases exponentially as the states are progressively localised and their spatial overlap decreases. The eigenvalue of H_{eff} is shown as $\Delta\tilde{E}_F$ and corresponds exactly to ΔE. $\Delta\tilde{E}_{1\text{D}}$ and $\Delta\tilde{E}_{2\text{D}}$ correspond to the theoretical predictions for the energy splitting based on the ansatz wave functions $\psi_i^{1\text{D}}(\boldsymbol{r})$ (4.14) and $\psi_i^{2\text{D}}(\boldsymbol{r})$ (4.17). *Bottom* The energy gap ΔE and coherence length ξ_y for the system in the 1D defect configuration while varying the system size in the y direction, for $|B_y| = 1.5$. As the system size increases the size of the $\text{sgn}(B_y)$ region remains $N_y/4 < j_y < 3N_y/4$. As the overlap between the gapless modes decreases the energy gap, ΔE, decreases exponentially. The predicted energy gap, $\Delta\tilde{E}$, accurately reproduces the numerically observed values.

reflects the fact that in the continuum case the Zeeman field penetrates the bulk. We use l as a fitting parameter to map the continuum model to the discrete case. Evaluating this we find that

$$\Delta\tilde{E}_{1\mathrm{D}} = \xi_y |B_y| L_y e^{-\frac{\xi_y}{4} L_y} \big(1 - e^{-\xi_z l}\big). \tag{4.16}$$

The plot of $\Delta\tilde{E}_{1\mathrm{D}}$ as a function of $|B_y|$ is shown in Fig. 4.3 *Top*. By a numerical fit to the exact diagonalisation data we find that $l \approx L_y^{-1}$. In the region $|B_y| > 0.2$ of Fig. 4.3, there is a strong agreement between the behaviour of the numerical observations and the modelling of the states by 4.14. We note that the value of ξ_y is derived from the numerical data of the state amplitudes only on the boundary. Similarly, the value of ξ_z is taken to be an average over the surface. A more careful analysis would require $\xi_y = \xi_y(z)$ and $\xi_z = \xi_z(y)$, which might explain the slight deviation between the numerical and the predicted values of ΔE. By averaging over the relevant spatial variables we find a good match for the overall behaviour of the surface physics. We also apply this formula for varying L_y, as shown in Fig. 4.3 *Bottom*. In the region $|B_y| < 0.2$, the states are transitioning between their extended 2D form and an exponentially localised 1D form. For small values of $|B_y|$, the states are closer to the form

$$\psi_i^{2\mathrm{D}}(\boldsymbol{r}) = \sqrt{\frac{\xi_z}{L_x L_y \bar{Z}}} e^{-\frac{\xi_z}{2}|z - z_i|}. \tag{4.17}$$

The overlap of two of these states on the same surface in the presence of the potential $V_0 = |B_y|(1 - \mathrm{H}(l - z))$ is given by

$$\Delta\tilde{E}_{2\mathrm{D}} = |B_y| \big(1 - e^{-\xi_z l}\big). \tag{4.18}$$

The behaviour of this model is shown in Fig. 4.3, where we have again taken $l \approx L_y^{-1}$. The initial linear increase in ΔE is accurately reproduced by assuming that the states are spread evenly throughout the 2D surface, as modelled by (4.17).

4.3.3 1D reciprocal space

To determine the discretion relation of the 1D Majorana modes, we Fourier transform the Hamiltonian in the x direction, giving

$$H' = \sum_{p_x} \Psi^\dagger_{p_x} \Lambda(p_x) \Psi_{p_x}, \tag{4.19}$$

where $\Psi_{p_x} = \bigoplus_{\bar{\boldsymbol{j}}} \left(\hat{a}_{1,\bar{\boldsymbol{j}},p_x}, \quad \hat{a}^\dagger_{1,\bar{\boldsymbol{j}},p_x}, \quad \hat{a}_{1,\bar{\boldsymbol{j}},p_x}, \quad \hat{a}^\dagger_{1,\bar{\boldsymbol{j}},p_x} \right)^T$ with $\bar{\boldsymbol{j}} = \begin{pmatrix} j_y, & j_z \end{pmatrix}$ and $p_x \in [-\pi, \pi)$. The energy dispersion as a function of p_x is shown in Fig. 4.4. The spectrum is PH symmetric and the bulk negative energy states are separated from the bulk excited states by a bulk energy gap. There is a set of eigenvalues that cross zero energy at $p_x = 0$. Because, the mapping that takes us to the spectral Majorana modes is unitary, the crossing states correspond to the four gapless Majorana modes $\tilde{\gamma}_{g,n}$ now given by $\tilde{\gamma}_{g,n,p_x}$. In reciprocal space, the Majorana modes no longer obey the reality condition and we have $\tilde{\gamma}_{g,n,p_x} = \tilde{\gamma}^\dagger_{g,n,-p_x}$. This implies that the spectrum for $p_x > 0$ is an inverted copy of $p_x < 0$. Furthermore, the eigenvalue of $\tilde{\gamma}_{1,n,p_x}$ is equal in magnitude to the eigenvalue of $\tilde{\gamma}_{2,n,p_x}$ but with opposite sign. This leads us to conclude that $\tilde{\gamma}_{1,1}$ and $\tilde{\gamma}_{1,2}$ propagate in the same direction, but in the opposite direction to $\tilde{\gamma}_{2,1}$ and $\tilde{\gamma}_{2,2}$, as shown in Fig. 4.2 *Bottom*.

4.3.4 Fractional Chern numbers and edge states

The behavior of the surface states in the presence of magnetic domain walls is commensurate with our understanding of chiral 2D TS. Given a pair of 2D class D topological superconductors on a torus, the number of gapless Majorana states at the interface is equal to the difference of their Chern numbers, as given in (4.1) [114]. This configuration is shown in Fig. 4.5 *Top*. In the presence of a uniform non-zero effective Zeeman field the union of the top and bottom surfaces of the 3D

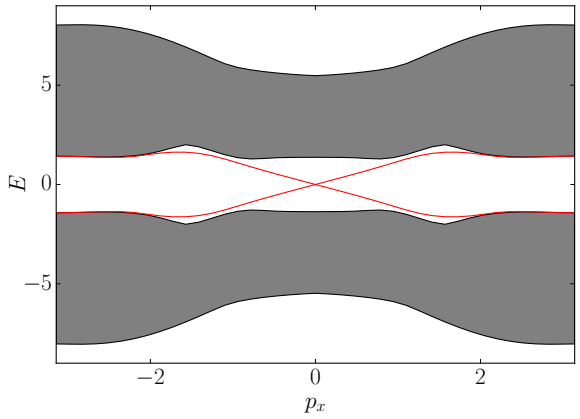

Figure 4.4: The energy dispersion of the system in the 1D defect configuration ($N_y = 50$, $N_z = 14$, $\mu = 3$, $\Delta = t = 1$), having Fourier transformed the system in the x direction. The system supports two pairs of degenerate counter propagating gapless Majorana modes indicated in red, each localised at a different defect line. The grey regions contain the bulk bands, not explicitly shown here.

DIII model can be considered to be a 2D class D TS [115]. The sign of the partial contribution to the Chern number of each boundary surface is equal to the sign of B_y at that surface. When the magnetic domain walls are introduced we can effectively view each magnetic domain as one-half of a 2D class D superconductor in its own right. The systems either side of a domain wall have partial Chern numbers of opposite sign, as shown in Fig. 4.5 *Bottom*. We find that the number of Majorana modes at each interface is equal to the difference in the partial Chern numbers in each magnetic domain on a surface. This suggests the relation

$$N = |\nu_{b,+} - \nu_{b,-}|, \tag{4.20}$$

where $\nu_{b,\pm}$ are the partial Chern numbers either side of a magnetic domain wall.

We can demonstrate the validity of 4.20 by starting from relation 4.1 that gives the number of edge states between surfaces with integer Chern numbers. It is known that the Chern number of a composite system of two non-interacting

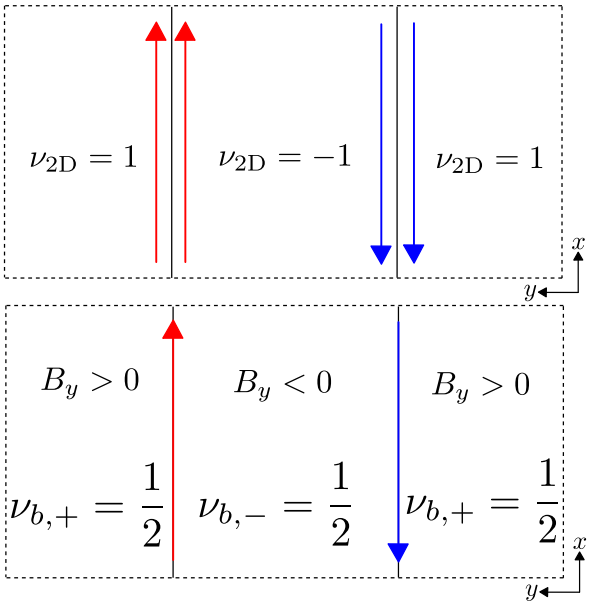

Figure 4.5: *Top* A schematic representation of a pair of 2D class D TS on a torus. The dashed lines indicate a periodic boundary. The Chern numbers of the systems differ by a sign. Such chiral superconductors possess a pair of chiral counter-propagating Majorana modes at their boundaries. The orientation of the modes is defined up to a sign in the Chern number. *Bottom* A schematic representation of a single surface of our 3D DIII system. The two magnetic domain walls trap one Majorana fermion each. The number of Majorana modes is the difference of the partial Chern numbers in each magnetic domain.

2D subsystems is equal to the sum of the Chern numbers of the two subsystems. This property holds true even if one of the Chern numbers is half integer, e.g. when one of the subsystems is the 2D boundary of a 3D system. Consider now two neighbouring TS with bulk invariants ν_+ and ν_- with $N = |\nu_+ - \nu_-|$ gapless states at their interface. We superpose to them a gapped 2D surface of a 3D system that has Chern number $\nu_b = 1/2$. This surface supports no edge modes hence it will not change the total number N of edge states. But it will modify the total Chern number at either side of the interface to become half-integer, giving eventually 4.20.

It is also possible to show the consistency of this new relationship with the original index theorem. The Chern number of the whole boundary of a system is defined as $\nu_{2\mathrm{D}} = \sum_b \nu_b$. Take two copies of the 3D bulk system with Zeeman field of opposite sign. One of the systems has a boundary with Chern number $\nu_{2\mathrm{D},+} = \sum_b \nu_{b,+}$ while the other has a boundary with Chern number $\nu_{2\mathrm{D},-} = \sum_b \nu_{b,-}$. We now glue them together such that we have periodic boundary conditions in the x and y directions with the 1D defect configuration on the boundary of the composite system, as described previously. The index theorem (4.1) relates the Chern numbers of the boundaries of both systems (the union of the top and bottom surfaces of each) to the number of states that appear at their interface. In the case when $\nu_{3\mathrm{D}} = 1$ (4.1) tells us there should be two states at the interface. We can rewrite (4.1) in the following way

$$\begin{aligned} N &= |\nu_{2\mathrm{D},+} - \nu_{2\mathrm{D},-}| \\ &= |\nu_{T,+} + \nu_{B,+} - \nu_{T,-} - \nu_{B,-}| \\ &= |\nu_{T,+} - \nu_{T,-}| + |\nu_{B,+} - \nu_{B,-}| \\ &= N_T + N_B. \end{aligned} \tag{4.21}$$

where $N_b = 1$. The decomposition in the second step is allowed because the quantities $\nu_{b,+} - \nu_{b,-}$ have the same sign. The original index theorem is preserved as the total number of states at the interface between the two boundary systems is 2.

4.3.5 The $\nu_{\mathbf{3D}} = 2$ model

To demonstrate the generality of our results, we now consider the defects at the boundary of a $\nu_{3\mathrm{D}} = 2$ TS. We consider the tight binding Hamiltonian H_2

$$\begin{aligned}\hat{H}_2 = \sum_{\boldsymbol{j}} \Bigg\{ \sum_{k=1,2} \Big[&\mu \hat{a}^\dagger_{k,\boldsymbol{j}} \hat{a}_{k,\boldsymbol{j}} + \frac{1}{2} + t\hat{a}^\dagger_{k,\boldsymbol{j}} \hat{a}_{k,\boldsymbol{j}-\hat{\boldsymbol{x}}} + t\hat{a}^\dagger_{k,\boldsymbol{j}} \hat{a}_{k,\boldsymbol{j}-\hat{\boldsymbol{x}}+\hat{\boldsymbol{z}}} \\ &- \Delta \hat{a}_{k,\boldsymbol{j}} \hat{a}_{k,\boldsymbol{j}+\hat{\boldsymbol{x}}} + \Delta \hat{a}_{k,\boldsymbol{j}} \hat{a}_{k,\boldsymbol{j}-\hat{\boldsymbol{x}}+\hat{\boldsymbol{z}}} \Big] - 2i\Delta\big(\hat{a}_{1,\boldsymbol{j}} \hat{a}_{2,\boldsymbol{j}+\hat{\boldsymbol{y}}} + \hat{a}_{2,\boldsymbol{j}} \hat{a}_{1,\boldsymbol{j}+\hat{\boldsymbol{y}}}\big) \\ &+ 2i\Delta\big(\hat{a}_{1,\boldsymbol{j}} \hat{a}_{1,\boldsymbol{j}+\hat{\boldsymbol{x}}+\hat{\boldsymbol{y}}} - \hat{a}_{2,\boldsymbol{j}} \hat{a}_{2,\boldsymbol{j}+\hat{\boldsymbol{x}}+\hat{\boldsymbol{y}}}\big) + H.c. \Bigg\}. \end{aligned} \tag{4.22}$$

When in the $\nu_{3\mathrm{D}} = 2$ phase ($\mu = \Delta = t = 1$) and with open boundary conditions in the z directions, the model supports two helical Majorana cones per surface. When gapped by a uniform positive effective Zeeman field, each surface contributes $\nu_{\mathrm{T}} = \nu_{\mathrm{B}} = 1$ to the total Chern number of the boundary system such that $\nu_{2\mathrm{D}} = 2$. In the language of the previous section, it supports eight mid-gap states $\{|\kappa_n\rangle, |\kappa_{-n}\rangle\}$, $n = 1, 2, 3, 4$. This corresponds to eight gapless Majorana modes $\tilde{\gamma}_{g,n}$, $g = 1, 2$. A plot of $|\Gamma_{g,n}(\boldsymbol{j})|$ finds that the states are localised as

$$\begin{aligned} |\Gamma_{1,1}(\boldsymbol{j})| &\propto e^{-\|\boldsymbol{\xi}\cdot(\boldsymbol{j}-\boldsymbol{j}_{0,\mathrm{T},1})\|}, \quad |\Gamma_{2,1}(\boldsymbol{j})| \propto e^{-\|\boldsymbol{\xi}\cdot(\boldsymbol{j}-\boldsymbol{j}_{0,\mathrm{B},2})\|}, \\ |\Gamma_{1,2}(\boldsymbol{j})| &\propto e^{-\|\boldsymbol{\xi}\cdot(\boldsymbol{j}-\boldsymbol{j}_{0,\mathrm{T},2})\|}, \quad |\Gamma_{2,2}(\boldsymbol{j})| \propto e^{-\|\boldsymbol{\xi}\cdot(\boldsymbol{j}-\boldsymbol{j}_{0,\mathrm{B},1})\|}, \\ |\Gamma_{1,3}(\boldsymbol{j})| &\propto e^{-\|\boldsymbol{\xi}\cdot(\boldsymbol{j}-\boldsymbol{j}_{0,\mathrm{T},1})\|}, \quad |\Gamma_{2,3}(\boldsymbol{j})| \propto e^{-\|\boldsymbol{\xi}\cdot(\boldsymbol{j}-\boldsymbol{j}_{0,\mathrm{B},2})\|}, \\ |\Gamma_{1,4}(\boldsymbol{j})| &\propto e^{-\|\boldsymbol{\xi}\cdot(\boldsymbol{j}-\boldsymbol{j}_{0,\mathrm{T},2})\|}, \quad |\Gamma_{2,4}(\boldsymbol{j})| \propto e^{-\|\boldsymbol{\xi}\cdot(\boldsymbol{j}-\boldsymbol{j}_{0,\mathrm{B},1})\|}, \end{aligned} \tag{4.23}$$

where $\boldsymbol{\xi} = (0, \xi_y, \xi_z)$, with $\xi_z = 1.90$ and $\xi_y = 0.94$. Each magnetic domain wall supports two gapless Majorana modes. The difference in the partial Chern numbers either side of a magnetic domain wall is equal to the number of states localised to it; this is commensurate with (4.20).

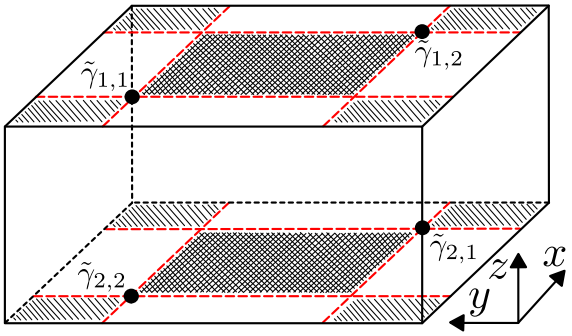

Figure 4.6: A schematic representation of the configuration of local effective Zeeman fields when localising the Majorana modes to 0D. The system is periodic in the x and y directions while having open boundaries in the z direction. The black dots indicate the points at which the Majorana modes are localised. In the central darker regions $\mathrm{sgn}(B_y) = -1$, the lighter corner regions have $\mathrm{sgn}(B_y) = 1$ and the white regions have $B_y = 0$.

4.4 Quasi-0D Majorana modes

We now consider the next iteration of nested defects where we reduce their dimensionality from 1D to 0D and study the arrangement of the surface Majorana modes in this new configuration. Taking the $\nu_{3\mathrm{D}} = 0, \pm 1$ model with Hamiltonian (3.17), to produce the defects we divide the boundary surfaces into nine domains where the magnitude of the effective Zeeman field is either zero or $\pm B_y$, as shown in Fig. 4.6. Numerical evaluation finds that the four mid-gap states $\{|\kappa_n\rangle, |\kappa_{-n}\rangle\}$, $n = 1, 2$, are still present. Calculation of the amplitudes of the four associated gapless Majorana modes finds that they are localised at the following points

$$\begin{aligned}
\tilde{\gamma}_{1,1}: &\quad \boldsymbol{j}_{0,T,a} = \frac{N_x}{4}\hat{\boldsymbol{x}} + \frac{N_y}{4}\hat{\boldsymbol{y}} + N_z\hat{\boldsymbol{z}}, \\
\tilde{\gamma}_{1,2}: &\quad \boldsymbol{j}_{0,T,b} = \frac{3N_x}{4}\hat{\boldsymbol{x}} + \frac{3N_y}{4}\hat{\boldsymbol{y}} + N_z\hat{\boldsymbol{z}}, \\
\tilde{\gamma}_{2,1}: &\quad \boldsymbol{j}_{0,B,a} = \frac{N_x}{4}\hat{\boldsymbol{x}} + \frac{N_y}{4}\hat{\boldsymbol{y}} + \hat{\boldsymbol{z}}, \\
\tilde{\gamma}_{2,2}: &\quad \boldsymbol{j}_{0,B,b} = \frac{3N_x}{4}\hat{\boldsymbol{x}} + \frac{3N_y}{4}\hat{\boldsymbol{y}} + \hat{\boldsymbol{z}}.
\end{aligned} \tag{4.24}$$

We expect that the Majorana modes should be exponentially localised to their respective points in regions of non-zero effective Zeeman field, as in the 1D case. In the regions of zero effective Zeeman field there is no suppressing field and as such we expect a less stringent form of localisation. Numerical evaluation of the amplitudes $|\Gamma_{g,n}|$ finds that they are not rotationally symmetric about their respective points. As expected, they are exponentially localised in the regions of non-zero effective Zeeman field and polynomially localised in the regions with zero effective Zeeman field. Due to the polynomial nature of the localisation into the regions of zero effective Zeeman fields, we say that the Majorana modes are quasi-0D. A plot of $|\Gamma_{1,1}|$ is shown in Fig. 4.8.

Assuming that $N_x = N_y$, we introduce the localisation parameter ξ_{xy} that refers to the exponential decay coefficient corresponding to the decay of the gapless Majorana modes along the straight line that passes through both quasi-0D Majoranas on a surface, which are shown in Fig. 4.6. Fig. 4.7 *Top* shows the energy gap ΔE and ξ_{xy} for varying $|B_y|$. We have presented data from systems of various sizes. As $|B_y|$ increases, we identify in Fig. 4.7 *Top* two distinct behaviors. For small $|B_y|$ we see ΔE increasing in a similar manner to the 1D case studied in Sec. 4.3. The states are transitioning between their 2D delocalised form to their quasi-0D form. This initial linear increase is commensurate with the gap induced by the effective Zeeman field on some 2D surface states, as previously discussed. For larger $|B_y|$ the energy gap exponentially decays to some constant value that depends on the system size. Fig. 4.8 *Top* shows the value of ΔE for varying system size, with $|B_y| = 1.5$. A numerical fit finds that $\Delta E \propto N_{xy}^{-2}$, and so for sufficiently large system sizes $\Delta E \to 0$. Using this behaviour to extrapolate Fig. 4.7, we deduce that for a sufficiently large system size and sufficiently large effective Zeeman field we have quasi-0D *zero energy* states bound at the point-like defects.

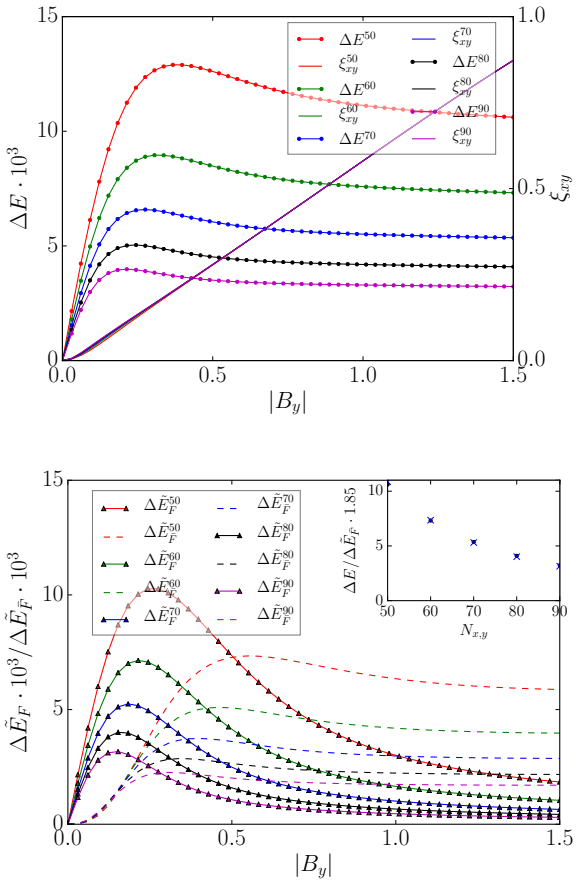

Figure 4.7: *Top* The energy splitting ΔE and localisation parameter ξ_{xy} as a function of $|B_y|$, for the chessboard configuration of effective Zeeman fields. Shown is data from systems of sizes $N_x = N_y = 50$, $N_x = N_y = 60$, $N_x = N_y = 70$, $N_x = N_y = 80$, and $N_x = N_y = 90$. *Bottom* The eigenvalues of the effective Hamiltonian H_{eff}, $\Delta\tilde{E}_F$, and the corrective effective Hamiltonian $\bar{H}_{\text{eff}}$, $\Delta\tilde{E}_{\bar{F}}$. (Inset) The values of ΔE (black dots) and $\Delta\tilde{E}_{\bar{F}}$ (blue crosses) for $|B_y| = 1.5$ for different system sizes. When $\Delta\tilde{E}_{\bar{F}}$ is multiplied by a factor of 1.85 the two quantities are the same at all system sizes.

An effective description of the surface system is two fold. The parts of the surface that experience a non-zero Zeeman field are described by the effective Hamiltonian H_{eff}, as in the 1D case. Its eigenvalues $\Delta\tilde{E}_F$ as a function of $|B_y|$ are shown in Fig. 4.7 *Bottom*. For small values of $|B_y|$, H_{eff} accurately reproduces the

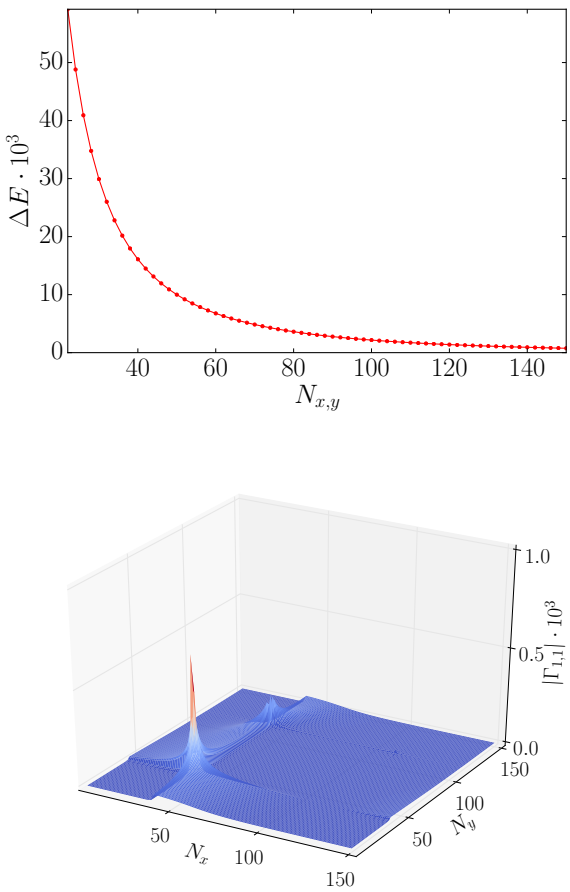

Figure 4.8: *Top* The energy splitting ΔE for chessboard configuration of boundary fields for $|B_y| = 1.5$ for varying system size in the x and y directions, such that $N_x = N_y$. A numerical fit of the curve finds that $\Delta E \propto N_{x,y}^{-2}$ and will decay to zero in the thermodynamic limit. *Bottom* The amplitude of $\tilde{\gamma}_{1,1}$ over the x-y plane at $z = N_z$.

numerically evaluated energy gap ΔE. For larger values of $|B_y|$, $\Delta\tilde{E}_F$ diverges from ΔE decaying too quickly as $|B_y|$ increases. As the magnitude of the Zeeman field becomes large the regions of the surface that experience no Zeeman field still support a significant proportion of the state. Despite the fact that they do not experience the coupling of their local degrees of freedom via the Zeeman field they still provide a contribution the energy gap. This contribution arises due to the

surface states being significantly modified by the nested defects so that they are no longer zero eigenstates of the bulk Hamiltonian, H. This extra contribution can be seen by defining a second effective Hamiltonian

$$\bar{H}_{\text{eff}} = \sum_{\alpha\beta} \langle\psi_\alpha|H|\psi_\beta\rangle \, |\psi_\alpha\rangle \, \langle\psi_\beta| \, . \tag{4.25}$$

The eigenvalues of $\bar{H}_{\text{eff}}$ are degenerate and denoted $\Delta\tilde{E}_{\bar{F}}$. Fig. 4.7 shows $\Delta\tilde{E}_{\bar{F}}$ as a function of $|B_y|$. For small values of $|B_y|$, $\Delta\tilde{E}_{\bar{F}}$ is small and does not make a significant contribution to ΔE. As $|B_y|$ becomes large $\Delta\tilde{E}_{\bar{F}}$ converges to a constant value dependent on system size. It is this contribution which accounts for the behaviour of ΔE for large values of $|B_y|$. This can be seen in Fig. 4.7 *Bottom* (Inset). The values of ΔE and $\Delta\tilde{E}_{\bar{F}}$ for $|B_y| = 1.5$ are the same up to a constant factor of 1.85.

This field configuration traps gapless Majorana modes at 0D points that are at the interface between regions of the surface that have partial Chern numbers $\nu_b = \pm\frac{1}{2}$. As in the 1D case, the number of Majorana modes at each point is the difference of the partial Chern numbers either side of the interface. Where there are interfaces between regions of non-zero Zeeman field and regions that experience no Zeeman field, no well localised Majorana modes appear. We suspect that this is because (4.20) is not well defined for gapless regions. An examination of this field configuration implemented in the $\nu = 2$ model given in (4.22) finds that we simply double the number of gapless Majorana modes at the four points given in (4.24).

4.5 Conclusions

In this chapter we have investigated the response of helical Majorana modes at the boundary of a 3D TS in the symmetry class DIII in the presence of nested defects. Gapless Majorana modes become localised at these defects, allowing states

of dimension 2, 1 and quasi-0 to appear at the boundary of the system depending on the effective Zeeman field configuration. Furthermore, we observed a generalisation of the index theorem (4.1) whereby the number of gapless Majorana modes trapped at a given magnetic domain wall is the difference in the possibly partial Chern numbers either side of a wall, as defined in (3.27). This relation holds in the case of edge states localised at both 1D and 0D domain walls.

We suggest two possible implementations of such an effective Zeeman field. First, in recent years much work has been done on implementing effective Zeeman fields through doping materials with polarised magnetic impurities [116, 117, 118, 119, 120, 121, 122, 123, 124, 125, 126, 127, 128, 129, 130, 131, 132, 133]. Through judicious doping of sections of the surface of the superconductor, such that magnetic domain walls are created in place of the defect lines in our model, we can induce an effective Zeeman field coupling between the different pseudo-spin components of our model. Second, we could construct a superconductor to magnetic material heterostructure. By depositing a layer of ferromagnetic material on the surface of the superconductor, we can induce a spin-orbit coupling in the surface of the superconductor [134, 135, 113]. If a magnetic domain wall is created in the magnetic material, this would correspond to a change in the sign of the effective spin-orbit coupling, as needed of the implementation of nested defects.

Chapter 5

Summary and Outlook

Throughout the course of this PhD I have looked at a wide variety of models of topological condensed matter systems. There exists a staggering diversity in both the types of system that fall under this umbrella and the variety of different means of analysing them.

My study of the decomposition of the Chern number [90] of four component systems presents a means of measuring this topological index in such systems. The method is quite general in its theoretical formulation, from the perspective of what kind of system it is applicable to. However, there are still questions to answer about the generalisation of this method to an arbitrary number of components. As stated, the generalised Schmidt decomposition, upon which such an extension could be based, is complex.

Attempts to find topologically non-trivial models for superconductivity in three spatial dimensions were successful [115]. Through a random numerical search we managed to discover four distinct models in the symmetry class DIII that support a wide variety of winding numbers. Each of these modes support helical Majorana edge modes. In the presence of an effective Zeeman field, these

states become energetically gapped and form a 2D topological superconductor in the class D. A bulk-boundary correspondence was observed between the boundary system's Chern number and the bulk system's winding number. Furthermore, by adding spatial variations to the effective Zeeman field on the boundary, we reduced the dimensionality of the zero energy Majorana modes from 2D to 1D and quasi-0D.

This method of numerical search for new and interesting models was quite successful. However, it is difficult to see how the resultant models might be realisable outside of some very advanced systems of cold atoms. In the coming months I intend to develop this numerical search method in the hopes of discovering new *physically realisable* models of topological superconductivity. As was discussed, we arrived at the new models by defining the most general Hamiltonian for the symmetry class DIII for a given finite range of interactions. By randomly selecting a point in parameter space and computing the topological index, we eventually arrived at a non-trivial model. The only restriction we had was that the Hamiltonian should be TR and PH symmetric symmetric. In effect, this constraint projects us into a subspace of the overall model space. However within this subspace is contained the multitude of different microscopic realisations of 3D DIII models. Of this subset of models only a small number are practically realisable or in any way related to real materials. The question is then, 'is there a way of imposing a larger number of constraints on the Hamiltonian such that the model we arrive at obeys an arbitrarily large number of constraints?'

One of the variety of metaheuristic methods can be applied to the search for and characterisation of new analytically tractable and *physically implementable* models. Indeed, with judicious construction of such algorithms, the structural

characteristics of the resultant models can be decided *a priori*. As an example, consider the following problem. I wish to find a 3D tight-binding model that has

- A given point group.
- A given number of species of fermion.
- A given symmetry class.
- A fixed maximum coupling length.
- A bulk gap of a certain size.
- A bulk topological invariant of a given value.

We call this the *target* Hamiltonian $H_T(\boldsymbol{\lambda}_T)$, where $\boldsymbol{\lambda}_T = (\lambda_{T,1}, ..., \lambda_{T,m})$ parametrises the couplings. One can write down a general Hamiltonian $H(\boldsymbol{\lambda})$ that contains all possible couplings parametrised by $\boldsymbol{\lambda} = (\lambda_1, ..., \lambda_n)$, where $m \leq n$, within the bounds of these criteria. Assuming the criteria we have defined are not too stringent, within this general model lies the precise example we are looking for. What we desire is an algorithm that performs the following operation

$$H(\boldsymbol{\lambda}) \rightarrow H_T(\boldsymbol{\lambda}_T) \tag{5.1}$$

More precisely, we desire a means of finding $\boldsymbol{\lambda}_T$ and the relationships between $\lambda_{T,i}$.

If we decide to use a MC algorithm to do our optimisation. Therefore, we define a cost function that preferentially weights our search to the desired characteristics. For example, we require that the couplings are preferentially constrained to adhere to the given point group. One of the primary problems with this method is the fact that it is not possible to define a local gradient in the topological invariant. By their very nature they are invariant to small changes in the values

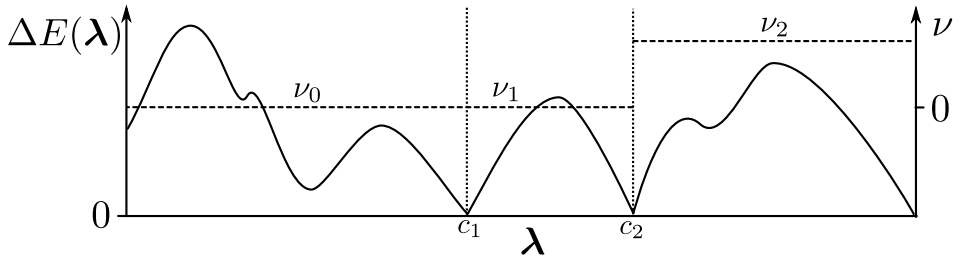

Figure 5.1: An abstract representation of the phase diagram of a general Hamiltonian $H(\boldsymbol{\lambda})$ with an energy gap $\Delta E(\boldsymbol{\lambda})$ and bulk topological invariant ν. The points $c_{1,2}$ are the critical points at which the Hamiltonian is gapless. Each gapped phase has an associated value of the invariant $\nu_{0,1,2}$. In this instance $\nu_0 = \nu_1 = 0$.

of the couplings. Only a closure of the bulk gap can result in a change in the invariant. However what can be found easily are critical points. The boundary between different topological phases lies at the points in phase space where the bulk gap closes. As such, we can include a term in the cost function that leads the search to these critical points. In the case shown in the Fig. 5.1 there are two critical points c_1 and c_2 that separate different phases. The most desirable outcome of any search is finding the critical point c_2 that lies at the boundary of a topologically non-trivial phase. The challenge is to develop an algorithm that preferentially finds c_2 over c_1.

There are many possible avenues of study for potentially resolving this problem.

- The 'brute force' method.
  - Involves simply performing a simulated annealing MC search repeatedly until the desired critical point is found.
  - This approach would be viable if performed using GPU parallelisation.
- Parallel tempering.

  - Using some sort of modified parallel tempering algorithm.

- Evolutionary algorithm.
  - Implementation of some kind of evolutionary algorithm, either for the whole search procedure or as a tertiary process once a set of critical points have been found.

Such a means of constructing new topological models is generic. As such most systems that can be written down in tight-binding form can be subject to these kinds of optimisation procedures. This might apply to TS, topological insulators, Weyl semi-metals, and more. Furthermore, the ability to generate models of arbitrary symmetry class with specific properties presents a number of potential avenues of study. Such availability of new models would facilitate the study of

- The nature of topological phase transitions between symmetry classes.
- The behavior of heterostructures of various new combinations of topological systems.
- What kinds of superconducting pairing gives rise to different kinds of topological phase.

Appendix A

Representation Transformations

There exist a set of transformations depicted in Fig. A.1 that map between different basis representations of

$$H = \sum_{k,k',\boldsymbol{j},\boldsymbol{j}'} \hat{a}_{k,\boldsymbol{j}} \Lambda_{k,\boldsymbol{j}}^{k',\boldsymbol{j}'} \hat{a}_{k',\boldsymbol{j}'} = \Psi^\dagger \Lambda \Psi \tag{A.1}$$

There are four distinct representations that are all related by a set of unitary rotations $\left\{U_\gamma, V, \tilde{U}_\gamma\right\}$. The four representations are as follows

- Ψ: constituent Dirac fermions, $a_{k,\boldsymbol{j}}$.
- Ψ_γ: constituent Majorana modes, $\gamma_{g,\boldsymbol{j}}$.
- $\tilde{\Psi}$: spectral Dirac fermions, $\tilde{a}_n$.
- $\tilde{\Psi}_\gamma$: spectral Majorana modes, $\tilde{\gamma}_{g,n}$.

If we start with the H in the constituent fermion basis as given in (4.3) we can rewrite Λ as its singular value decomposition $\Lambda = VDV^\dagger$, where V is a unitary matrix who's columns are the eigenvectors of Λ and D is a diagonal matrix containing the eigenvalues of Λ

$$\begin{aligned} V &= \left(\left|\kappa_n\right\rangle, \left|\kappa_{-n}\right\rangle, \quad \ldots, \quad \left|\kappa_1\right\rangle, \quad \left|\kappa_{-1}\right\rangle\right), \\ \mathrm{diag}(D) &= \left(E_n, E_{-n} \quad \ldots, \quad E_1, \quad E_{-1}\right). \end{aligned} \tag{A.2}$$

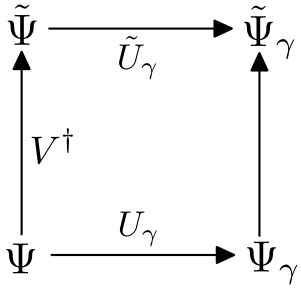

Figure A.1: A diagram showing the set of transformations that map between the different fermion pictures. Ψ are the constituent Dirac fermions, Ψ_γ are the constituent Majorana modes, $\tilde{\Psi}$ are the spectral Dirac fermions and Ψ_γ are the spectral Majorana modes. V is the unitary matrix found via the singular value decomposition of Λ.

By contracting V with the spinor Ψ we put the Hamiltonian in the form $H = \tilde{\Psi}^\dagger D\tilde{\Psi}$ where $\tilde{\Psi} = V^\dagger\Psi$. The elements of $\tilde{\Psi}$ are the spectral Dirac fermionic operators that diagonalise the Hamiltonian, such that $H = \sum_n E_n \tilde{a}_n^\dagger \tilde{a}_n$, and each spectral Dirac fermion operator can be written as a sum of the constituent Dirac fermion operators

$$\begin{aligned}\tilde{a}_n = \langle\kappa_n|\,\Psi &= \sum_{\boldsymbol{j}k} \left(\alpha^{\kappa_i}_{\boldsymbol{j}k\bullet}\right)^* a_{k,\boldsymbol{j}} + \left(\alpha^{\kappa_i}_{\boldsymbol{j}k\circ}\right)^* a^\dagger_{k,\boldsymbol{j}},\\ \tilde{a}_{-n} = \langle\kappa_{-n}|\,\Psi &= \sum_{\boldsymbol{j}k} \alpha^{\kappa_i}_{\boldsymbol{j}k\circ} a_{k,\boldsymbol{j}} + \alpha^{\kappa_i}_{\boldsymbol{j}k\bullet} a^\dagger_{k,\boldsymbol{j}}.\end{aligned} \tag{A.3}$$

where $\alpha^{\kappa_i}_{\boldsymbol{j}k\rho}$ come from the relevant eigenstates $|\kappa_i\rangle$ and we note that $\tilde{a}_n^\dagger = \tilde{a}_{-n}$. These spectral Dirac fermion operators can act on a fermionic Fock vacuum $|\varnothing\rangle = \bigotimes_{\boldsymbol{j}} |0_{a_1} 0_{a_2}\rangle$, such that

$$|\psi_i\rangle = 2\tilde{a}_i^\dagger\,|\varnothing\rangle = 2\sum_{\boldsymbol{j},k} \alpha^{\kappa_i}_{\boldsymbol{j}k\bullet} a^\dagger_{k,\boldsymbol{j}}\,|\varnothing\rangle\,, \tag{A.4}$$

where the factor of 2 renormalises the state. $|\psi_i\rangle$ are the eigenstates of H in the Fock representation.

Another useful representation is the Majorana fermion basis. Via the unitary

matrix

$$U_\gamma = \bigoplus_{\boldsymbol{j}} \frac{1}{\sqrt{2}} \begin{pmatrix} 1 & 1 & 0 & 0 \\ -i & i & 0 & 0 \\ 0 & 0 & 1 & 1 \\ 0 & 0 & -i & i \end{pmatrix}, \tag{A.5}$$

we can rotate the Hamiltonian into a new basis $H = \Psi^\dagger U_\gamma^\dagger U_\gamma \Lambda U_\gamma^\dagger U_\gamma \Psi = \Psi_\gamma^\dagger \Lambda_\gamma \Psi_\gamma$. The elements of Ψ_γ are the constituent Majorana fermion operators $\gamma_{g,\boldsymbol{j}}$, given by

$$\begin{aligned} \gamma_{1,\boldsymbol{j}} &= \frac{a_{1,\boldsymbol{j}} + a_{1,\boldsymbol{j}}^\dagger}{2}, & \gamma_{2,\boldsymbol{j}} &= \frac{a_{1,\boldsymbol{j}} - a_{1,\boldsymbol{j}}^\dagger}{2i}, \\ \gamma_{3,\boldsymbol{j}} &= \frac{a_{2,\boldsymbol{j}} + a_{2,\boldsymbol{j}}^\dagger}{2}, & \gamma_{4,\boldsymbol{j}} &= \frac{a_{2,\boldsymbol{j}} - a_{2,\boldsymbol{j}}^\dagger}{2i}. \end{aligned} \tag{A.6}$$

The eigenstates of Λ_γ are

$$|\kappa_n\rangle_\gamma = \sum_{\boldsymbol{j}} \sum_{g=1}^{4} \beta_{\boldsymbol{j}g} \, |\boldsymbol{j}\rangle \otimes |g\rangle \, . \tag{A.7}$$

The final corner of the diagram in Fig. A.1 corresponds to the spectral Majorana fermion basis. It is related to the spectral Dirac fermion basis via the unitary rotation $\tilde{U}_\gamma$, given by

$$\tilde{U}_\gamma = \mathbb{I}_{\dim(\Lambda)/2} \otimes \begin{pmatrix} 1 & 1 \\ -i & i \end{pmatrix}, \tag{A.8}$$

where $\mathbb{I}_{\dim(\Lambda)/2}$ is the $\dim(\Lambda)/2$ dimensional identity matrix. The elements of the spinor $\tilde{\Psi}_\gamma = \tilde{U}_\gamma \tilde{\Psi}$ are the spectral Majorana fermion operators $\tilde{\gamma}_{\tilde{g},n}$, where $\tilde{g} = 1, 2$, such that

$$\tilde{\gamma}_{1,n} = \frac{\tilde{a}_n + \tilde{a}_n^\dagger}{2}, \quad \tilde{\gamma}_{2,n} = \frac{\tilde{a}_n - \tilde{a}_n^\dagger}{2i}, \tag{A.9}$$

where each gapless Majorana can be expressed as a linear sum of the $\gamma_{i,\boldsymbol{j}}$ operators

$$\begin{aligned}\tilde{\gamma}_{1,n} = \frac{1}{\sqrt{2}} \sum_{\boldsymbol{j}} \Big[&\Re\big\{\beta^{\kappa_i}_{\boldsymbol{j}1}\big\}\gamma_{1,\boldsymbol{j}} - \Re\big\{\beta^{\kappa_i}_{\boldsymbol{j}2}\big\}\gamma_{2,\boldsymbol{j}} \\ &+ \Re\big\{\beta^{\kappa_i}_{\boldsymbol{j}3}\big\}\gamma_{3,\boldsymbol{j}} - \Re\big\{\beta^{\kappa_i}_{\boldsymbol{j}4}\big\}\gamma_{4,\boldsymbol{j}} \Big], \\ \tilde{\gamma}_{2,n} = \frac{1}{\sqrt{2}} \sum_{\boldsymbol{j}} \Big[&\Im\big\{\beta^{\kappa_i}_{\boldsymbol{j}1}\big\}\gamma_{1,\boldsymbol{j}} - \Im\big\{\beta^{\kappa_i}_{\boldsymbol{j}2}\big\}\gamma_{2,\boldsymbol{j}} \\ &+ \Im\big\{\beta^{\kappa_i}_{\boldsymbol{j}3}\big\}\gamma_{3,\boldsymbol{j}} - \Im\big\{\beta^{\kappa_i}_{\boldsymbol{j}4}\big\}\gamma_{4,\boldsymbol{j}} \Big]. \end{aligned} \tag{A.10}$$

where $\beta^{\kappa_i}_{\boldsymbol{j}g}$ come from the relevant eigenstates $|\kappa_i\rangle_\gamma$.

Bibliography

[1] L. D. Landau, Phys. Z. Sowjetunion **11**, 26 (1937). 1

[2] L. Landau and E. Lifshitz, *Statistical Physics: Course of Theoretical Physics* (Pergamon Press, Oxford, 1958). 1

[3] J. F. Annett, *Superconductivity, superfluids and condensates* (Oxford University Press, Oxford, 2004). 1

[4] K. v. Klitzing, G. Dorda, and M. Pepper, Phys. Rev. Lett. **45**, 494 (1980). 1

[5] D. J. Thouless, M. Kohmoto, M. P. Nightingale, and M. den Nijs, Phys. Rev. Lett. **49**, 405 (1982). 1, 2, 38, 52, 74

[6] A. Kitaev and J. Preskill, Phys. Rev. Lett. **96**, 110404 (2006). 2

[7] M. Levin and X.-G. Wen, Phys. Rev. Lett. **96**, 110405 (2006). 2, 38

[8] H. Li and F. D. M. Haldane, Phys. Rev. Lett. **101**, 010504 (2008). 2

[9] X. G. Wen and Q. Niu, Phys. Rev. B **41**, 9377 (1990). 2

[10] A. Kitaev, Annals of Physics **321**, 2 (2006), January Special Issue. 2, 3, 38, 56, 58, 77

[11] S. Ryu and Y. Hatsugai, Phys. Rev. Lett. **89**, 077002 (2002). 2

[12] Y. Hatsugai, Phys. Rev. Lett. **71**, 3697 (1993). 2

[13] D. C. Tsui, H. L. Stormer, and A. C. Gossard, Phys. Rev. Lett. **48**, 1559 (1982). 2

[14] R. B. Laughlin, Phys. Rev. Lett. **50**, 1395 (1983). 2

[15] B. A. Bernevig and T. L. Hughes, *Topological Insulators and Topological Superconductors* (Princeton University Press, Oxford, 2013). 2, 77

[16] M. Kohmoto, Annals of Physics **160**, 343 (1985). 2, 38

[17] A. P. Schnyder, S. Ryu, A. Furusaki, and A. W. W. Ludwig, Phys. Rev. B **78**, 195125 (2008). 2, 3, 16, 37, 39, 72, 74, 80

[18] S. Ryu, A. P. Schnyder, A. Furusaki, and A. W. W. Ludwig, New Journal of Physics **12**, 065010 (2010). 2, 37, 39

[19] C.-K. Chiu, J. C. Y. Teo, A. P. Schnyder, and S. Ryu, ArXiv e-prints (2015), 1505.03535. 2, 3

[20] X.-G. Wen, Phys. Rev. B **85**, 085103 (2012). 3, 37, 39

[21] C.-K. Chiu, H. Yao, and S. Ryu, Phys. Rev. B **88**, 075142 (2013). 3

[22] T. Morimoto and A. Furusaki, Phys. Rev. B **88**, 125129 (2013). 3

[23] K. Shiozaki and M. Sato, Phys. Rev. B **90**, 165114 (2014). 3

[24] L. Fidkowski and A. Kitaev, Phys. Rev. B **81**, 134509 (2010). 3

[25] A. Kapustin, R. Thorngren, A. Turzillo, and Z. Wang, Journal of High Energy Physics **12**, 52 (2015), 1406.7329. 3

[26] E. Witten, ArXiv e-prints (2015), 1508.04715. 3

[27] C.-T. Hsieh, G. Y. Cho, and S. Ryu, ArXiv e-prints (2015), 1503.01411. 3

[28] K. H. A., Proceedings Koninklijke Akademie van Wetenschappen **33**, 959 (1930). 17

[29] A. Altland and M. R. Zirnbauer, Phys. Rev. B **55**, 1142 (1997). 17

[30] A. Y. Kitaev, Physics-Uspekhi **44**, 131 (2001). 18, 38, 58, 81

[31] F. S. Levin, *An introduction to quantum theory* (Cambridge University Press, 2002).

[32] C. Nayak, S. H. Simon, A. Stern, M. Freedman, and S. Das Sarma, Rev. Mod. Phys. **80**, 1083 (2008). 28, 37

[33] J. K. Pachos, *Topological Quantum Computation* (Cambridge University Press, Cambridge, 2012). 35, 37, 78

[34] T. Fukui, Y. Hatsugai, and H. Suzuki, Journal of the Physical Society of Japan **74**, 1674 (2005). 35

[35] A. Kitaev, Annals of Physics **303**, 2 (2003). 37

[36] J. K. Pachos, Int. J. Quant. Info. **04**, 2 (2006). 37

[37] H. Sumiyoshi and S. Fujimoto, Journal of the Physical Society of Japan **82**, 023602 (2013), http://journals.jps.jp/doi/pdf/10.7566/JPSJ.82.023602. 38

[38] E. Grosfeld and S. Das, Phys. Rev. Lett. **102**, 106403 (2009). 38

[39] S. Onoda, N. Sugimoto, and N. Nagaosa, Phys. Rev. B **77**, 165103 (2008). 38

[40] B. Hetényi, Phys. Rev. B **87**, 235123 (2013). 38

[41] X.-G. Wen, Advances in Physics **44**, 405 (1995), http://www.tandfonline.com/doi/pdf/10.1080/00018739500101566. 38

[42] A. Kitaev and J. Preskill, Phys. Rev. Lett. **96**, 110404 (2006). 38

[43] H. Li and F. D. M. Haldane, Phys. Rev. Lett. **101**, 010504 (2008). 38

[44] C. L. Kane and E. J. Mele, Phys. Rev. Lett. **95**, 146802 (2005). 51, 52, 81

[45] J. K. Pachos, E. Alba, V. Lahtinen, and J. J. Garcia-Ripoll, Phys. Rev. A **88**, 013622 (2013). 51, 53, 55, 56, 58

[46] D. N. Sheng, Z. Y. Weng, L. Sheng, and F. D. M. Haldane, Phys. Rev. Lett. **97**, 036808 (2006). 52

[47] L. Wang, A. A. Soluyanov, and M. Troyer, Phys. Rev. Lett. **110**, 166802 (2013). 55, 56

[48] E. Alba, X. Fernandez-Gonzalvo, J. Mur-Petit, J. K. Pachos, and J. J. Garcia-Ripoll, Phys. Rev. Lett. **107**, 235301 (2011). 55, 56

[49] H. M. Price and N. R. Cooper, Phys. Rev. A **85**, 033620 (2012). 55

[50] D. A. Abanin, T. Kitagawa, I. Bloch, and E. Demler, Phys. Rev. Lett. **110**, 165304 (2013). 55

[51] M. Atala *et al.*, Nat. Phys. **9**, 795 (2013). 55

[52] R. O. Umucal ılar, H. Zhai, and M. O. Oktel, Phys. Rev. Lett. **100**, 070402 (2008). 55

[53] L. B. Shao, S.-L. Zhu, L. Sheng, D. Y. Xing, and Z. D. Wang, Phys. Rev. Lett. **101**, 246810 (2008). 55

[54] A. Dauphin and N. Goldman, Phys. Rev. Lett. **111**, 135302 (2013). 55

[55] K. Björnson and A. M. Black-Schaffer, Phys. Rev. B **89**, 134518 (2014). 55

[56] F. Gerbier and J. Dalibard, New J. Phys. **12**, 033007 (2010). 55

[57] D. Jaksch and P. Zoller, New J. Phys. **5**, 56 (2003). 55

[58] L. Mazza *et al.*, New J. Phys. **14**, 015007 (2012). 55

[59] L. Jiang *et al.*, Phys. Rev. Lett. **106**, 220402 (2011). 55

[60] G. M. Bruun and C. J. Pethick, Phys. Rev. Lett. **92**, 140404 (2004). 55

[61] D. Hsieh *et al.*, Science **323**, 919 (2009), http://www.sciencemag.org/content/323/5916/919.full.pdf. 56

[62] Y. Cao *et al.*, Nat. Phys. **9**, 499 (2013). 56

[63] A. M. Lunde and G. Platero, Phys. Rev. B **88**, 115411 (2013). 56

[64] A. Bermudez, M. A. Martin-Delgado, and D. Porras, New Journal of Physics **12**, 123016 (2010). 56

[65] N. Goldman *et al.*, Phys. Rev. Lett. **105**, 255302 (2010). 56

[66] B. Béri and N. R. Cooper, Phys. Rev. Lett. **107**, 145301 (2011). 56

[67] A. Bermudez *et al.*, Phys. Rev. Lett. **105**, 190404 (2010). 56

[68] A. Kubasiak, P. Massignan, and M. Lewenstein, EPL (Europhysics Letters) **92**, 46004 (2010). 56

[69] A. Acín *et al.*, Phys. Rev. Lett. **85**, 1560 (2000). 57

[70] V. Mourik *et al.*, Science **336**, 1003 (2012), http://science.sciencemag.org/content/336/6084/1003.full.pdf. 58

[71] S. Nadj-Perge *et al.*, Science **346**, 602 (2014), http://science.sciencemag.org/content/346/6209/602.full.pdf. 58

[72] A. Das *et al.*, Nat. Phys **8**, 887 (2012). 58

[73] L. P. Rokhinson, X. Liu, and J. K. Furdyna, Nat. Phys **8**, 795 (2012). 58

[74] M. T. Deng *et al.*, Nano Letters **12**, 6414 (2012), http://dx.doi.org/10.1021/nl303758w, PMID: 23181691. 58

[75] V. Lahtinen *et al.*, Annals of Physics **323**, 2286 (2008). 58

[76] V. Lahtinen and J. K. Pachos, New Journal of Physics **11**, 093027 (2009). 58

[77] Z. Nussinov, G. Ortiz, and E. Cobanera, Phys. Rev. B **86**, 085415 (2012). 58

[78] S. Ryu, Phys. Rev. B **79**, 075124 (2009). 58

[79] S. Sasaki *et al.*, Phys. Rev. Lett. **107**, 217001 (2011). 58

[80] S. Sasaki *et al.*, Phys. Rev. Lett. **109**, 217004 (2012). 58

[81] L. Fu and E. Berg, Phys. Rev. Lett. **105**, 097001 (2010). 58, 59

[82] A. P. Schnyder, S. Ryu, and A. W. W. Ludwig, Phys. Rev. Lett. **102**, 196804 (2009). 59

[83] D.-L. Deng, S.-T. Wang, and L.-M. Duan, Phys. Rev. B **89**, 075126 (2014). 59

[84] M. Z. Hasan and C. L. Kane, Rev. Mod. Phys. **82**, 3045 (2010). 60

[85] M. Sato, Y. Takahashi, and S. Fujimoto, Phys. Rev. Lett. **103**, 020401 (2009). 60

[86] J. Alicea, Phys. Rev. B **81**, 125318 (2010). 60, 80

[87] L. Fu and C. L. Kane, Phys. Rev. Lett. **100**, 096407 (2008). 60, 80

[88] M. Sigrist and K. Ueda, Rev. Mod. Phys. **63**, 239 (1991). 61

[89] M. Sato, Phys. Rev. B **79**, 214526 (2009). 61, 63

[90] J. de Lisle *et al.*, New Journal of Physics **16**, 083022 (2014). 74, 104

[91] J. C. Y. Teo and C. L. Kane, Phys. Rev. Lett. **104**, 046401 (2010). 78

[92] L. Fidkowski, X. Chen, and A. Vishwanath, Phys. Rev. X **3**, 041016 (2013). 78

[93] V. Lahtinen, A. W. W. Ludwig, J. K. Pachos, and S. Trebst, Phys. Rev. B **86**, 075115 (2012). 79

[94] B. Bauer, R. M. Lutchyn, M. B. Hastings, and M. Troyer, Phys. Rev. B **87**, 014503 (2013). 79

[95] M. Eto, Y. Hirono, and S. Yasui, Prog. Theor. Exp. Phys. (2014). 79

[96] A. M. J. Schakel, Phys. Rev. E **63**, 026115 (2001). 79

[97] P. Hosur, P. Ghaemi, R. S. K. Mong, and A. Vishwanath, Phys. Rev. Lett. **107**, 097001 (2011). 79

[98] H.-H. Hung, P. Ghaemi, T. L. Hughes, and M. J. Gilbert, Phys. Rev. B **87**, 035401 (2013). 79

[99] G. E. Volovik, *The universe in a helium droplet* (Oxford, 2003). 80

[100] L. Santos, Y. Nishida, C. Chamon, and C. Mudry, Phys. Rev. B **83**, 104522 (2011). 80

[101] I. Mandal, ArXiv e-prints (2015), 1503.06804. 80

[102] I. Mandal, EPL (Europhysics Letters) **110**, 67005 (2015). 80

[103] P. L. e. S. Lopes, J. C. Y. Teo, and S. Ryu, Phys. Rev. B **91**, 184111 (2015). 80

[104] D. Asahi and N. Nagaosa, Phys. Rev. B **86**, 100504 (2012). 80

[105] K. Shiozaki and S. Fujimoto, Phys. Rev. B **85**, 085409 (2012). 80

[106] W. P. Su, J. R. Schrieffer, and A. J. Heeger, Phys. Rev. Lett. **42**, 1698 (1979). 80

[107] R. Jackiw and C. Rebbi, Phys. Rev. D **13**, 3398 (1976). 80

[108] R. Jackiw and P. Rossi, Nuclear Physics B **190**, 681 (1981). 80

[109] N. Read and D. Green, Phys. Rev. B **61**, 10267 (2000). 80

[110] J. D. Sau, R. M. Lutchyn, S. Tewari, and S. Das Sarma, Phys. Rev. Lett. **104**, 040502 (2010). 80

[111] R. M. Lutchyn, J. D. Sau, and S. Das Sarma, Phys. Rev. Lett. **105**, 077001 (2010). 80

[112] Y. Oreg, G. Refael, and F. von Oppen, Phys. Rev. Lett. **105**, 177002 (2010). 80

[113] J. C. Y. Teo and C. L. Kane, Phys. Rev. B **82**, 115120 (2010). 80, 87, 103

[114] B. Béri, Phys. Rev. B **81**, 134515 (2010). 82, 93

[115] P. Finch, J. de Lisle, G. Palumbo, and J. K. Pachos, Phys. Rev. Lett. **114**, 016801 (2015). 87, 88, 94, 104

[116] X.-L. Qi and S.-C. Zhang, Rev. Mod. Phys. **83**, 1057 (2011). 103

[117] K. Nomura, S. Ryu, A. Furusaki, and N. Nagaosa, Phys. Rev. Lett. **108**, 026802 (2012). 103

[118] M. S. Foster, Phys. Rev. B **85**, 085122 (2012). 103

[119] T. Meng and L. Balents, Phys. Rev. B **86**, 054504 (2012). 103

[120] X.-J. Liu and P. D. Drummond, Phys. Rev. A **86**, 035602 (2012). 103

[121] H. Hu, L. Jiang, H. Pu, Y. Chen, and X.-J. Liu, Phys. Rev. Lett. **110**, 020401 (2013). 103

[122] S. Deng, G. Ortiz, and L. Viola, Phys. Rev. B **87**, 205414 (2013). 103

[123] L. B. Shao *et al.*, ArXiv e-prints (2013), 1304.4726. 103

[124] J. Li *et al.*, ArXiv e-prints (2015), 1501.00999. 103

[125] Y. Baum, T. Posske, I. C. Fulga, B. Trauzettel, and A. Stern, Phys. Rev. B **92**, 045128 (2015). 103

[126] Y. Peng, F. Pientka, Y. Vinkler-Aviv, L. I. Glazman, and F. von Oppen, Phys. Rev. Lett. **115**, 266804 (2015). 103

[127] J. J. Cha *et al.*, Nano Letters **10**, 1076 (2010), http://dx.doi.org/10.1021/nl100146n, PMID: 20131918. 103

[128] L. Chen and S. Wan, ArXiv e-prints (2010), 1005.4143. 103

[129] M.-T. Tran and K.-S. Kim, Phys. Rev. B **82**, 155142 (2010). 103

[130] R. Žitko, Phys. Rev. B **81**, 241414 (2010). 103

[131] Q. Liu, C.-X. Liu, C. Xu, X.-L. Qi, and S.-C. Zhang, Phys. Rev. Lett. **102**, 156603 (2009). 103

[132] F. Ye, G.-H. Ding, H. Zhai, and Z.-B. Su, EPL (Europhysics Letters) **90**, 47001 (2010). 103

[133] T.-P. Choy, J. M. Edge, A. R. Akhmerov, and C. W. J. Beenakker, Phys. Rev. B **84**, 195442 (2011). 103

[134] L. Mao and C. Zhang, Phys. Rev. B **82**, 174506 (2010). 103

[135] J. Chakhalian *et al.*, Nature Physics **2**, 244 (2006). 103